Theory of Single Spin Detection Using an ESR-STM Technique

Emma Cameron Podnieks

H. H. Wills Physics Laboratory
University of Bristol

A dissertation submitted to the University of Bristol
in accordance with the requirements of the degree of
Ph.D. in the Faculty of Science

Department of Physics
September 2006

Abstract

This thesis aims to describe the interaction between a tunnelling electron current and a local spin in a steady magnetic field. A spin in a steady magnetic field should decohere back to the equilibrium magnetisation direction in a defined time T_1. A current passing through a local spin within a tunnel junction has been observed to contain an a.c. component at the frequency defined by the precessional frequency of the local spin in the magnetic field. This oscillation remains after a time T_1 has elapsed.

The nature of the electron current tunnelling through a magnetic field is first studied using wave-matching techniques at a barrier wall symbolising the tunnel junction. This is explored in both a non-relativistic and relativistic framework, and the polarisation of an incoming unpolarised electron after it has crossed the barrier is calculated. The polarisation is found to depend upon the width of the barrier, and the strength of the magnetic field.

The problem is then reformulated into a scattering event using a Delta Shell potential in the Lippmann-Schwinger formalism. The bound states, scattering states and resonances are investigated, and the phase shifts caused by this potential are examined. A semi-relativistic approach is found to capture the energy dependence of the non-relativistic, whilst sufficiently showing the spin-orbit coupling caused by the electron spin.

The scattering from a local spin is then investigated, first as a static, then as a precessing spin. The phase shifts, the scattering amplitudes and the total scattering cross section is examined here, and the response of the electrons to the local spin is shown to be closely related to the orientation of the electron spin and the type of scattering that occurs.

Finally, the scattering cross section through both potentials is calculated to determine the size of the influence of the STM tip on the local precessing spin. It was found that oscillations were observed in the cross section as the effect of a second potential was increased, suggesting that it is necessary to include both potentials when modeling this scenario with the simple potentials used here.

I declare that the work in this dissertation was carried out in accordance with the Regulations of the University of Bristol. The work is original, except where indicated by special reference in the text, and no part of the dissertation has been submitted for any other academic award. Any views expressed in the dissertation are those of the author.

SIGNED: ....

DATE:..

Contents

List of Figures

List of Tables

Chapter 1

Introduction

1.1 The Importance of Single Spin Detection

The ability to measure a single spin is considered an important achievement in the field of Quantum Computation. A classical computer uses macroscopic regions of magnetic materials to store information as a series of 1's and 0's, and uses transistors made from semiconductor material as switches. In the field of quantum computation, quantum mechanical objects are sought to replace these mechanisms. The advantage of using quantum mechanical objects as storage devices, is that they can be placed into a state that is neither a 1 nor a 0, but rather a superposition of both states. The availability of this superposition of states can in principle result in computations that are performed in parallel instead of in series. Particular algorithms [3] have been predicted to perform exponentially faster when using quantum computation than when using a classical approach.

Obviously this is an attractive idea for sheer computational ability, but this is not the only motivation for advancing the field of quantum computation; overcoming the quantum limit is another. Moore's Law describes the rise in the number of transistors able to fit onto a silicon chip. As we advance to the limit of miniaturisation, the quantum nature of the atoms used will need to be considered. A move away from conventional methods will be needed, such as moving from using mesoscopic currents to using single electrons instead.

The simplest example of a quantum mechanical object is a quantum bit (a qubit), a two level quantum system that can be put into a superposition of its two eigenstates. The general state of such an object will be written as

$$C_0 \mid 0\rangle + C_1 \mid 1\rangle, \tag{1.1}$$

where the probability of each state occurring is given by the square of its coefficient $C_{0,1}$. When such a system is measured the qubit is projected into one of its two eigenstates with the probability associated with that state.

Possible two-level systems used in quantum computation experiments could be; an electron charge (0 or 1 electrons being the two states); the spin of an electron [4]; single ions in their ground and excited state [5]; nuclear spins [6, 7], and correlated many electron states. In this work we are concerned with a single electron spin as the qubit of choice. The two spin configurations - spin up and spin down, are the two levels, and the electron can be put into either state quite simply with an applied magnetic field.

For the actual physical construction of a quantum computer, there are a number of requirements set out by the 'DiVincenzo checklist': [8]

- The system must have identifiable qubits.
- An initial state must be able to be prepared.
- The system should be isolated from its environment.
- Manipulation of the system via universal gates must be possible.
- A strong measurement (readout) must be possible.

Each possible implementation of a quantum computer will find at least one of the requirements in the checklist difficult to meet. Possibly the most common difficulty however, is the isolation of the system from its environment. In order for the system to be measured, there must be some interaction with the outside world. However this leads to *decoherence*, the destruction of the quantum state, as the energy of the state is transferred to and from the environment. Any superposition that existed decays into its classical equivalent leaving no more extra information than a classical operation. The decoherence of a system often occurs at a faster rate than a coherent measurement can be made. This decoherence time, τ_d, varies immensely according to the qubit system. A nuclear spin can take 10^4 seconds to decohere, and electrons in a GaAs substrate can take as little as 10^{-10}s [9].

For quantum computations that use spin qubits, spin decoherence is a large barrier to their successful implementation. In an Optically Detected Magnetic Resonance (ODMR) experiment [10], approximately 10^6 readings are needed to acquire a coherent result. A continuous measurement of the spin state, which is the alternative measurement approach, would induce decoherence which would collapse the spin state before any reading can be made. Successful quantum computation using spins has been achieved in room-temperature liquid-state Nuclear Magnetic Resonance (NMR) experiments [7, 6]. A solution of molecules is used, encompassing ensembles of up to 10^{12-18} spins, each molecule differentiated due to their slightly differing chemical environment. In particular Ref. [7] demonstrated the implementation of Shor's factoring algorithm with 7 spin-1/2 nuclei factorising the number 15. The NMR technique has difficulties with some of the checklist requirements however; the thermal distribution of spin states make the preparation of the initial state difficult, and the large numbers of molecules involved in such experiments are impractical if it becomes necessary to scale the system. The thermal spin distribution ceases to be a problem when only a single spin is examined. In this case an output measurement could be made faster than the time it takes for the spin to relax.

With a reduced number of spins (~ 70), Rugar *et al.* [11, 12] have shown manipulation and control of spins using a Magnetic Resonance Force Microscope (MRFM). A cantilever with a small magnet at the tip combined with a microwave field are used to selectively capture positive fluctuations of paramagnetic spin centres in SiO_2. The spins are cyclically inverted by the cantilever, and can eventually create a mean polarization in the system. To image the location of a single spin however, an experimental run of ~ 13 hours was needed to distinguish the spin signal from the background noise level (due to the low signal-to-noise ratio).

The most appealing approach for a quantum computer would be the solid-state approach. Microfabrication techniques are already in use such that multiple systems can be reproduced easily, reducing the problem of scalability. Solid state qubits could be single electrons in a semiconductor quantum dot or electrons on a superconducting circuit with Josephson junctions [13].

Single quantum dots use the Zeeman-split energy levels of an electron as qubits [14]. Double dots can be used with the singlet and triplet states of two electrons acting as the qubit [4]. Careful manipulation of tuning parameters and the use of simple gate operations have been shown to increase the decoherence time of spin states from $\sim 10ns$ to greater than 1μs. However the inhomogeneous environment in a quantum dot may cause fluctuations in the Zeeman splitting of electrons in that dot. Lee *et al.* [15] study the extent to which these fluctuations cause operating errors in the dot. Some energy fluctuations may be due to changes of the electronic Landé g factor, but possibly the dominant mechanism for spin decoherence and relaxation is the electron-nuclear interaction. It was found that the precession frequency of the electrons is affected by the magnetic field of the nucleus (B_N) as well as the applied magnetic field B_0. This precessional frequency ω_e, is then given by

$$\omega_e = g_e \mu_B \sqrt{(B_0 + B_N)^2 + (B_N)^2}. \tag{1.2}$$

Spins in semiconductors have long decoherence times which should make them easier to detect. By introducing a trapping level within tunnelling distance of the conductance channel, the presence of a spin has been detected using a Field Effect Transistor [16]. The trap levels are spin-split using a magnetic field, and the transition between one trapped electron and two trapped electrons is detected. By using an Electron Spin Resonance technique and selecting the appropriate frequency, the single trapped electron 'flips up' in energy allowing a second electron to enter the trap, and reducing the current through the conduction channel.

Aside from the solid state approach to monitoring and manipulating quantum mechanical objects, there are other novel constructions used to perform calculations quantum mechanically. Two such ideas are those of ion traps and molecular cascades. A ^{9}Be$^+$ ion has been shown to have a coherence time on the scale of minutes, and be extremely versatile in the implementation of gates [5], as have trapped Ca$^+$ ions [17]. Neutral atoms have been trapped on microchips - a highly desirable potential system due to its reproducibility [18]. However, using groups of atoms as qubits introduces the problem of addressing the individual atoms. If lasers are used to select them the atoms have to be spaced such that they are optically resolvable, but still have the tight confinement needed to keep their quantum state well defined.

Although not a quantum computation, Heinrich *et al.* [19] have used interacting cascades of carbon monoxide molecules as nanoscale logic gates, leading the way to magnetic cascade computation. This work can potentially be expanded to make systems which could be easily reset and combined in large numbers to perform many calculations simultaneously.

1.2 Quantum Transport

Quantum computational interests aside, it is important to be able to read out measurements from these small devices on the macroscopic scale. One area of study bridging this gap between the microscopic and macroscopic world, is the study of molecular wires and chains of metallic atoms which make a connection between two bulk leads or connectors.

Much work has already been done on calculating conductance or transmission through molecules in a tunnel junction [20, 21, 22]. In Ref. [20] the conductance through benzene molecules sandwiched between two gold leads was studied using a combination of Density Functional Theory and Non-Equilibrium Green's Functions. Calculations were performed on molecules both stretched and relaxed, touching none, one and two extra gold atoms. This method included molecule-lead interactions, and the effect of contact atomic relaxation. The authors found a large difference in the conductivity when the number of gold atoms was increased, and could map the increase in conductance with an increased electron transfer from the Au leads to the benzene molecules.

In Ref. [22] the transmission of electrons through various benzene-derivative organic molecules is calculated using the Breit-Wigner formula. This is expressed in terms of the broadening of particular energy levels available for tunnelling. The current through such systems are calculated by integrating the transmission probabilities over the appropriate energy window around the Fermi energy. Speyer *et al.* [21] calculate conductance through a system using yet another method. The system (a polyaniline chain) is treated as if it is composed of a discrete lattice of components. Using a transfer matrix variant model, the electron flux can be calculated at intermediate steps as it propagates through successive rings of the chain. The transmission coefficient of the last step in the chain is inserted into the Landauer-Büttiker formula to find the conductance. First Principles calculations of band structures give the hopping energy of each step of the system.

This method is less computer-intensive than other approaches as it does not need Non-Equilibrium Green's Functions, and once the correct hopping terms are found, gives good agreement with experiment.

Transport through wires composed of metallic atoms have also been studied [23, 24, 25]. When there are large numbers of electrons in the system (as there will be in a metallic chain), a full ab-initio numerical technique can be used to calculate the effective potential (V_{eff}). This is the potential seen by all the electrons from the ground state of the leads and the atomic chain. In Ref. [23] a chain of Al atoms are modeled connected to 3D jellium leads. When the number of atoms in the chain rises above one, making a quantum wire, conductance quantization is seen, showing the opening of different transmission modes. This is also seen in Ref. [24], where an experimental and theoretical study of transport through lead nanowires of various widths is carried out. By going to the superconducting state, which closes off particular modes, the authors are able to examine some of the transmission modes individually.

Any discrepancy between experimental and theoretical results in quantum transport investigations could be due to neglecting electron-electron correlation effects in simulations. When considering tunnelling into molecules, these can be incorporated by including a description of the electronic structure of the molecule e.g. the HOMO-LUMO gap [22]. In the study of a chain of Pt atoms Ferretti *et al.* [25] include self-energy terms detailing the electron-electron correlations as well as the coupling between the leads and the atoms in the chain. This has the effect of reducing the transmission of electrons through the chain, taking account of the effect that the reduced dimensionality of the system has on the localisation of electrons.

When describing electron transport in a tunnelling experiment, we should be aware that there may be more than one tunnelling path open to the electrons [26]: a) Bulk to bulk tunnelling, b)tunnelling via scattering from the surface molecule, c) tunnelling through the surface molecule to the bulk, d) tunnelling via scattering from the tip molecule, e) tunnelling through the tip molecule. Each of these channels can be entered into an equation for the transition matrix, and the conductance can be found by taking into account interference from these different channels.

This approach involves viewing the molecule as a scattering centre. This is an alternative view to conductance/transmission that is often used in the description of electron motion through tunnel junctions as well as through wires or bulk material. Zarand *et al.* [27] studies the transition matrix of electrons scattering from a single magnetic impurity, and Ref. [28] studies a scattered wavefunction after its interaction with an impurity inside a wire. The presence of an impurity (representing a scatterer) in a lead will obviously affect the transmission through that lead, but in Ref. [28] it is shown that in a 2D wire, the strength of the impurity will NOT affect the transmission signature. In a weak scattering regime it is shown that near the threshold energy for scattering the scattering pattern doesn't even depend on the location of the scatterer.

1.3 Structure of the Thesis

This work details an analytic approach to modeling electrons interacting with a single spin in a tunnel junction. The bulk of this work is based on a scattering theory model which examines the transition of electrons through various single potentials. Two potentials are then combined to investigate the scattering cross section for the entire system.

In Chapter 2 I discuss the theoretical and experimental details of a scanning tunnelling microscope (STM). I then describe in detail the particular STM experiment I will be studying, and discuss current explanations in the literature.

In Chapter 3 I approach the problem through wave tunnelling techniques. I employ wave-matching in coordinate space, and discuss the effects felt when a barrier is asymmetric, and when we consider the incoming electron wave to be relativistic.

In Chapter 4 I introduce a Delta Shell model as an analytic treatment of an STM tip. The virtues of the model are described, then I look at the bound states and scattering states caused by such a potential. Chapter 5 deals with the relativistic version of the model and the derivation of the semi-relativistic limit.

Chapter 6 and 7 detail the adaption of the model to include a single spin, thus representing an impurity with a single spin rather than the STM tip. A stationary spin interacting with the spin of the tunnelling electrons is first discussed, then we assume the impurity spin is precessing in a magnetic field and describe the effect this has on the scattering states.

Chapter 8 combines a bare potential shell with a potential shell featuring a spin to model the STM experiment. The scattering cross section through both potentials is derived and the influence of the spin on the entire system is examined.

Chapter 9 will draw together my conclusions.

Chapter 2

Background: Electron Spin Detection and Scanning Tunnelling Microscopy

In this chapter we give general background information about Electron Spin Resonance (ESR) and Scanning Tunnelling Microscopy (STM) experiments, and we introduce the ESR-STM hybrid experiment [29], which is the main motivation for this work.

We begin by recounting the main points of electron spin theory that are exploited in an ESR experiment, and will then talk through a standard STM experiment describing the main points of the technique. Several successful techniques have been used to theoretically describe results achieved with an STM and I will go through some of the methods used. We will then discuss the results of two ESR-STM experiments performed by Manassen *et al.* [30] and Durkan *et al.* [29], and compare their results. We explore some current theories in the literature which try to explain the observed phenomenon, and discuss the implications and results of these papers.

2.1 The Behaviour of an electron in a Magnetic Field: Electron Spin Resonance

The magnetic moment of an electron is made up of the orbital angular momentum $\boldsymbol{l}$, and the intrinsic angular momentum, $\boldsymbol{S}$. $\boldsymbol{S}$ can be visualised by applying a static magnetic field in one direction (say the z direction) to a beam of unpolarized electrons. By passing through such a field, the electrons will acquire one of two possible polarizations. They will have a magnetic dipole moment aligned either parallel (μ^+) or anti-parallel (μ^-) to the applied field. For electrons these are the only two possible orientations, and the general theory of angular momentum dictates that such components must differ by $\hbar$ and be distributed symmetrically around zero [31]. The two values of this property S are therefore $\pm\hbar/2$.

The relation between the intrinsic angular momentum and the magnetic dipole moment is given by

$$\boldsymbol{\mu} = \gamma \boldsymbol{S} \ , \tag{2.1}$$

where the gyromagnetic ratio γ, is given by $-g|e|/2m_e$ for electrons. g is the Landé g-factor which is ≈ 2 for electrons.

If we isolate the spin magnetic moment by putting the orbital angular momentum l to zero, we can study the motion of μ as a magnetization vector. In a magnetic field a torque of strength $\boldsymbol{\mu} \times \boldsymbol{B_0}$ will change the direction of $\boldsymbol{\mu}$ with time, Figure 2.1. For $\boldsymbol{B_0} = (0, 0, B_0)$, it is easy to show that

$$\mu_x = \mu \sin(\alpha) \cos(\omega_0 t) \ ; \ \mu_y = \mu \sin(\alpha) \sin(\omega_0 t) \ ; \ \mu_z = \mu cos(\alpha) \tag{2.2}$$

where $\mu \sin(\alpha)$ is the projection of $\boldsymbol{\mu}$ in the x y plane, α is the angle the magnetic field makes with the z axis, and $\omega_0 = \gamma B_0$ can be identified as the frequency of rotation in the x y plane (the Larmor precession frequency).

We now introduce an oscillating magnetic field B_1, of frequency ω_1 perpendicular to the static magnetic field. If ω_1 is equal to the precession frequency ω_0, B_1 can tip the magnetization vector completely towards the x y plane in a time $t_{\pi/2} = \pi/2\gamma B_1$. But if $t_{\pi/2}$ is

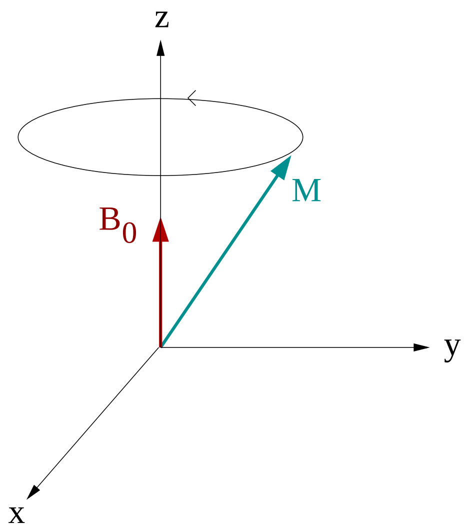

Figure 2.1: A magnetic moment precessing around the direction of an applied magnetic field.

too long, the spin responds to the perturbation through interactions with its environment and re-establishes equilibrium magnetization along the direction of the static field before it can be completely tipped. This is called longitudinal relaxation and is quantified by the time constant T_1 [32].

The motion of the three magnetization vectors after a perturbation due to B_1 are given phenomenologically by the Bloch Equations

$$\begin{aligned}\frac{d\mu_x}{dt} &= -\gamma\mu_y B_0 + \gamma\mu_z B_1 \sin(\omega_1 t) - \frac{\mu_x}{T_2}\ , \\ \frac{d\mu_y}{dt} &= -\gamma\mu_x B_0 - \gamma\mu_z B_1 \cos(\omega_1 t) - \frac{\mu_y}{T_2}\ , \\ \frac{d\mu_z}{dt} &= -\gamma(\mu_x B_1 \sin(\omega_1 t) - \mu_y B_1 \cos(\omega_1 t)) + \frac{\mu_0 - \mu_z}{T_1}\ . \end{aligned} \tag{2.3}$$

As well as the oscillatory term due to B_1, μ_x and μ_y also have a term which describes the tendency for the system to lose its magnetization in the x y plane due to transverse relaxation. This relaxation is quantified by T_2, the transverse relaxation time and describes the interaction of the spin with all of its neighbouring spins. If all the spins in a sample start in phase at $t = 0$, by $t = T_2$ the spins will be completely out of phase with one another and the net magnetisation in the x and y directions will be zero. The magnetization in the z-direction depends on B_1 only, and includes the enhancement of μ_z due to longitudinal relaxation. μ_0 is the thermal equilibrium magnetisation and represents the magnetisation vector at time $t = 0$.

In an ESR experiment, a condition called resonance is exploited. The quantum mechanical description of a precessing spin is summarised in Appendix A, and can be used to explain this effect. For such a system as detailed above, the probability of finding the system in the spin up state, ↑, at time t is given by

$$\frac{4\mu_B^2 B_1^2}{\hbar^2} \frac{\sin^2(\frac{1}{2}(2\mu_B B_0 t/\hbar - \omega_1 t))}{(2\mu_B B_0 t/\hbar - \omega_1 t)^2}, \tag{2.4}$$

where $\mu_B = e\hbar/2m$. The resonance condition is defined as when the system maximally absorbs energy from the applied a.c. field. This occurs in equation 2.4 when $\omega_1 = 2\mu_B B_0/\hbar$. For a g-factor of 2, this frequency is the Larmor precession frequency mentioned above:

$$\omega_1 = \frac{2\mu_B B_0}{\hbar} = \frac{2}{\hbar} \frac{e\hbar}{2m} B_0 = \frac{2e}{2m} B_0 = \frac{ge}{2m} B_0 = \gamma B_0 = \omega_0 \ . \tag{2.5}$$

This shows clearly that when the applied magnetic field oscillates at the Larmor frequency of the sample, maximum absorption (resonance) occurs.

One use of Electron (and Nuclear) Spin Resonance is to study a liquid or powder in order to decipher its constituents. The sample under study is placed into the two perpendicular fields described above. The frequency of the oscillating field is swept until a large absorption of energy is observed. The frequency that this occurs at gives information about which spins are in the sample, and also their relative quantity can be determined. ESR measurements typically require $\sim 10^{19}$ spins in order for a signal to be detectable so tends to be used on bulk samples.

2.2 Scanning Tunnelling Microscopy

2.2.1 Experimental Techniques

The attraction of scanning tunnelling microscopy is its ability to image down to the atomic level. First developed in 1982 by Gerd Binnig and Heinrich Rohrer [33], the scanning tunnelling microscope has spawned a whole family of microscopes which use a tip or cantilever very close to a surface to produce a topographical image of a surface. In conventional STM, a tip, typically made from tungsten or platinum, will be sharpened to as sharp a point as possible using electrolytical etching or cleaving techniques. An ideal tip will have a single atom at the end of it. This tip is raster-scanned in the x-y plane over a surface at a distance of a few Angstroms above the surface. The scan is driven by two piezo-drives perpendicular to each other and to a third drive that controls the height of the tip above the sample. As it is scanned, a potential difference is placed between the tip and the sample. Electrons from the occupied states in the tip (or the surface), will then tunnel across the gap into the unoccupied surface (tip) states depending on which way the voltage bias is applied. The tunnelling current that results from this is exponentially dependent on the distance between the tip and the surface, and is studied as a function of the x-y position of the tip.

There are two main scanning modes - constant current mode, and constant height mode. For constant current mode, the feedback system attached to the tip changes the height of the tip in the z-direction such that the tunnelling current is maintained at the same value. The resulting scan is then a map of height z as a function of x-y position. A constant height scan will give a map of current value against x-y position. Constant current techniques may involve a lag in time before the z piezo-drive responds, and a constant height scan cannot give an absolute value of the height of the tip above the sample, and is highly sensitive to vibrational disturbances. Due to the high sensitivity required in both these techniques, it is imperative that vibrations are kept to a minimum. This can be achieved somewhat by making the unit small and stiff such that the first mechanical resonant frequency is very high.

An STM can be used for a variety of purposes. As well as imaging the surface distribution of atoms and electronic structure, an STM can initiate and study chemical reactions, and be used for spectroscopic uses (see for example Ref. [34]). When examining a metal surface, an STM will be operated at a few milli-electron volts, drawing a current typically between 10 and 100pA. The majority of the tunnelling current is from the surface atoms, where the electron wavefunction overlaps significantly with the tip wavefunction. The next atom down, being about 3 Å away, will contribute about 0.1% to the current. This suggests that for atomic resolution, the macroscopic shape of the tip isn't as important as having a single atom at the end of it. For topographic studies though the shape is important. If the cone angle of the tip isn't narrow, it won't penetrate into deep and narrow grooves between the surface atoms. Techniques can be applied to account for the tip shape [35, 36] when reconstructing topographies.

An important development in the field of scanning tunneling microscopy is the use of spin-polarized probes. By using a tip coated in a ferromagnetic material, spin-polarized electrons will tunnel into the sample surface. The spin-polarized current will then see the magnetic structure of the surface in addition to the chemical structure [37], and properties such as magnetic domain structure, and even hysteresis on the nanoscale, [38] can be imaged. It is also possible to use the polarization of the electrons as an indicator of which angular momentum wavefunction is contributing most to the tunnelling process [39].

2.2.2 Theoretical studies of the STM

This section draws upon a review of STM theories by Drakova [40] in which more details and references can be found.

Perturbation Theory

The first theoretical development in the study of a tunnelling microscope involved the use of perturbation theory. J. Bardeen [41] considered multiple-particle tunnelling using the simple electron transition probability

$$P_{\mathrm{mn}} = \frac{2\pi}{\hbar} \mid M_{\mathrm{mn}} \mid^2 \rho_{\mathrm{n}} \ . \tag{2.6}$$

M_{mn} is the tunnelling matrix element from the initial to the final states of the electron, and ρ_{n} is the density of the final states of the electron.

Bardeen treats the problem by dividing the system into two, halfway between the two sides, inside the barrier. Two proposed wavefunction solutions each exist in one side of the barrier and they overlap inside the barrier assuming that they are not perturbed by the presence of the other electrode. The wavefunctions are reflected at the barrier, but also decays exponentially inside the barrier. Only considering elastic tunnelling, a time-dependant solution is constructed and the matrix element (which was postulated to be a constant for metal-metal barrier systems) is given by

$$M_{\mathrm{mn}} = \int \Psi_0^*(H - E_{\mathrm{mn}})\Psi_{\mathrm{mn}}\, d\tau \ . \tag{2.7}$$

This is the overlap of the two wavefunctions integrated over their adjoining surface. From this we can get the current density operator in the barrier region which appears to be zero outside the barrier, and independent of position once we look inside the barrier region.

By treating any tip-sample interaction as negligible, this model can only hope to reproduce results in which the tip is a large distance from the surface, and any variation in the conductance occurring from such a model can only arise from a change in the density of states the electrons are tunnelling into.

Bardeen's approximation looks at the tunnelling process only and ignores the difference between the mechanisms responsible (i.e. localised states are treated the same as propagating states). Further more, because this is a perturbation method, the approximation is only valid in the weak coupling limit (for small tunnelling currents). For a realistic system with a large number of defects, this can be interpreted as the limit in which the tunnelling rates are smaller than the scattering (of localised into propagating states) rates due to the defects.

Tersoff and Hamann [42] use these results and model an STM with the following additions; the surface being examined is treated exactly, and the tip is modeled as a locally spherical potential well. The Bardeen formulism gives the tunnelling current as

$$I = \frac{2\pi e}{\hbar} \sum_{\mathrm{mn}} f(E_{\mathrm{m}})[1 - f(E_{\mathrm{n}} + eV)] \mid M_{\mathrm{mn}} \mid^2 \delta(E_{\mathrm{m}} - E_{\mathrm{n}}), \tag{2.8}$$

where $m(n)$ represents the probe (surface), and f represents the Fermi Function. If the tip was a point probe, the matrix elements would be proportional to the wavefunction of the surface at the position of the probe ($\boldsymbol{r_0}$). It is shown in [42] that the spherical tip approximation is only important for the normalisation of the current and doesn't change the behaviour of the current as a function of potential. For simple s-wave tunnelling, the tunnelling current is proportional to the bare surface local density of states at the Fermi level, so any tip artefacts appear to not affect the observed currents.

This is another result that only holds for large tip-surface distances. In a real scan a sign reversal of the conductance is observed with a small tip-surface distance [43, 44], and perturbation theory cannot reproduce these results.

Three dimensional scattering and the generalised Ehrenfest theorem

Analytic models can describe the basic tunnelling processes, but to accurately describe a realistic scenario, ab initio calculations based on density functional theory are needed. To make an improved model of an STM experiment it is important to treat the wavefunctions exactly. To this end, a three dimensional model is developed in which each tunnelling event is viewed as a scattering process. The electrons approach from deep inside the tip (surface) region as a plane wave wavefunction, scatter from the tunnel junction and pass into the surface (tip) region, leaving the scattering centers as plane waves again. The incoming wave $\mid i+\rangle$ should be a eigenfunction of the whole STM system, and the outgoing wave $\mid f\rangle$ just an eigenfunction of the surface Hamiltonian. The tunnelling current is not affected by potentials far from the tunnel junction, so modeling the probe and surface with only a few layers of atoms is physically and mathematically adequate. The current is calculated from the generalised Ehrenfest theorem, and is written as a product of the transition matrix for tunnelling and a Delta function in energy:

$$J_{f\leftarrow i} = \frac{4\pi e}{\hbar} \mid \langle f \mid V_{\mathrm{tunn}} \mid i+\rangle \mid^2 \delta(E_{\mathrm{f}} - E_{\mathrm{i}}) \tag{2.9}$$

This expression for the current factorises into S_{tip}, representing the eigenfunctions of the total Hamiltonian with boundary conditions corresponding to the incident wave; and into $S_{\mathrm{electrode}}$, which corresponds to the eigenfunctions of the wave for the outgoing wave (which has no contribution from the tip). These can be understood to be indicative of the local electron densities of the relevant parts of the system. When these are used on wavefunctions localised in the tunnel barrier region (wavefunctions chosen to define the tip shape in space), $S_{\mathrm{electrode}}$ includes information on the electronic structure of the sample, and S_{tip} describes the tip-surface interaction information that was missing in the perturbation method described above. This is the main benefit of using this method; the ability to resolve numerically these two physical aspects of the tunnelling process. In Ref. [1] Doyen *et al.* successfully use this model to show the sign reversal of the conductance at low tip-surface amplitudes (Figure 2.2).

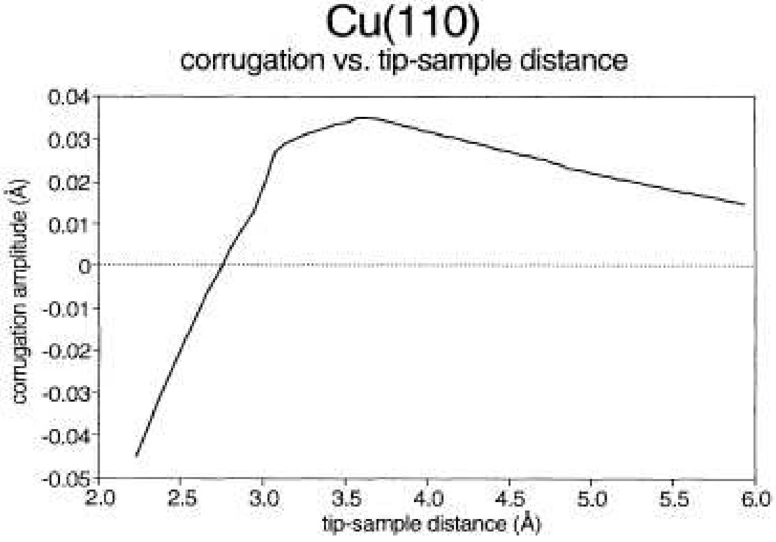

Figure 2.2: The sign reversal of the corrugation amplitude is correctly calculated in Ref. [1] using three dimensional scattering to model the STM experiment.

Current Density Integration

The current density integration approach to calculating an STM current involves introducing an interface between the tip and the surface, over which the current density is integrated. The interface can be placed either in a vacuum barrier if modeling an STM [45], or within the surface itself. This appears to be a physically transparent method, but the current density is not an observable and requires the simultaneous measurement of position and momentum. Calculating the initial states and the Green operator of the tip environment both require many summations over states making this a possibly computationally intense method.

Work has been done to show the equivalence of this method to Bardeen's Transfer Hamiltonian [46] in the weak perturbative limit. Starting from this, Doyen [44] has shown that by extending the equivalence to the strong coupling limit, an equivalence to the generalised Ehrenfest theorem (for a single electron current) can also be found. The equivalence does depend on normalization methods however - the current density wavefunctions have to preserve total flux before and after the scattering event (total scattered wavefunction = incoming plane wave + scattered wave), and the wavefunctions used in the Ehrenfest approach are normalized according to formal scattering theory (total scattered wave = incoming wave).

Scattering using the Landauer-Büttiker approach

The tunnelling current can be calculated from the tunnelling probability using the Landauer-Büttiker approach. The probability is given by the scattering matrix elements S_{if}

$$P = \sum_{\mathrm{i,f}} S^{*}_{\mathrm{if}} S_{\mathrm{fi}} = TrS^{\dagger}S \tag{2.10}$$

These elements are closely related to the transition matrix elements of the Ehrenfest method, and can be shown to give the exact same result for the conductance. Usually, when using this approach, the electrodes are structureless, in much the same way as the potential far from the tunnel junction in the Ehrenfest method was assumed to not affect the tunnelling current.

The Landauer approach only considers the coherent current due to wavefunctions expanding throughout all space. Incoherent states, such as surface and localised states are not included. However lattice defects may couple these states to the propagating coherent states, which results in the Landauer transmission ignoring these possible transmission channels. This method is often used for calculating transport through quantum wires [23], or through systems in which the transmission of the current through each component can be defined [47, 14].

Wortmann *et al.* [48] explore the difference between the Landauer and Bardeen approaches for conductance through a tunnelling barrier when describing the scenario as two semi-infinite volumes. They use an embedding potential technique using a surface located in space between the two sides. They found that both methods yielded the same results for a simple analytic model with a wide barrier. Once a realistic model was examined however, with localised interface states as well as propagating states, the Bardeen approach gave more accurate results, again in the limit of a thick barrier (which arises from the built-in limitations of the Bardeen model anyway). The Landauer approach was only accurate for when the conductance was mainly due to Bloch states.

The above approaches are all based on single-particle calculations. The natural next step in the development of a theory for STM tunnelling is by treating the system in a many-body framework.

Many-Particle Theories

An STM system can be regarded as being in a non-equilibrium state, and the tunnelling current can be calculated using the Keldysh formulism. This involves writing non-equilibrium Green's Functions (NEGF) for a system of interacting particles in terms of the Green's Functions for a non-interacting electron gas. With realistic models of the tip and the sample this can be an effective way to calculate the STM current. It is used when more atomic detail is required, and by combining Density Functional Theory and NEGF, this method has been shown to more accurately describe electron transport through molecular [20] and atomic [49] devices. A drawback of this technique however is that it can become computationally intensive.

Further Developments

The above approaches are all incomplete in that they do not explain the large corrugation amplitude (atomic resolution) seen in metals which are practically free-electron-gas-like metals. The charge density at these points of high amplitude are not large enough to account for the experimental results. It was suggested by Drakova *et al.* [2] that treating the charge tunnelling as an excited-state problem may be the solution to this. This is the basis of the dynamic theory of tunnelling. If we view tunnelling electrons as being injected locally into the sample, an excited state with a finite lifetime may occur which may have a very different transition probability to the ground state. The response of the surrounding medium to this excited state and its subsequent relaxation can increase the atomic resolution and has been shown [2] to match the increased corrugation amplitude seen in many experimental cases (Figure 2.3).

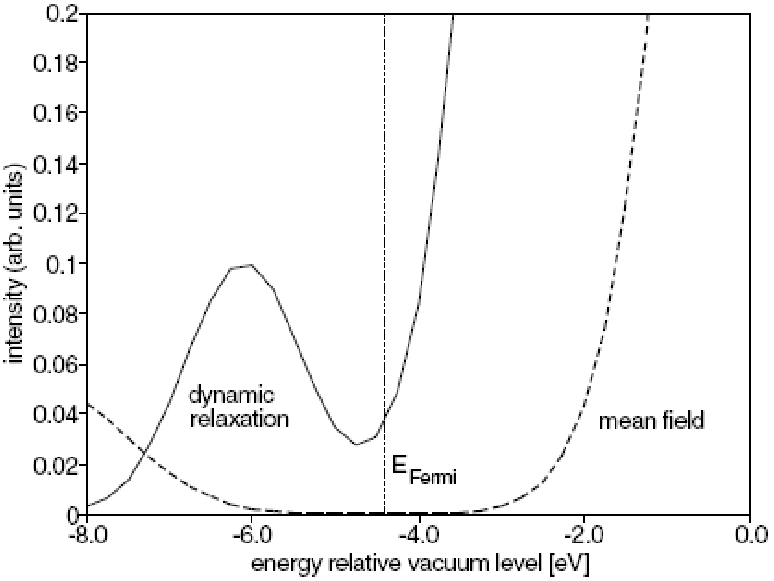

Figure 2.3: Work from Ref. [2] showing the calculated increase in corrugation amplitude using dynamic relaxation theory over mean field theory.

2.3 Detection of a single electron spin: The ESR-STM experiment

2.3.1 Experimental Detail

The two experiments below describe the discovery of an a.c. component in a tunnelling current when particular molecules are studied in a d.c. magnetic field.

This experiment was first performed by Manassen *et al.* in 1989 [30]. The authors studied a partially oxidized Si(111) surface with tips made from etched tungsten. A magnetic field was applied using two parallel bar magnets under the surface such that the magnetic field was perpendicular to the surface, and the strength of the field was modified by varying their separation. A circuit to separate the a.c. current from the d.c. current was constructed and was shown to be capable of detecting a 0.25 nA current at a frequency of 500 MHz. A slow conventional STM scan was performed with an r.f. power spectrum being measured every 3 Å. It was found that when the tip was far from a spin centre, the r.f. component was very small. It increased as the spin centre was approached and decreased as the tip then receded from the spin, Figure 2.4.

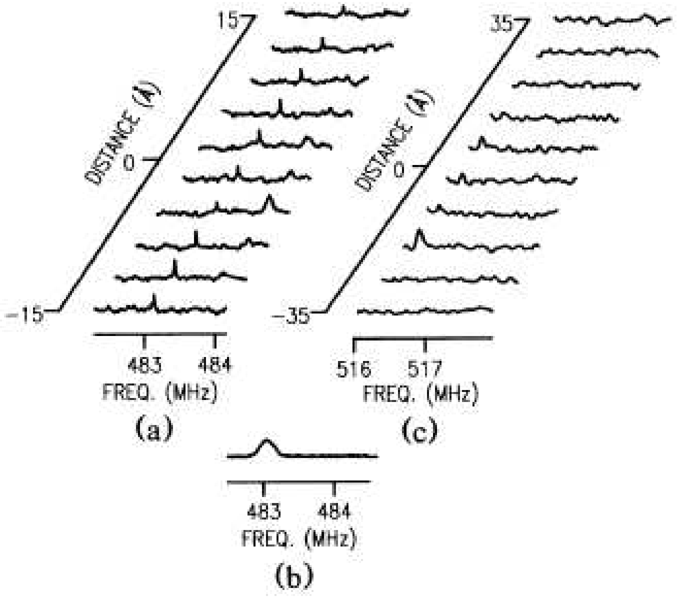

Figure 2.4: (a) Consecutive r.f. power spectra of the tunnelling current, measured at different lateral separations of the tip from a spin centre in a field of 12 G. (b) A power spectrum near another spin centre in a 172 G field. (c) Same as in (a) except for a field strength of 185 G.

For a Landè g-factor of 2, for an electron, the Larmor frequency is given by

$$\omega_L = \frac{g_e \mu_B B}{\hbar} = \frac{2\mu_B B}{\hbar} \tag{2.11}$$

The peak frequency in the power spectrum was found to obey this expression to within 2 MHz for varying magnetic field strengths. The exact nature of the spin centres were not known due to an inability to successfully image partially oxidized surfaces. The authors postulated that the difference between the measured frequency and the Larmor frequency could be due to either the possible different configurations of spin centres which could vary the gyromagnetic factor, or the small electric field originating from the STM tip. The expected value for the Larmor frequency was also limited by the accuracy to which the magnetic field could be measured.

There was some initial controversy with the findings in this work which is subsequently addressed by the author in Ref. [50]. The ability to detect such a small r.f. signal was verified by the addition of a small coil that could generate a small a.c. magnetic field component to the d.c. field. A phase-sensitive detection technique was used with a lock-in amplifier, and it was shown that an STM tip was capable of picking up a modulated signal.

The more recent experiment by Durkan *et al.* [29] involved the study of the organic molecule BDPA (α,γ-bisdiphenylene β-phenyl allyl). It is a stable free radical (has one unpaired electron) with a conjugated π electron system and a ^{13}C nucleus. The orbital angular momentum is s-wave. Conventional ESR experiments indicate a longitudinal relaxation time (T_1) of 1.1×10^{-7} s and a transverse relaxation time (T_2) of 1.0×10^{-7} s [51]. Later experiments [52] give T_2 as 0.5×10^{-7} s when BDPA is carried in mineral oil. BDPA has an isotropic g-factor of 2.0026 ± 0.0002 which has been shown to be constant over the temperature range 77 K to room temperature [53].

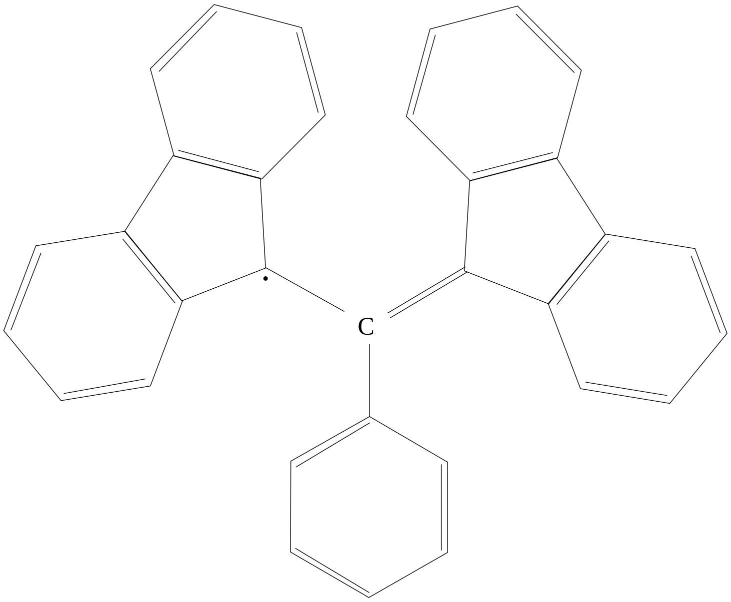

Figure 2.5: The chemical structure of BDPA, the molecule used in Ref. [29] (from[52]). Each vertex represents a carbon atom and each line represents a bond. The vertices with only three bonds are understood to have a hydrogen atom attached as the fourth bond. The vertex with three bonds and a dot however, symbolises one unpaired electron, which is the signature of a free radical molecule.

In Ref. [29] BDPA was deposited onto highly-orientated pyrolytic graphite (HOPG) to a concentration of ~ 100 molecules per μm^2. This substrate was chosen as it has negligible spin-orbit coupling, so should not interact with the molecule or the tunnelling electrons, and the experiment was performed in air. Typical molecular cluster sizes were $40 - 60$ Å across and $2 - 3$ Å high. The sample was mounted on a series of permanent Sm/Co magnets which varied in magnetic strength from $190 - 300$ Gauss. The magnetic axis was pointing through the sample in the direction of the tip, Figure 2.6. The STM tips used were electrochemically etched from Pt-Ir or mechanically formed from Au. The potential difference across the tip and surface was recorded as 350 mV with a tunnelling current of 1.4 nA. The range of frequencies expected for electrons interacting with the given magnetic field ranged from $585 - 840 \pm 0.28$ MHz, with the error determined by the accuracy of the Hall probe measuring the strength of the magnetic field.

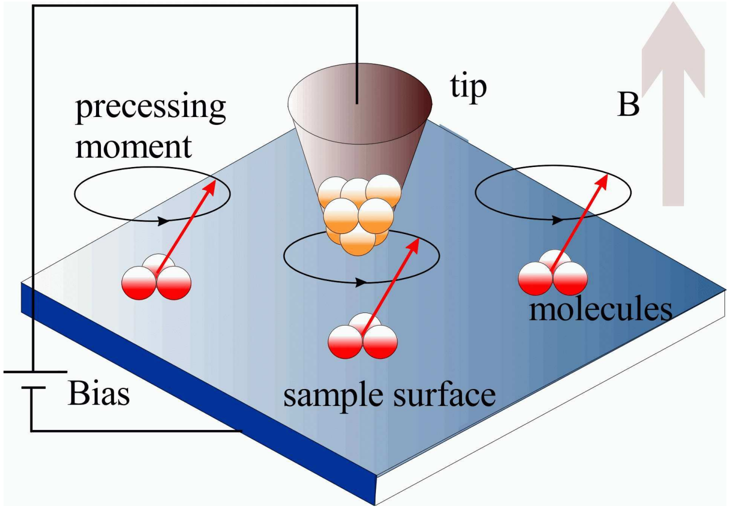

Figure 2.6: The experiment performed by Durkan *et al.* . BDPA is evaporated onto HOPG then placed into a constant magnetic field. The surface is imaged using conventional STM. Taken from C. Durkan with kind permission.

The STM tip was used in conventional mode to locate the molecular cluster, which typically contained a few molecules. It was then held stationary over a cluster and the tunnelling current spectrum was measured using an r.f. amplifier. The spectrum was sampled every 40 ms, and using a noise spectroscopy technique, a peak was seen at a given frequency for 100 ms - 1 s before disappearing. The size of the oscillating current is calculated in Ref. [54] to be $\sim 10^{-15}$ A.

When the magnet beneath the sample was changed, the peak frequency increased with the magnetic field according to equation 2.11 (shown in Figure 2.7). The Landè g-factor can be inferred from the graph in Figure 2.8 to be 2 ± 0.1, although it is of limited resolution.

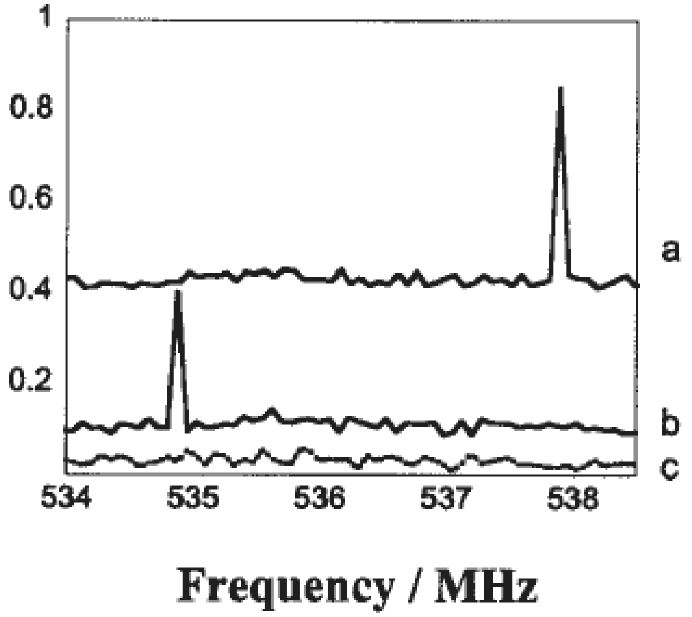

Figure 2.7: STM spin spectra of BDPA clusters (a), (b) taken a few nanometers apart. (c) shows a scan on the bare HOPG. The graphs are shifted vertically for clarity, and the vertical scale is arbitrary. Taken from [54].

For a constant magnetic field, a shift of peak frequency occurred after a short while; the authors suggest that this may be caused by a given molecule only interacting for a short time before switching off or saturating, and another molecule taking its place to interact with the tunnelling current. The r.f. signal on the bare HOPG surface was also studied. No peaks were found, verifying that the effect observed arises from the molecule itself and is not an artefact of the experiment construction.

Another free-radical molecule studied by Durkan is TEMPO [54]. It has a nuclear spin of 1, and therefore exhibits hyperfine splitting in a magnetic field. Three peaks were observable in the STM spectra, Figure 2.9, the centre one being at the Larmor frequency

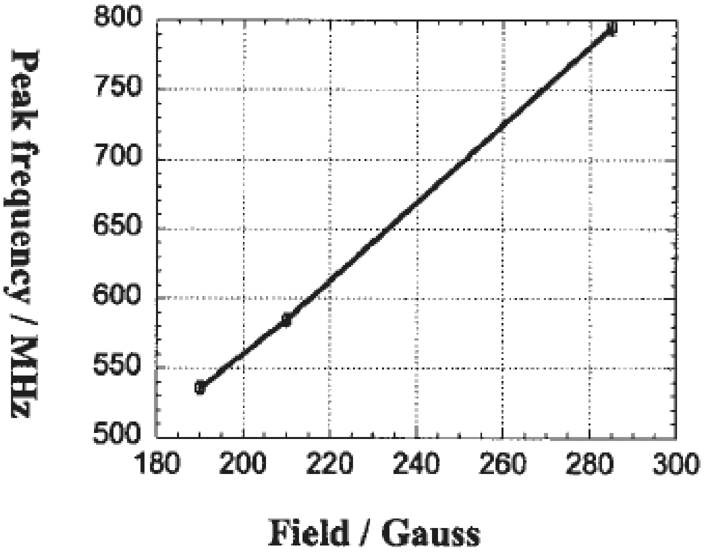

Figure 2.8: Plot of central frequency of STM spin spectra peaks on clusters as a function of the applied magnetic field. From this, the authors obtain a value of $g = 2 \pm 0.1$. Taken from [54].

for the applied field. This technique is obviously capable of detecting nuclear as well as electronic spins.

The most recent developments by Durkan [55] are towards the study of a spin-polarized STM (SP-STM). This is achieved by coating a non-magnetic tip with a few layers of iron. This results in closed magnetic domains on the end of the tip, and the tunnelling electrons are expected to take on the magnetic character of the domain they exit from. It was observed in this experiment that maximum conductance was achieved if the moment on the end atom of a tip was in the same direction as the magnetic moment on the surface atom, and minimum conductance was observed if they pointed in the opposite direction to one another.

2.3.2 Discussion

Both experiments use a d.c. magnetic field supplied by permanent magnets whose axis points in the same direction - towards the tip of the STM. In neither experiment is an a.c. field applied, the only use of it in Manassen's experiment is to verify that the equipment

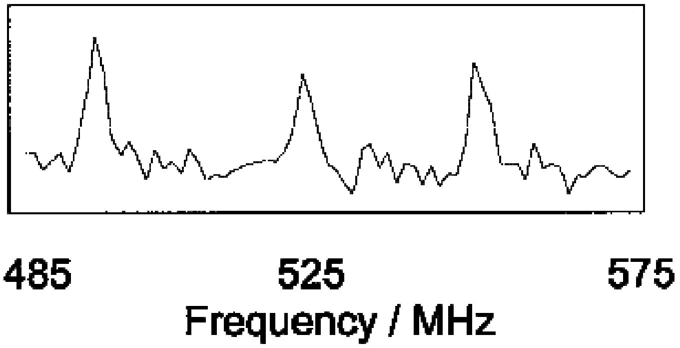

Figure 2.9: STM spin spectra of TEMPO clusters. The three peaks are evidence of hyperfine splitting. Taken from [54], the vertical scale is arbitrary.

can detect an a.c. signal. Yet both experiments detect a small a.c. current of the order of 10^6 smaller than the expected d.c. current.

The form of the spin centres studied by Manassen are unknown, and are not easily imaged using a conventional STM in order to find their location. Instead, Manassen provides a mapping of the spin locations based solely on their spin signal. In contrast, the BDPA used by Durkan is located with ease, and it is known for certain whether the tip is held over a spin centre or not. The spin signals measured by Manassen were reported to be localised over approximately 10 Å , with measurements taken at 3 Å intervals. We are told that the BDPA molecules are 40-60 Å across, but do not know how the signal varies across the molecule. However the frequency hopping noticed by Durkan could be due to the extended molecule size; we may expect no modulation of the spin if the tip is directly above the spin (due to its symmetric oscillation around the z-direction magnetic field), and an increased modulation as we move slightly to one side. Although Manassen claims that the *size* of the signal rather than the frequency changed as the spin was passed over by the tip.

This is not a conventional ESR experiment in which a second magnetic field is applied perpendicular to the static field in the z direction. The only possible source of perturbation to the spin appears to be the tunnelling electrons. However there should be nothing unusual about the electrons. All the tips used are non-magnetic so the electrons should be unpolarised. It is unlikely that both sets of results featured contamination of the tip, and recent private communication with Durkan suggests that the use of a deliberately spin-polarised tip resulted in no spin signal being detected. One reason for this though, may be because it appears that an atomically-sharp tip is required to see a spin signal. Coating a tip with a ferromagnetic material inevitably makes it 'blunt' in STM tip terms. The tip limits the reproducibility of the experimental conditions. It is difficult to quantify the shape and structure of the tips used; they can be imaged after they are used, but their exact structure during the experiment is not known. Producing atomically similar tips is practically impossible, and once the system is disturbed to allow for changing of tip or magnetic field, there is no way to know whether the same molecule is being imaged again. The nature of the spin centres observed by Manassen are unknown, but the BDPA molecule studied by Durkan is well characterised. When considering the motion of the tunnelling electrons past and through this molecule, we need to ask how the spin of the molecule is even precessing coherently for the length of time necessary for the measurement to be taken?

Examining the motion of the electrons ballistically, a tunnelling current of 1 nA, which represents the charge per second passing through the impurity molecule into the substrate below, corresponds to an electron transition frequency of 10^{10} Hz. The applied magnetic field of 200 G corresponds to an electron precession frequency of $\omega_L/2\pi = 500$ MHz. This results in a time period of $T = 2$ ns. For a spin relaxation time (T_1) of 110 ns, these values mean that typically, 50 precessions of the impurity molecule will occur before the molecular spin decoheres back to its equilibrium value. During one of those precessions, ~ 10 electrons (for a 1 nA current) will pass by the molecule. This results in 600 electrons passing before the molecule decoheres. If we instead imagine that the tunnelling electrons are precessing, and the molecular spin is static, the electron will have completed ~ 0.1 of its precession by the time it has passed the molecule.

The experiments detected an oscillation in the rate of electron transition - in Ref. [54], Durkan calculates the oscillation to be of an amplitude of $\sim 10^{-15}$ A. For every million electrons that pass by the molecule, their numbers will therefore change by ± 1 in one molecular precession. The questions to ask then, are how does the tunnelling current interact with the BDPA molecule, and how does this interaction project onto the tunnelling current spectrum?

2.3.3 Theoretical Explanations

As well as asking how the tunnelling electrons interact with the molecular electron, we can ask whether there are any correlations between the separate tunnelling electrons (for a non-spin-polarized tip). Balatsky, Manassen *et al.* [56] claim that no correlations within one precessional period are needed in the spin polarization of the tunnelling electrons to produce a current noise at the Larmor frequency.

Instead the noise arises from a $1/f$ noise already present in the conduction electrons in metals. These are fluctuations in the magnetization of conduction electrons caused by a superposition of consecutive random events starting at t_0, each of which follow an exponential relaxation law;

$$N(t - t_0) = N_0 \exp\left(-(t - t_0)/\tau\right) \tag{2.12}$$

For a distribution of relaxation times τ, the overall spectral density takes on a $1/f$ form. Balatsky *et al.* claim that it is the coupling of this $1/f$ magnetic noise from the tunnelling electrons with the local molecular spin that creates the peak in the current noise at the Larmor frequency.

It is necessary however to have a mechanism which causes this distribution in relaxation times. This could be due to local magnetic defects or polarizing fields. It is also suggested that the individual dephasing events in a metal that are responsible for the T_2 relaxation of conduction electrons, are similar to the relaxation events responsible for general $1/f$ noise.

Durkan, [54] shows using a WKB method, that the spin current through the tunnelling junction will be affected by the applied magnetic field, introducing correlations into the current. The magnetic field splits the tunnelling current into spin-up and spin-down electron components creating a spin-polarized component which may be responsible for the detected effect. This component should remain constant as the magnetic field is increased, and should also increase as the temperature is decreased. For standard experimental values of 4 eV for barrier height, 0.7 nm for barrier width, 20 mT for the applied magnetic field, and at a temperature of 300 K, Durkan calculates the polarized current to be equal to 65 fA.

Another paper by Balatsky and Manassen [57] asks the question: What is the role of a direct Heisenberg interaction between the local spin and the tunnelling electrons? They consider the spin polarization of the tunnelling electrons to be zero on a long time scale but not on the time scale of one precession of the local spin.

The spin-dependant tunnelling matrix element is given by

$$\hat{\Gamma} = \Gamma_0 \exp\left[-\sqrt{\frac{\phi - JS(t)\hat{\sigma}}{\phi_0}}\right] \tag{2.13}$$

ϕ_0 is the energy due to the distance between the sample and the tip, ϕ is the barrier height, and $JS(t)\hat{\sigma}$ is the exchange interaction. Γ_0 describes all the spin-independent tunnelling, and the current can be given by the sum of electrons tunnelling with each different spin orientation. By assuming that the Heisenberg exchange coupling between the tunnelling electrons and the local spin is a fraction of an electron-volt, the effective barrier as seen by the tunnelling electrons (which determines the current) is determined by the local spin orientation, which is assumed to be periodic and slow compared to the rate of electrons tunnelling.

The current dispersion is given as a multiple of the Larmor frequency component of the local spin, and the spin spectrum of the tunnelling electrons. They calculate the magnitude of the fluctuating current (in time) due to this exchange interaction to be of the order of 10 pA for a dc current of 1 nA. This will give a peak at the Larmor frequency once there is some polarization in the tunnelling current at a time scale of the relaxation time of the local spin. (It is noted that if the spins of the tunnelling electrons are totally uncorrelated, the noise component of the current will be smeared out over the full frequency range, and it is only if there is a degree of spin polarization, which this model does not provide, that a strong peak will appear at the Larmor frequency.)

Balatsky also asks in [58] under what conditions is it possible to detect the single spin precession with an STM? He suggests the coupling interaction is a spin-orbit one, and that the local spin is characterized by a Zeeman-split wavefunction;

$$| \Psi\rangle = \alpha \, |\uparrow\rangle + \beta \, |\downarrow\rangle \tag{2.14}$$

which evolves in time as

$$\alpha =| \alpha | \exp\left(-iE_{\uparrow}t\right) \quad ; \quad \beta =| \beta | \exp\left(-iE_{\downarrow}t + i\phi(t)\right) \tag{2.15}$$

with $\phi(t)$ representing a drifting phase which determines the spin coherence time (which is long enough here for the precession to be well-defined), and is related to the ESR spin-relaxation time. The mechanism here is based on the time-dependent modification of the tunnelling density of states induced near the precessing spin in the presence of an applied current, (also put forwards as an explanation in [30]). The unpolarized tunnelling electrons are treated as though the local spin moment $\boldsymbol{S}$ is static for each instantaneous orientation and the correction to the conduction electrons density of states is sought. The introduction of a current to the system creates a shift of $\boldsymbol{k_0}$ to the equilibrium momentum distribution of the tunnelling electrons. This is inserted into the Greens Function of the system, which is then used to calculate the correction to the density of states. The correction depends on the distance of the tunnelling electrons from the spin centre through a Bessel Function dependence, and it was found that if $\boldsymbol{S}$ oscillated at the Larmor frequency, a time dependence of the correction is found.

Work has been done by several authors on the transmission or conductance of electrons via a molecule or other system with one or two energy levels. Zhu and Balatsky [47], find that a Larmor oscillation in the conduction is found when tunnelling through a precessing spin if a spin-flip interaction between the conduction electrons and the single molecule is allowed. Galperin *et al.* [59] discuss using the ratio of the spectrum amplitudes at zero and the Larmor frequency as a measure of the spin-dependant tunnelling. They use a two-lead Kondo model which consists of, amongst other terms, tunnelling matrix elements due to the exchange interaction for the electrons tunnelling from the leads to the molecule, and a direct tunnelling matrix element. They assume the exchange tunnelling is much smaller than the direct tunnelling component and the total magnetic field is given as a sum of the external applied field and the additional field produced by the tunnelling electrons. They find an expression for the zero-frequency power spectrum that relies on the angle of the tunnelling electrons' polarization with the external field.

Summary

A recent experiment by Durkan *et al.* [29], claimed to have detected the presence of a single electron spin via the modulation of an STM current through the organic molecule BDPA. Placed in a magnetic field, an STM tip was held stationary over the molecule and a modulated tunnelling current was observed. The frequency of the modulation was the same as the Larmor frequency of the free electron, suggesting that the local spin was somehow coupled to the tunnelling electrons. There is no obvious reason in this experiment though, with only a steady magnetic field, why the local spin should be precessing.

Possible theoretical explanations include a time-dependent modification of the conduction density of states induced near the precessing local spin by the presence of an applied current, and magnetic defects causing a $1/f$ noise in the tunnelling electrons which then couple to the local spin spectrum.

There are two approaches to take when studying these experiments:

1. If the local spin is precessing, under what mechanism is it doing so (knowing that it is expected to be pointing in the equilibrium magnetisation direction)?
2. Assuming the local spin *is* precessing, how does this motion project itself into the tunnelling current spectrum?

We aim to examine both approaches, starting with the assumption that the local spin is not precessing.

Chapter 3

Tunnelling Through a Barrier

In this chapter we attempt to understand the form of an electron current as it passes an impurity which is inside the vacuum barrier of an STM. We treat the leads of the experiment (here the STM tip and the surface) as if they are at equal potential, and the vacuum barrier is represented by a barrier wall through which the electrons must tunnel. We study the wavefunction of the incoming plane of electrons as it moves through the barrier. We are interested in the wavefunction after the barrier has been traversed. The system is treated both non-relativistically and relativistically, with and without applied magnetic fields.

In the following sections, unless otherwise stated, the barrier is treated as rectangular, of a height V_0 and a width a, starting at $z = 0$ and ending at $z = a$.

$$V(z) = \begin{cases} 0 & : \quad z < 0 \\ V_0 & : \quad 0 \leq z \leq a \\ 0 & : \quad z > 0 \end{cases} \tag{3.1}$$

3.1 Non-Relativistic Barrier Tunnelling

The method for studying quantum mechanical tunnelling through a barrier or a well is well known. We start with the general Schrödinger equation for a particle under the influence of a potential $V(z)$:

$$-\frac{\hbar^2}{2m}\nabla^2\Psi + V(z)\Psi = E\Psi \ . \tag{3.2}$$

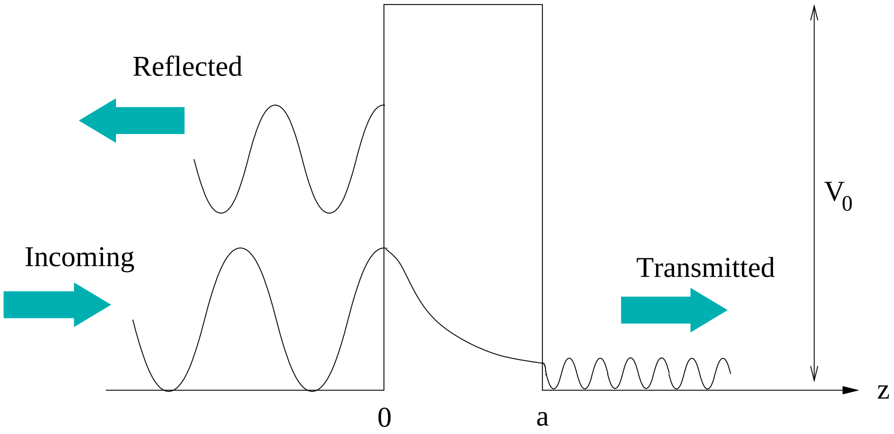

Figure 3.1: A wave approaching a barrier of height V_0 and width a. The wave decays exponentially inside the barrier and is partially transmitted on the other side. Part of the wave is reflected at the front face of the barrier (shifted upward for clarity).

The system is separated into areas of different potentials, changing the Schrödinger equation accordingly. Trial wavefunctions are substituted into the equations hopefully satisfying the Eigenvalue equation with appropriate wavevectors. Boundary conditions are then applied to the wavefunctions. They must match at the barrier boundary (must be continuous) and their derivative must also match (the wavefunctions are smooth). This ensures the model is physical. The wavefunctions must also be normalised such that $\Psi(z) \rightarrow 0$ as $z \rightarrow \pm\infty$.

3.1.1 Tunnelling with no Magnetic Field

The wave will approach the barrier from the left (Section I), and will take the form of a plane wave. In the barrier (Section II) the wave exponentially decays, and in Section III as the wave leaves the barrier we expect the wave to be a translated fraction of itself in section I. The trial solutions include both forward and backward-moving waves. The wavefunctions are chosen such that the wavenumbers k and k' are real for an incoming electron with energy E less than the barrier height V_0.

$$\Psi(z) = \begin{cases} A\exp(ikz) + B\exp(-ikz) & : \quad I \\ C\exp(-k'z) + D\exp(k'z) & : \quad II \\ AS(E)\exp(ik(z-a)) & : \quad III \end{cases} \tag{3.3}$$

The coefficients represent the wave amplitudes and $S(E)$ is the fraction of the initial wave amplitude transmitted through the barrier. These are substituted into the appropriate one-dimensional Schrödinger equation;

$$\begin{aligned} -\frac{\hbar^2}{2m}\frac{d^2}{dz^2}\Psi(z) &= E\Psi(z) \quad : \quad I,\, III \\ -\frac{\hbar^2}{2m}\frac{d^2}{dz^2}\Psi(z) + V_0\Psi(z) &= EU(z) \quad : \quad II \end{aligned} \tag{3.4}$$

to give momentum values of $k = \sqrt{2mE/\hbar}$ and $k' = \sqrt{2m/\hbar(V_0 - E)}$ for Sections (I, III) and II respectively. Boundary conditions are applied at $z = 0$ and $z = a$ such that the wavefunctions are continuous and smooth.

$$\left.\begin{aligned} A + B &= C + D \\ ikA - ikB &= -k'C + k'D \end{aligned}\right\} z = 0$$
$$\left.\begin{aligned} C\exp(-k'a) + D\exp(k'a) &= AS(E) \\ -k'C\exp(-k'a) + k'D\exp(k'a) &= ik'AS(E) \end{aligned}\right\} z = a \tag{3.5}$$

From these equations we find an expression for $S(E)$, the transmitted amplitude fraction of the wave

$$S(E) = \frac{2ikk'}{2ikk'\cosh(k'a) + (k^2 - k'^2)\sinh(k'a)} \; . \tag{3.6}$$

The current density must be conserved through the barrier such that the incident current density equals the reflected plus the transmitted current densities ($J_{\text{inc}} = J_{\text{ref}} + J_{\text{trans}}$). This can be calculated in the non-relativistic case with the expression

$$J_n = -\frac{i\hbar}{2m}(\Psi_n^*\nabla\Psi_n - \Psi_n\nabla\Psi_n^*) \; . \tag{3.7}$$

This results in the incident probability amplitude equalling the sum of the reflected (R) and transmitted (T) probability amplitudes; $1 = R + T$. R (T) is given by the square of the ratio of the reflected (transmitted) wave amplitude to the incoming wave amplitude. Specifically, the transmissivity is given by

$$T = \left| \frac{AS(E)}{A} \right|^2 = \left(1 + \frac{\sinh^2(k'a)(k^2 + k'^2)^2}{4k^2k'^2} \right)^{-1} . \tag{3.8}$$

3.1.2 Tunnelling with a Magnetic Field in the Barrier

We first postulate that the magnetic field is felt in the vacuum barrier only. There seems to be little consensus in the literature as to whether this is an accurate representation of the physical picture. It was found in Ref. [60] that STM images of p-doped InAs(110) were not changed when placed in fields of up to 6 Tesla. However, a paper the following year [61] by the same group, using fields of up to 6 Tesla detected oscillations of the conductance with a change in the magnetic field. This was through n-doped InAs(110) and the oscillations were attributed to Landau-level splitting of the conduction band of the surface. A study of Au(111) in Ref. [62] found that a magnetic field appeared to enhance standing wave patterns on the surface image, and suppress atomic imaging. However it was shown in Ref. [63] that simply changing the tip, and therefore changing the electronic structure of the tip was enough to produce this effect. The authors of [62] acknowledge that the changes could be either due to the tip or the surface and are currently investigating the effect of a magnetic field on the Au(111) surface in more detail.

With these results in mind, and the fact that the magnetic fields described above were much bigger than those used in the Durkan experiments, we decide to try both limiting the field to the barrier, and allowing it to permeate the whole of the system. We first restrict it to the barrier and choose it to be in the direction $\boldsymbol{B} = (0, 0, B)$, i.e. pointing along the short axis of the barrier.

A magnetic field results in energy differences for electrons with spins aligned with or against the direction of the field of a magnitude $\pm g_e \mu_B B$. $g_e \mu_B$ is the usual Landé g-factor and Boltzmann constant for electrons in a magnetic field of strength B. We choose the incoming electron wave to be of a generic spin formation, with equal numbers of electrons with spin up and spin down (1 and 2 respectively).

The wavefunctions are given by

$$\begin{aligned} z<0 \quad \Psi_I &= \begin{pmatrix} A_1 \\ A_2 \end{pmatrix} \exp\left(ik_0 z\right) + \begin{pmatrix} B_1 \\ B_2 \end{pmatrix} \exp\left(-ik_0 z\right) \\ 0<z<a \quad \Psi_{II} &= \begin{pmatrix} C_1 \exp\left(k_1 z\right) \\ C_2 \exp\left(k_2 z\right) \end{pmatrix} + \begin{pmatrix} D_1 \exp\left(-k_1 z\right) \\ D_2 \exp\left(-k_2 z\right) \end{pmatrix} \\ z>a \quad \Psi_{III} &= \begin{pmatrix} U_1 \\ U_2 \end{pmatrix} \exp\left(ik_0(z-a)\right) \ , \end{aligned} \tag{3.9}$$

where

$$\begin{aligned} k_0 &= \tfrac{1}{\hbar}\sqrt{2mE} \\ k_1 &= \tfrac{1}{\hbar}\sqrt{2m(V_0 - E - g_e\mu_B B)} \\ k_2 &= \tfrac{1}{\hbar}\sqrt{2m(V_0 - E + g_e\mu_B B)} \ . \end{aligned} \tag{3.10}$$

The wavefunctions and their derivatives were matched at the barrier walls ($z = 0$ and $z = a$), and were rearranged using Cramer's Rule to find the transmission and reflection coefficients ($U_{1,2}$ and $B_{1,2}$ respectively) of both spin wavefunctions. Cramer's Rule is used for solving Linear systems of non-singular matrices. The solution of $AX = B$ is given by

$$X_n = \frac{det\, A_n}{det\, A} \ , \tag{3.11}$$

where A_n is the matrix formed by replacing the nth column of A with the column matrix B. The transmitted components were calculated separately for spin up and spin down ($i = 1, 2$) and were given by

$$T_i = |U_i|^2 = \left(1 + \frac{\sinh^2(k_i a)(k_0^2 + k_i^2)^2}{4k_0^2 k_i^2}\right)^{-1} \ . \tag{3.12}$$

This is exactly the same form as for non-relativistic tunnelling with no magnetic field. We can find the polarisation of the total transmitted wave with the equation

$$P = \frac{T_\uparrow - T_\downarrow}{T_\uparrow + T_\downarrow} \ . \tag{3.13}$$

Figure 3.2 shows the polarisation result - a small excess of up spins over down spins. The difference corresponds to a spin polarisation of 1 in 50,000 for moderate magnetic fields such as used in the Durkan experiment ($0.019 - 0.03$ T). The polarisation effect is constant at low energies, then seems to increase sharply at energies very close to the barrier height. The graphs in this chapter are plotted in Atomic Units (details given in Appendix B).

Quantity	Symbol	Experimental Value	Value in A.U.
Tip Bias	V_0	0.5 – 8 eV	0.018 – 0.3 ht
Barrier Width	a	10Å	20 Bohrs
Magnetic Field	B_0	0.019 – 0.03 T	$7.6 - 12 \times 10^{-8}$ AU

Table 3.1: Experimental values and their equivalent in Atomic Units.

For the Durkan experiment, the experimental values and the equivalent values in Atomic Units are given in Table 3.1.

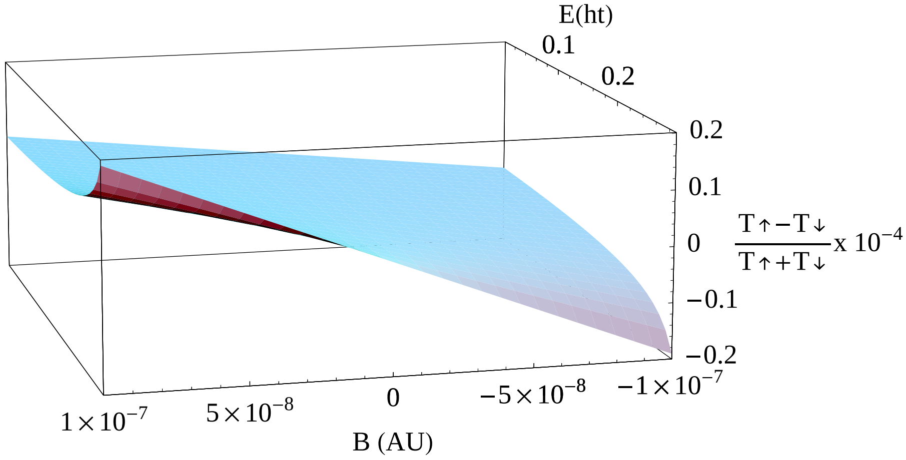

Figure 3.2: The polarisation of electrons when tunnelling through a barrier with an applied magnetic field, as a function of magnetic field and electron energy. The barrier has the dimensions; $V_0 = 0.3$ ht and $a = 20$ Bohr. The polarisation is scaled by 10^4.

In Figure 3.3 we show the behaviour of the separate spin components when the barrier height is increased; there is a small constant polarisation for low energies, a steep rise in energy when close to the barrier height, and an oscillating behaviour when the energy is greater than the barrier height (when the momentum becomes imaginary). Changing the barrier height appears to have no effect on the size or pattern of the transmission. The sole effect seems to be to move the graph in energy such that the sharp rise is always at the energy of the barrier height. The spin up component leads the spin down component, but the differences in transmission are too small to be resolved in the graphs for the magnetic fields we are interested in. It is more informative to study the polarisation.

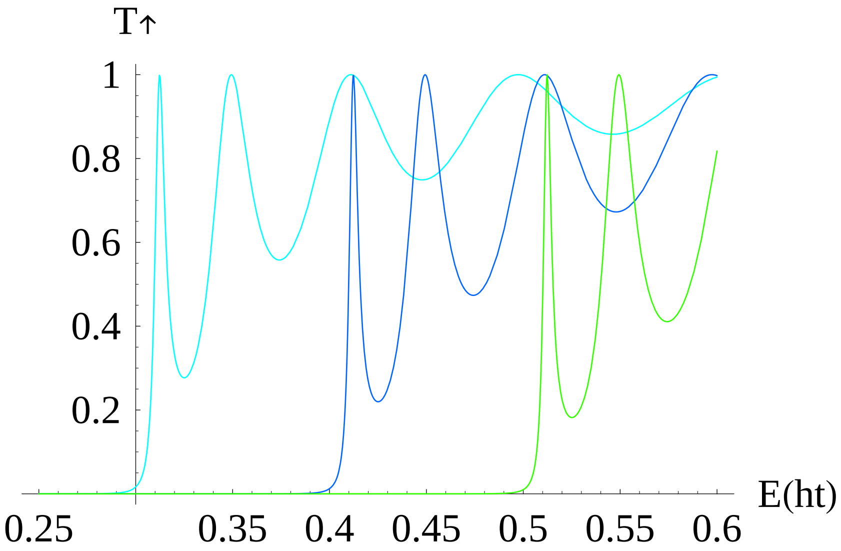

Figure 3.3: Transmission of the spin up component as a function of the electron energy for a tunnelling event with a magnetic field of $B = 1 \times 10^{-7}$ AU in the barrier. The barrier width is 20 Bohrs, and the three plots are for barrier heights of: Light Blue - 0.3 ht, Dark Blue - 0.4 ht, Green - 0.5 ht

Figure 3.4 shows how the polarisation of the transmitted wave changes as the barrier width is increased. Figure 3.4(a) shows the same barrier heights as in Figure 3.3, and Figure 3.4(b) shows the approximately linear relationship between the energy of the barrier height and the maximum polarisation. Plotted in Figure 3.4(b) is also the electron energy at which the maximum polarisation occurs; it appears to consistently occur at a slightly higher energy than the barrier height. This is slightly inside the barrier and must be an artefact resulting from the matching of the travelling wave outside the barrier and the exponentially decaying wave inside the barrier.

This difference in energy between barrier height and maximum polarisation can be seen clearer in Figure 3.5, which is a plot of the changing polarisation with increasing barrier width, a. The barrier height here is 0.3 ht and the peak of the curve for $a = 20$ Bohrs quite clearly occurs at $E \sim 0.31$ ht. As the width is increased, the polarisation is seen to

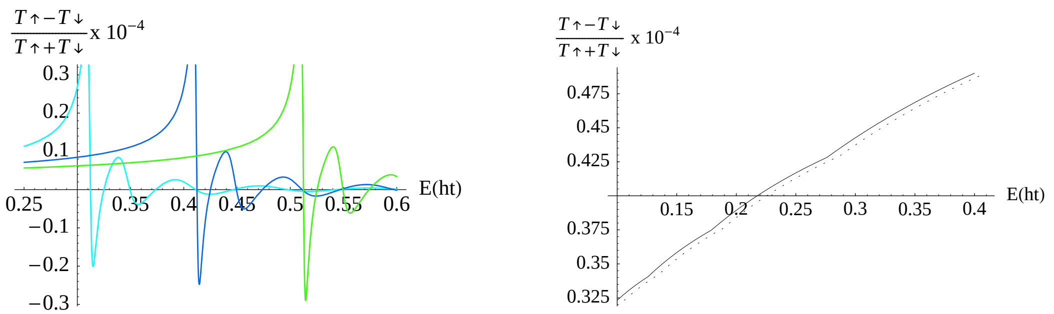

(a) When the barrier height is increased, the polarisation graph shifts in energy to the energy of the barrier height. The graphs are for the same barrier heights as in 3.3.

(b) Maximum polarisation as a function of increasing barrier height (solid line). The dashed line represents the energy at which the maximum polarisation occurs.

Figure 3.4: The dependence of the polarisation on barrier height. A magnetic field of $B = 1 \times 10^{-7}$AU is in the barrier only. The barrier width is $a = 20$ Bohrs. The polarisation is scaled by 10^4.

increase, most likely due to the influence of the magnetic field being felt over a greater distance. The rise in polarisation which is usually seen as the barrier height is approached, becomes sharper as the width is increased, and occurs at successively lower energies until the energy of the barrier is reached.

To summarise, these results appear to show that increasing the barrier height increases the energy of maximum polarisation which always occurs at an energy slightly higher than the barrier height. There seems to be no effect however on the value of the maximum polarisation. When reducing the barrier width, on the contrary, the amplitude is greatly reduced. The reduction of the barrier also increases the energy of the maximum polarisation. The width of the barrier positively affects the maximum polarisation and the location in energy appears to be solely decided by the barrier height.

3.1.3 Tunnelling with a Magnetic Field all over

We now examine the transmission and polarisation of a wave that is moving through an area of continuous magnetic field, both inside and outside of the potential barrier. This involves changing the form of the k values outside of the barrier to include the magnetic energy -

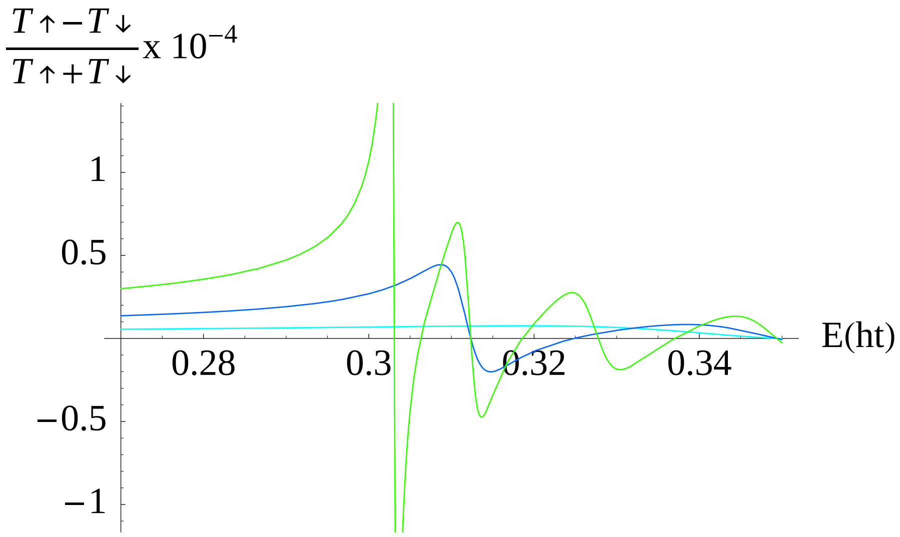

Figure 3.5: Increasing the width of the barrier with a constant barrier height of $0.3\,ht$ and a magnetic field in the barrier of 1×10^{-7} AU. Light Blue - 10 Bohr, Dark Blue - 20 Bohr, Green - 40 Bohr. The polarisation is scaled by 10^4.

$$
\begin{aligned}
k_{01} &= \sqrt{\frac{2m}{\hbar^2}(E + g\mu_B B)} \\
k_{02} &= \sqrt{\frac{2m}{\hbar^2}(E - g\mu_B B)}
\end{aligned} \tag{3.14}
$$

The momentum values inside the barrier remain the same, and the polarisation of the resulting wave after the barrier is as we might expect. It behaves much like the graph of the previous section at high energies, but is significantly different at lower energies. At very small energies, as $E \approx 0$, the wave is totally polarised in the same direction as the magnetic field (positively). As we increase the energy the polarisation reduces to being only slightly positive (as when the magnetic field was in the barrier only), then increases to the local maximum at the barrier height energy (plotted in Figure 3.6).

As we change the well dimensions, the profiles behave the same as for when the magnetic field was in the barrier only, apart from the behaviour at low energies which stays roughly constant. Comparing the polarisation graphs for the magnetic field being just in the barrier, and all over the system, we see that it is only when the energy of the electrons

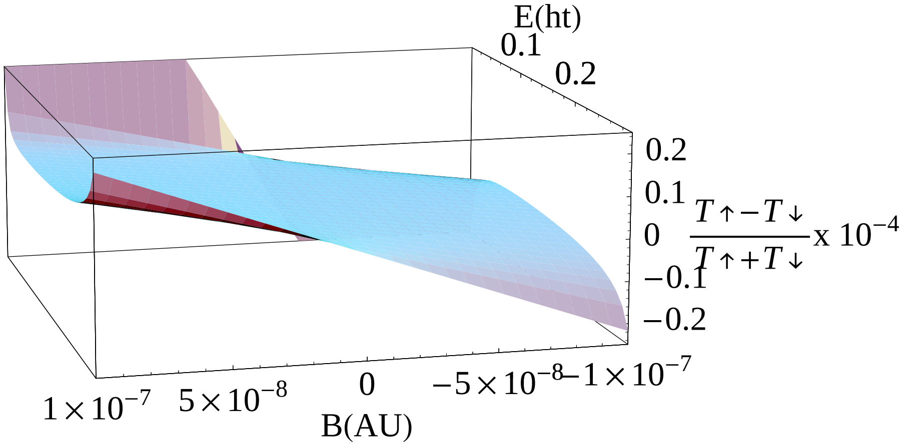

Figure 3.6: The tunnelling polarisation with a magnetic field through the whole system as a function of magnetic field and electron energy; $V_0 = 0.3$ ht and $a = 20$ Bohr. The polarisation is scaled by 10^4.

are ~ 0 that the location of the magnetic field has any effect. This is obviously due to the magnetic field being the more dominant influence at these energies.

3.1.4 Tunnelling with a Magnetic Field in the Barrier - Two-Step Barrier

In the experiment we are modelling, the electrons pass through the vacuum barrier, and then through the molecule under study. These two environments can be represented by two different potential values of two different widths. Here, we examine the effect this will have on the polarisation of the electrons. We choose the barrier to consist of two rectangular barriers placed side by side. The first barrier is of height V_1 and extends from $z = 0$ to $z = a$. The second is of height V_2 and extends from $z = a$ to $z = b$. We keep $V_1 < V_2$ for now.

The approach is the same as for the singular barrier, except there are now three barriers at which wave functions need to be matched, and correspondingly, more unknown variables. We introduce a wave function for $a < z < b$ as follows and add extra subscripts onto the momentum values to clarify which barrier we are looking at; the first number of the subscript identifies which barrier we are in, and the second represents the spin direction

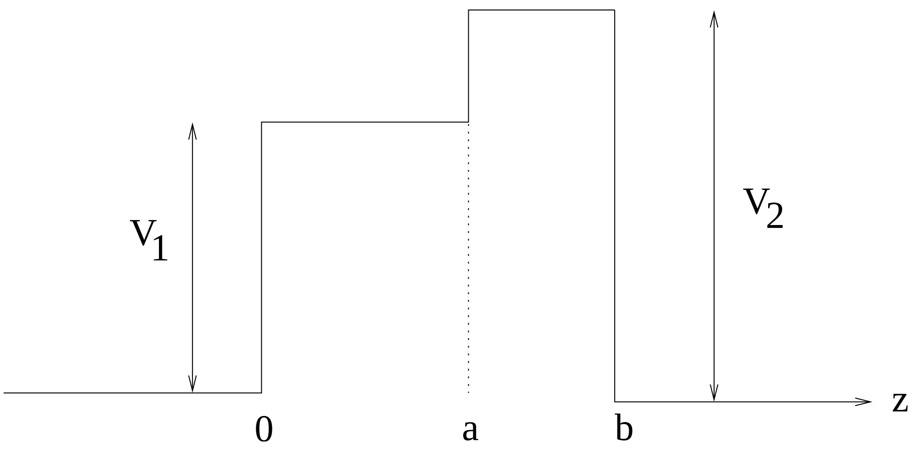

Figure 3.7: A stepped barrier consisting of two potential heights of V_1 and V_2, with widths a and b respectively. The electron wave enters from the left.

($\uparrow = 1$, $\downarrow = 2$).

$$\begin{aligned}
z < 0 \quad \Psi_0 &= \begin{pmatrix} U_1 \\ U_2 \end{pmatrix} \exp(ik_0 z) + \begin{pmatrix} A_1 \\ A_2 \end{pmatrix} \exp(-ik_0 z) \\
0 < z < a \quad \Psi_1 &= \begin{pmatrix} B_1 \exp(k_{11} z) \\ B_2 \exp(k_{12} z) \end{pmatrix} + \begin{pmatrix} C_1 \exp(-k_{11} z) \\ C_2 \exp(-k_{12} z) \end{pmatrix} \\
a < z < b \quad \Psi_2 &= \begin{pmatrix} D_1 \exp(k_{21} z) \\ D_2 \exp(k_{22} z) \end{pmatrix} + \begin{pmatrix} G_1 \exp(-k_{21} z) \\ G_2 \exp(-k_{22} z) \end{pmatrix} \\
z > a \quad \Psi_3 &= \begin{pmatrix} H_1 \\ H_2 \end{pmatrix} \exp(ik_0(z-b))
\end{aligned} \tag{3.15}$$

There are twelve boundary conditions in total; at the three distances $z = 0$, a, b we have to match the wavefunctions and their derivatives, for both of the spin directions. The trial wavefunctions are the same as those in equation (3.10), but with two different potentials now;

$$\begin{aligned}
k_0 &= \tfrac{1}{\hbar}\sqrt{2mE} \\
k_{i1} &= \tfrac{1}{\hbar}\sqrt{2m(V_i - E - g_e \mu_B B)} \\
k_{i2} &= \tfrac{1}{\hbar}\sqrt{2m(V_i - E + g_e \mu_B B)}
\end{aligned} \tag{3.16}$$

where $i = 1, 2$ refers to the potential barrier.

If we first constrain ourselves to energies less than the height of the smallest barrier, we find exactly the same shape graph as when there was only one potential. The width of the two barriers determine the polarisation of the wave in different ways. In Figure 3.8, we compare different width combinations. It appears that for optimum polarisation, it is more important for the first barrier to be thick than for the second barrier to be. A wider total barrier will give more polarisation than a thinner barrier; for a constant total width $a + b$, the highest amount of polarisation will occur when the bulk of the width is in the first potential step.

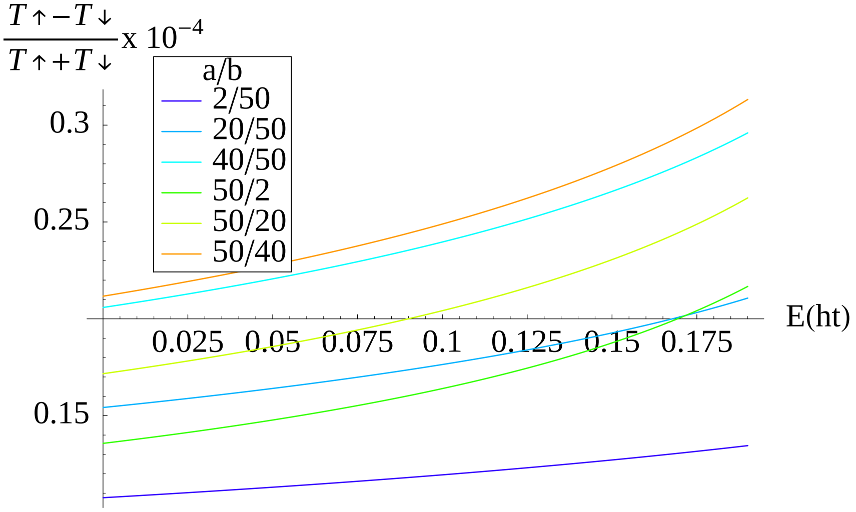

Figure 3.8: Varying individual barrier widths to determine the effect on the magnitude of the overall polarisation at energies less than the first barrier height. Barrier heights are fixed at $V_{1,2} = 0.3, 0.5$ ht, and the magnetic field is $B = 1 \times 10^{-7}$AU. Polarisation is scaled by 10^4.

If we allow the maximum energy to go above the height of the second barrier, we see two distinct regions in the polarisation graphs. Up to the energy of the first barrier, we have a smoothly varying graph which is the same as the previous graphs, with the typical peak in polarisation as the barrier energy is reached. After this, we get oscillatory behaviour until we reach the energy of the second barrier, when another peak tends to occur. The oscillations will decay if the energy gap between the barriers is wide enough. They appear to grow for $a = 10$ Bohrs in Figure 3.9, but this is due to the proximity of the next barrier, and the first barrier not being wide enough to affect the wave significantly. Above the energy of the second barrier, only quickly-decaying oscillations are observed. Changing the heights of the barriers has the same effect as the previous sections; the location of the polarisation pattern is affected but the magnitude is not.

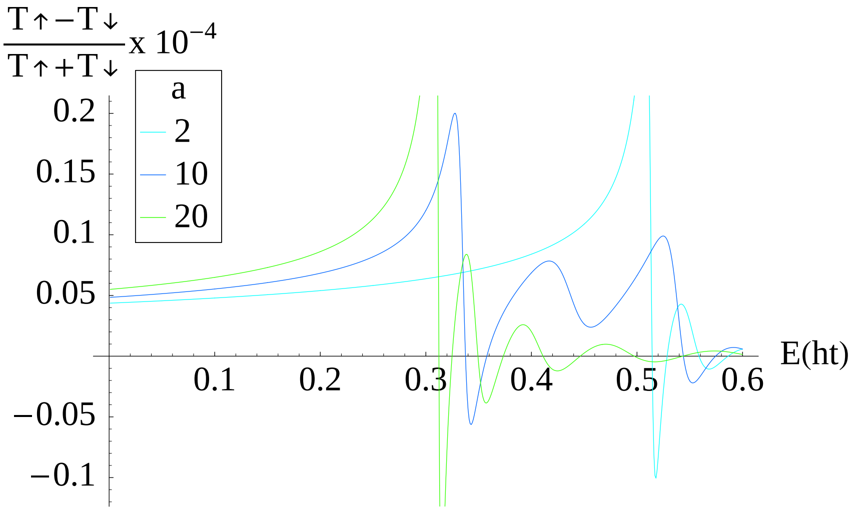

Figure 3.9: The polarisation pattern for tunnelling through a stepped barrier varying the width of the first barrier a. The barrier heights are fixed at $V_{1,2} = 0.2, 0.4$ ht, the width of the second barrier is $b = 20$ Bohr, and the magnetic field is $B = 1 \times 10^{-7}$AU. The polarisation is scaled by 10^4.

What would the polarisation look like if the wave moves through the area of largest potential first? Up to the energy of the first barrier we get constant, slightly positive polarisation until just before the second barrier height, then the characteristic peak occurs. When we look at the dependence on barrier width however, we get the opposite result from before. A greater polarisation occurs when the second barrier is wider than the first; this suggests that the polarisation is optimised for the wider potential barriers, whether they appear first or second in the barrier step, and the heights are less important in deciding the amount of polarisation. This supports the results found in the case of a single step.

In this section we have presented non-relativistic tunnelling through a barrier. The polarisation as a function of the applied magnetic field has been studied, and was found to depend mainly on the width of the barrier being tunnelled through. Comparing a composite barrier with a single step barrier, the polarisation in both cases appear to be very similar, with neither producing significantly more polarisation than the other. The change in polarisation with magnetic field is smooth in all cases and appears to be linear (Figures 3.10 and 3.2).

How do these results relate to the experimental findings? A tunnelling current can be viewed as a random ensemble of spins. We would expect such a current to be unable to coherently map the state of a single impurity spin that it passes. A spin polarisation in the tunnelling current however, may allow the impurity to affect the current in an observable manner. For the widths used in the experiments the polarisation in this model is only 1 in $50,000$; a similar sized result was found by Durkan in Ref. [54]. In 0.1 ms this corresponds to only 18 more spin up electrons than spin down electrons out of the 880,000 electrons which will pass through the junction in that time (for a 1 nA current). If we wanted to achieve total polarisation of the electron wave, for typical barrier heights and magnetic fields used in the Durkan experiment, a barrier width of ~ 0.1 mm would be needed.

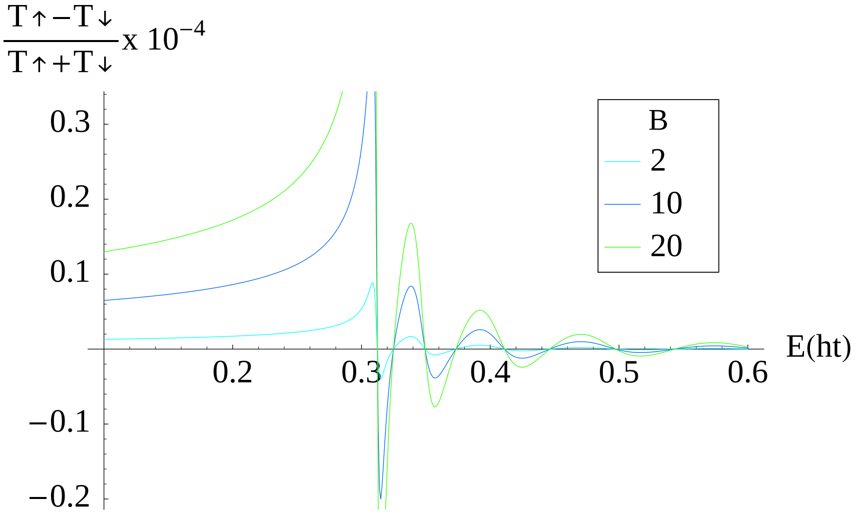

Figure 3.10: Polarisation changing with magnetic field, all B values are $\times 10^{-8}$. $V_{1,2} = 0.2, 0.4$ ht; $a, b = 20$ Bohrs. The polarisation is scaled by 10^4.

3.1.5 The Pauli Equation

The method used above to include the spin of the tunnelling electrons was not a completely rigorous approach. The full equation for non-relativistic particles with spin has been derived by Pauli. In an electromagnetic field it is given by;

$$i\hbar\frac{d\Psi}{dt} = \left(\frac{1}{2m}(\hat{p} - \frac{e}{c}\boldsymbol{A})^2 + e\phi - \mu_B\tilde{\sigma}\cdot\boldsymbol{B}\right)\Psi \tag{3.17}$$

Where ϕ is the scalar Coulomb potential and $\boldsymbol{A}$ is the vector potential related to $\boldsymbol{B} = \mathrm{curl}\boldsymbol{A}$. $\tilde{\sigma}$ represents the three Pauli spin matrices given by;

$$\tilde{\sigma_x} = \begin{pmatrix} 0 & 1 \\ 1 & 0 \end{pmatrix} \quad \tilde{\sigma_y} = \begin{pmatrix} 0 & -i \\ i & 0 \end{pmatrix} \quad \tilde{\sigma_z} = \begin{pmatrix} 1 & 0 \\ 0 & -1 \end{pmatrix} \tag{3.18}$$

If we select the magnetic field to be in the z-direction as above, the vector field can be given by $\boldsymbol{A} = \{-1/2B_y, 1/2B_x, 0\}$, and assuming the magnetic field is weak, we can ignore terms in $\boldsymbol{A}^2$. For this choice of $\boldsymbol{A}$ we get $\boldsymbol{A}\cdot\hat{p} = B/2\hat{L_z}$, and assuming the wavefunction to be comprised of a two-component Spinor as before, we find the Pauli equation goes to

$$\left(\frac{\hat{p}^2}{2m} - \frac{eB}{2m}(\hat{L_z} + \hbar\tilde{\sigma_z})\right)\begin{pmatrix} \Psi_1 \\ \Psi_2 \end{pmatrix} = E\begin{pmatrix} \Psi_1 \\ \Psi_2 \end{pmatrix} \tag{3.19}$$

for a magnetic field and no external potential. The addition of a potential will require an additional term of $+V_0\Psi$ on the left hand side of the equation.

If we use this equation to study the transmission probability of up and down spins for a magnetic field confined to the barrier region, we get the same equation for the probability as above and inputting the values of k_0, k_1, k_2, get the exact same result. So the approach above, where the spin was added in ad-hoc and the orbital angular momentum was not accounted for, was adequate for a study of the polarisation resulting from an electron wave tunnelling through a barrier.

3.2 Relativistic Barrier Tunnelling

3.2.1 Relativistic Tunnelling with no Magnetic Field

Another check we can perform to verify that we have taken account of the electron spins appropriately, is to formulate the tunnelling relativistically. We can then take the non-relativistic limit, looking at the energy range in which we are interested, but still maintaining the spin description. For this the wavefunctions must be a solution of the Dirac equation, which for a free particle is given by

$$i\hbar\frac{\partial\Psi(\boldsymbol{r},t)}{\partial t}=(c\;\tilde{\boldsymbol{\alpha}}_{\boldsymbol{r}}\cdot\boldsymbol{p}+\tilde{\beta}m_0c^2)\Psi(\boldsymbol{r},t)\;. \tag{3.20}$$

This is modified inside the barrier by the inclusion of a potential term $+V_0\Psi(\mathbf{r},t)$. $\tilde{\alpha_r}$ and $\tilde{\beta}$ are 4×4 Dirac matrices given by

$$\tilde{\alpha}_r=\begin{pmatrix}0 & \tilde{\sigma}_r\\ \tilde{\sigma}_r & 0\end{pmatrix}\;;\;\tilde{\beta}=\begin{pmatrix}\underline{\boldsymbol{I_2}} & 0\\ 0 & -\underline{\boldsymbol{I_2}}\end{pmatrix} \tag{3.21}$$

Where $r=(x,y,z)$, and $\tilde{\sigma_r}$ are the Pauli 2×2 matrices. Each of the components of the relativistic wavefunction must individually satisfy the Klein Gordan equation [64], and for tunnelling or scattering below the energy range in which particle-antiparticle pairs are created, must satisfy the probability current conservation equation, given in the relativistic case by

$$J_{i,r}=\langle\Psi_i\,|c\;\tilde{\alpha}_r|\;\Psi_i\rangle \tag{3.22}$$

with $i=(1,2)$ corresponding to $1=\uparrow,2=\downarrow$.

As in the non-relativistic calculation, we would like to confine the electrons momentum to propagate in the z-direction ($r=z$), so that $\tilde{\boldsymbol{\alpha}}_{\boldsymbol{r}}\cdot\boldsymbol{p}\rightarrow\tilde{\alpha}_z\hbar k_z$. For every momentum value, there will be two energy solutions corresponding to particles or antiparticles (holes). The relativistic energies E_R are given by the free Dirac equation;

$$E_R=\pm\sqrt{m_0^2c^4+(\hbar ck)^2} \tag{3.23}$$

We are only interested in the particles, so will only take the positive values of E_R. If we again allow waves to move in both the positive and negative direction, we find a set of wavefunctions that satisfy equations 3.20 and 3.22;

$$
\begin{aligned}
z<0 \quad \Psi_1 &= \frac{1}{\sqrt{1+f_0^2}}\begin{pmatrix} A_1 \\ A_2 \\ f_0A_1 \\ -f_0A_2 \end{pmatrix}\exp\left(ik_0z\right) + \begin{pmatrix} B_1 \\ B_2 \\ -f_0B_1 \\ f_0B_2 \end{pmatrix}\exp\left(-ik_0z\right) \\
0<z<a \quad \Psi_2 &= \begin{pmatrix} C_1 \\ C_2 \\ -if'C_1 \\ if'C_2 \end{pmatrix}\exp\left(k'z\right) + \begin{pmatrix} D_1 \\ D_2 \\ if'D_1 \\ -if'D_2 \end{pmatrix}\exp\left(-k'z\right) \qquad (3.24) \\
z>a \quad \Psi_3 &= \begin{pmatrix} U_1 \\ U_2 \\ f_0U_1 \\ -f_0U_2 \end{pmatrix}\exp\left(ik_0(z-a)\right)
\end{aligned}
$$

Where

$$
\begin{aligned}
f_0 &= \frac{\hbar c k}{E+2m_0c^2} & k_0 &= \frac{1}{\hbar c}\sqrt{E^2+2Em_0c^2} \\
f' &= \frac{\hbar c k'}{E-V_0+2m_0c^2} & k' &= \frac{i}{\hbar c}\sqrt{(V_0-E)(V_0-E-2m_0c^2)}
\end{aligned} \qquad (3.25)
$$

The relativistic energy in the wavefunctions have been re-written as a sum of the rest mass energy and the non-relativistic energy $E_R = E + m_0c^2$. We match the wavefunctions at $z = 0$ and $z = a$, and solve for the transmission and reflection coefficients, U and B. If the wave has no spin polarisation, we find the transmission probabilities of the up and down spin components to be equal;

$$
T = \left(1 + \frac{\sinh^2(k'a)(f_0^2+f'^2)^2}{4f_0^2f'^2}\right)^{-1} \qquad (3.26)
$$

We modify our wavefunctions to observe what happens if we look at a polarised wave. For total spin polarisation, (say $A_2 = 0$), we observe no reflected or transmitted component in the opposite (down) spin channel. The two spin channels do not interfere with each other and are transmitted completely separate of each other.

3.2.2 Relativistic Tunnelling with a Magnetic Field

As shown by [65] the magnetic field can be introduced into the relativistic electron tunnelling via the following modification of the Dirac equation;

$$\imath\hbar\frac{\partial\Psi(\boldsymbol{r},t)}{\partial t}=(c\,\tilde{\boldsymbol{\alpha}}\cdot\boldsymbol{p}+\tilde{\beta}m_0c^2+V_0-g\mu_B B\cdot\sigma_i)\Psi(\boldsymbol{r},t)\;. \tag{3.27}$$

Outside the barrier, the electrons must still satisfy the free-particle Dirac equation given in (3.20) and again, we take the direction of interest to be the z direction. The same wavefunctions are used but we modify the equation components f', k' to be:

$$f_1=\frac{\hbar ck_1}{E+2m_0c^2-V_0+g\mu_B B}\qquad f_2=\frac{\hbar ck_2}{E+2m_0c^2-V_0-g\mu_B B} \tag{3.28}$$

and change k' to k_1 and k_2 as follows;

$$\begin{aligned} k_1 = &\ \frac{1}{\hbar c}\sqrt{(V_0-E-g\mu_B B)(E+2m_0c^2-V_0+g\mu_B B)} \\ k_2 = &\ \frac{1}{\hbar c}\sqrt{(V_0-E+g\mu_B B)(E+2m_0c^2-V_0-g\mu_B B)} \end{aligned} \tag{3.29}$$

Analytically, these components generate transmission probabilities similar to equation 3.26, with f' and k' exchanged for f_1, k_1 for spin up, and f_2, k_2 for spin down. Because we have taken care to write the relativistic components in terms of non-relativistic energies we can directly compare the polarisation given by this method to the non-relativistic values (Figure 3.11).

We see that the non-relativistic approach gives much the same results as the relativistic approach. The greatest discrepancy is at low energies, but as the difference is only of the order of $\sim 10^{-11}$, is considered to be negligible. Even if we consider relativistic tunnelling through a barrier with two different heights, the difference between the relativistic and non-relativistic case remains small. This is illustrated in Figure 3.12, where we plot the polarisation difference between the both models for changing magnetic field strengths (the data in Figure 3.10 minus its relativistic equivalent).

The wavefunctions consist of Large and Small components (the upper and lower two entries respectively). If we take the non-relativistic limit in which $v/c \to 0$, the small components (f_1, f_2) go to 0, and we are left with the Large components only. The relativistic normalisation term $1+f_0^2$ goes as $1+(\hbar k/mc)^2 \to 1+v^2/c^2 \to 1$, and the k values all reduce to

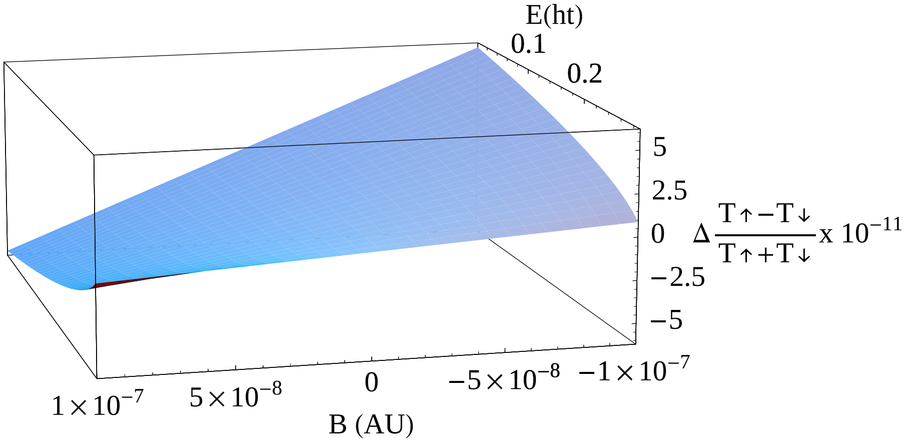

Figure 3.11: The polarisation difference between relativistic and non-relativistic tunnelling through a barrier in a magnetic field. Barrier height = 0.3 ht, barrier width = 20 Bohr. The polarisation has been scaled by 10^{11}.

their appropriate non-relativistic values to recover the non-relativistic transmission probabilities of the earlier sections. Both the algebraic and the graphical data suggest that the non-relativistic model is an appropriate form to describe the electronic spin behaviour in this case and for the low energies we are interested in, and moving to a relativistic format is not needed.

3.3 Conclusions

This work has shown that tunnelling through an area with an applied magnetic field is enough to introduce a slight polarisation of an originally unpolarised tunnelling current. When experimental parameters are used in the model, the resulting polarisation is very small - 1 in $50,000$. Is there any way in which the polarisation could actually be larger in the Durkan spin-detection experiment? The two obvious ways to increase the polarisation seem to be to increase the magnetic field strength used, and to increase the tunnelling barrier width: The longer the free electrons are subjected to the field (i.e. the width of the tunnelling barrier), the more polarised they become. The magnetic field strength cannot be increased by accident in the experiment as it was supplied by a permanent magnet

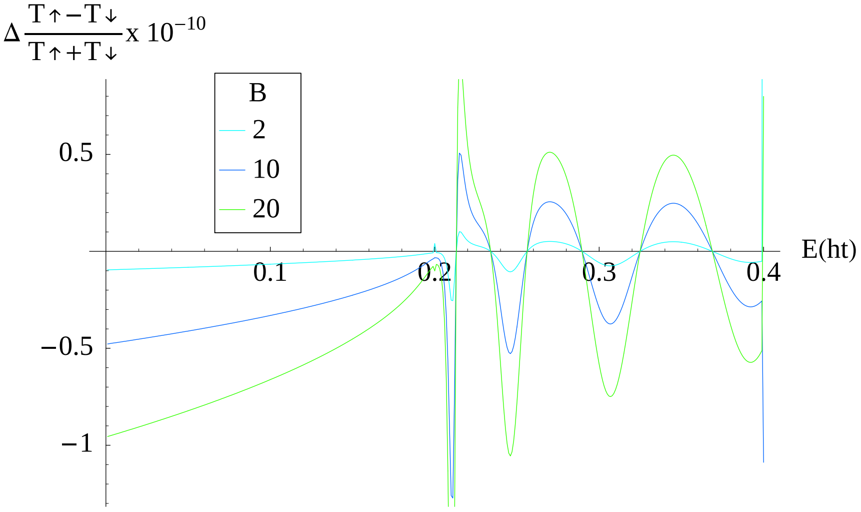

Figure 3.12: The difference between the relativistic and non-relativistic polarisation for various magnetic field values in a stepped barrier. All B values are $\times 10^{-8}$. $V_{1,2} = 0.2, 0.4$ ht; $a, b = 20$ Bohrs. The polarisation is scaled by 10^{10}.

situated under the sample. The tunnelling barrier is also unlikely to have increased by large amounts unnoticed as the image quality would have degraded in the process. It would appear then, based on the results of this model, that only a very small polarisation of the tunnelling electrons occurs.

This model was only intended to describe the state of the tunnelling current as it passed a magnetic field. When modeling the molecule as having a different potential to the surface as we did in the two-step barrier, we didn't include any interactions between the molecule and the tunnelling current. We didn't include the spin of the molecule which is obviously the next step to take. Moving to a relativistic framework didn't give any further insights into the problem as we found that it was sufficient to include the spin in the non-relativistic method in an ad-hoc manner.

From this we conclude that a further investigation will require a different model, one in which we can use our result of a slight polarisation and study the effect this will have on the molecular spin.

Chapter 4

The Non-Relativistic Delta Shell Model

In the experiment performed by Durkan *et al.* [29], the tunnelling current measured had an a.c. component whose frequency was directly correlated to the magnetic field it passes through. It therefore appears that the motion of the tunnelling electrons is somehow related to their spin. The other condition which must be satisfied before this effect is seen, is that the electrons must tunnel into a molecule with a non-zero spin component. This suggests that the spin of the electrons are interacting with the spin of the molecule.

Because spin is a relativistic effect, to effectively model this interaction requires a move into a relativistic framework. Although the experiment isn't performed on relativistic energy scales, we can frame the problem relativistically and then take a low energy limit, retaining spin interaction terms.

The effect we are looking for has been seen in studies of organic molecules and silicon spin centres. It has been observed with several different tips, not necessarily of the same geometry and not all made from the same material. These details suggest that the electronic structure of the tip and the molecule will not be important when modeling the experiment. It has been shown in [66] that two different tip models - a parabolic etched tip and a cleaved triangular tip ending in a single atom - experience the same force as each other (to the same order of magnitude). As the experiment is not claiming to be imaging to atomic resolution, we may be able to use a model in which the tip isn't known or described exactly, as long as we do not assume the results to be numerically exact.

Possible extensions to the experiment include the use of spin polarised STM tips. It would be good to include this possibility when creating a model. Both of the above points suggest that a good choice of model would be one in which the experimental parameters were not an integral part of the derivation, and could be varied easily to model different tips and molecules.

In the experiments we hope to model, the electrons first interact with (leave) the tip then cross the vacuum barrier. They then pass through the molecule, somehow interacting with its spin, and then carry on into the surface. The geometry of the system naturally breaks up the problem into the smaller parts shown in Figure 4.1. Rather than trying to solve the problem as a whole, we decide to examine separately the effect of each component on the electron wave, and then combine them to try to understand the influence each potential has.

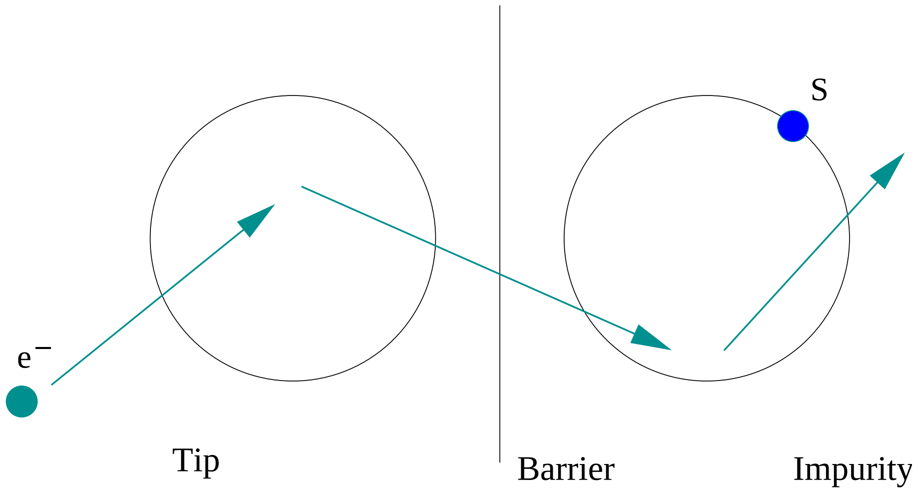

Figure 4.1: The component parts of the STM system. The tunnelling electrons interact with the tip, pass through the barrier, then interact with the deposited molecule and its spin (shown as S). They then continue onward into the substrate.

This is an improvement over the method used in the previous chapter as then, the tunnelling barrier represented the electrons leaving the tip, passing through the vacuum barrier, then entering the surface all in one step. This new approach will allow individual tuning of parameters, and is a logical way to build up a model. To do this we choose to move away from wave-matching at a boundary and instead treat the tip and deposited molecule (hereafter called the impurity) as scattering centres which the incoming electron wave can interact with. This will allow us to consider the circumstances under which an electron will be bound (caught) by the tip or impurity, as well as being able to study what happens to the electrons when they scatter from them.

We model the system in this separable manner over the next few chapters. We model the potential of the tip and the impurity as spherically symmetric Delta Shell potentials. We can introduce a spin onto one of the potentials to represent the impurity spin which can be either static or precessing. By changing to a relativistic framework we can include the spin of the tunnelling electrons. Once the effect of the separate parts of the system are known, they can be combined to determine the likelihood of scattering from the entire system.

In this chapter we start by formulating a non-relativistic model using the Delta Shell potential to model the STM tip. We first describe some of the techniques we will be using to look at the bound states and scattering states of our potentials. We then review other work in the literature that uses the Delta Shell potential. The model is then formulated and the bound states, scattering states and phase shifts are found.

4.1 Background

4.1.1 Bound States, Scattering States, Phase Shifts and Resonances

Bound states occur for attractive potentials only. A particle will become trapped by a potential and be considered a localised bound state if its energy is lower than the potential energy. A *critical* potential is the potential which will support states of zero energy.

If a particle has an energy greater than the potential energy scattering states start to emerge.

Phase shifts (δ_l) represent a means to study these states. When a particle interacts with a potential, there is a change in phase of the wavefunction (the amplitude is not affected). A phase shift of $\pi/2$ implies strong scattering, and a phase shift of 0 or π implies weak scattering [67]. We observe a negative phase shift when the potential is repulsive, and a positive phase shift for an attractive potential. The shape of the phase shift however, doesn't uniquely define the form of the potential [68].

When studying scattering from a nucleus, the phase shifts may be obtained by joining up the solutions inside the nucleus to the Coulomb solutions outside, at the boundary of the nucleus [69]. In that scenario, the phase shift can be given mathematically by $\tan\delta_l = B/A$. The coefficients B and A, are the prefactors of the regular and irregular solutions to the radial part of the differential Schrödinger equation. The phase shift can be defined in other ways, and it is possible to express scattering and transition amplitudes in terms of them. The outgoing wave after interaction with a potential is described by the Scattering- or S-Matrix given by $\exp(2i\delta_l)$, and the Transition- or T-Matrix through the potential can be expressed as $T = \exp(i\delta_l)\sin\delta_l$. The phase shifts can also be found from integral equations which prove useful when working in approximate limits [70].

An effect in which the electron becomes 'almost bound' can occur when a particle is temporarily captured by a potential. This is called a resonance effect and looks like a stationary (bound) state for a particular length of time. This occurrence of a temporary resonance state can be detected through the phase shift. As the particle energy passes through the resonant energy, the value of the phase shift will increase through an odd multiple of $\pi/2$.

There are two types of resonance that can occur; a sharp resonance, which occurs when the phase shift increases rapidly with energy through an odd multiple of $\pi/2$, and a broad resonance which occurs when the phase shift changes more slowly, and changes negatively with energy. In Ref. [71], Wigner states that

> *one will expect η [the phase shifts] to decrease slowly between resonances and increase fast at resonances,*

referring to the broad and sharp resonances respectively. The sharp resonances are regarded as the 'true' resonances. The scattered wave is retarded in space from the incident wave due to the potential, and this length given as $2\,d\eta/dk$ by Wigner, can be converted into a time called the 'Wigner delay time'

$$t_l^D = 2\hbar\frac{d\,\delta_l(E)}{d\,E}\ , \tag{4.1}$$

from which the width of the resonance (dE) can be found. Resonances will only occur up to a particular energy for a given potential strength. This energy cut-off is an indication of when the potential barrier becomes too permeable to support these 'resonance' states [68]. For electron energies much higher than the potential energy, the potential will not affect the electron in any appreciable way.

4.1.2 The Delta Shell Potential

The Delta Function potential is well-known as a simplistic mathematical tool with which bound states, phase shifts and singularities can be studied [68]. There are many instances in the literature of studies made on the effect of Delta functions and Delta Shell potentials on non-relativistic and relativistic particles, in both configuration and momentum space, with or without the addition of another potential type [72, 73]. The potential we are interested in is a Delta Shell potential given by;

$$V(\boldsymbol{r}) = -g\delta(\mid \boldsymbol{r} \mid - a) \tag{4.2}$$

g is the interaction strength and a is the range of the potential (referring to the actual size of the delta shell). This form of the potential is for a shell centered on the origin such that the potential is only felt by a particle a radius a from the origin. It can however be easily moved in space by introducing an off-set to the delta function; $\boldsymbol{r} \rightarrow \boldsymbol{r} - \boldsymbol{r_0}$.

The Delta Shell model is simple but has limited flexibility. The potential strength and the radius of the shell can be changed, but the nature of the potential is intrinsically short-ranged. We could conclude from this that the model is rather idealistic and of little use when describing real experiments. Other theoretical approaches to the STM problem were discussed in Chapter 2, and turn out to be more suitable for quantitative simulation. However the spherical symmetry of the model simplifies the analysis and encourages the use of partial wave decompositions, all the features of the experiment can be drawn together without too much difficulty, and this also proves to be a useful model when calculating a first approximation to low energy nuclear reactions [68], describing hyperfine interactions [73], or simulating strong interactions in hadronic atoms [74]. The Delta Shell potential also proves to be one of the few potentials exactly solvable in both the Schrödinger and

Dirac equation, (adding it to the Coulomb potential).

We start our examination of the STM tip with work carried out by Villarroel [75]. This work is carried out in momentum space without the need to match wave functions at the boundaries between areas of different potential. The bound state spectrum for non-relativistic and relativistic particles has been calculated, of which we will study the non-relativistic results below before going on to formulate a theory for describing the scattering states and resonances caused by a Delta Shell potential.

Rescaled Units

Throughout this work, as well as working in Atomic Units, the parameters of the model and the energy values are rescaled to dimensionless values symbolised with a tilde. The quantity we rescale with is

$$E_0 = \frac{\hbar^2}{2ma^2} \ , \tag{4.3}$$

giving the energy, potential strength and momentum as

$$E = \tilde{\xi} E_0 \quad g = \tilde{g} E_0 a \quad k = \sqrt{\frac{\tilde{\xi}}{a^2}} \ . \tag{4.4}$$

As we always use Atomic Units, where $\hbar = m = 1$; $E_0 = 1/2a^2$ (a is the radius of the potential shell). Details of the Atomic Units are to be found in Appendix B.

4.2 Bound States in a Delta Shell Potential

The energy spectrum of non-relativistic bound states, as found in Ref. [75] are given in terms of Modified First and Third Order Bessel Functions as

$$\frac{1}{\tilde{g}} = I_{l+1/2}\left(\sqrt{-\tilde{\xi}}\right) K_{l+1/2}\left(\sqrt{-\tilde{\xi}}\right) \ . \tag{4.5}$$

They are plotted in Figure 4.2 for the first three angular momentum values. It is apparent from the figure that a minimum potential must exist for a bound state to occur. For an electron of zero energy, this potential strength is given as equal to $2l + 1$, where l is the angular momentum value.

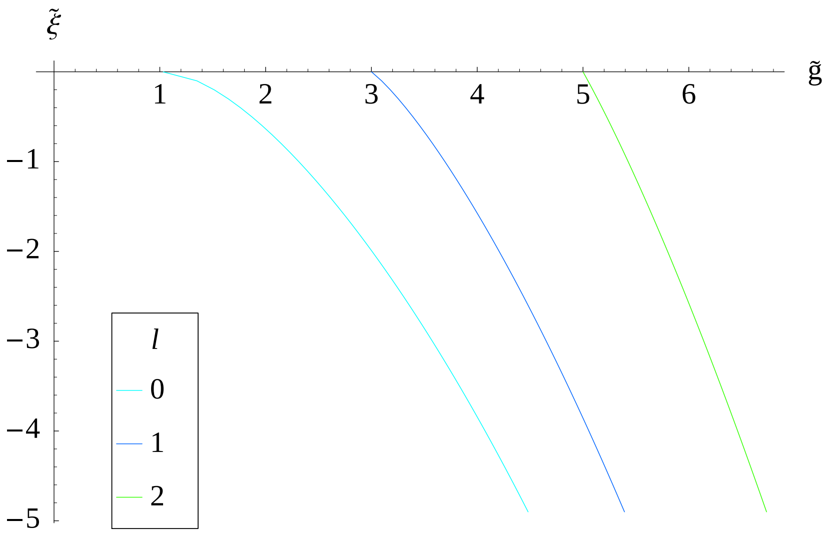

Figure 4.2: The occurrence of non-relativistic bound states for the first three angular momentum states, expressed as a function of particle energy and potential strength. A minimum potential of $2l + 1$ is required for a bound state to exist.

The bound states of the Delta Shell Potential were also found by Gottfried [68] working in coordinate space and using wave-matching techniques for inside and outside of the potential shell of radius a. He uses the partial wave solution of the integral radial Schrödinger equation;

$$A_l(k;r) = j_l(kr) + \int_0^\infty G_k^l(r;r')U(r')A_l(k;r')r'^2\,dr' \tag{4.6}$$

[$G_k^l(r;r')$ contains a Green's Function, and $j_l(kr)$ is the First Spherical Bessel Function given by $j_l(kr) = (\frac{\pi}{2kr})^{\frac{1}{2}} J_{l+\frac{1}{2}}(kr)$].

Substituting $U(r')$ for the Delta Shell potential, Gottfried shows the result

$$A_l(k;r) = j_l(kr) + ikga^2 A_l(k;a) \times \begin{cases} j_l(kr)h_l(ka) & : \quad a > r \\ j_l(ka)h_l(kr) & : \quad r > a \end{cases} \tag{4.7}$$

with

$$A_l(k;a) = \frac{j_l(ka)}{1 - ikga^2 j_l(ka)h_l(ka)} \,. \tag{4.8}$$

h_l is the Spherical Hankel Function given by the sum of Spherical Bessel and Neumann

Functions, $j_l + in_l$. By considering $A_l(k; r)$ to be a function of the complex variable $k = i\alpha$, Gottfried shows that $A_l(k; r)$ has poles on the positive imaginary k-axis at $i\sqrt{2m|E|/\hbar^2}$. These positions relate to the energy eigenvalues of the bound states; by finding the poles of the radial equation solution, we find the bound states of the potential. It transpires that the poles are to be found from the zeros of the denominator of $A_l(k; r)$. He searches for the least potential that can bind a state of angular momentum l and finds the same result as Villarroel, namely that $g = 2l + 1$. We will often return to this comparison of results from the coordinate space method, and the momentum space approach as a check on our method.

4.3 Scattering from a Delta Shell Potential

4.3.1 The Transition Matrix

In this section we consider the amplitude for the transition of the electrons from a momentum state of $\boldsymbol{k}$ to one of $\boldsymbol{k'}$ via an interaction with the Delta Shell potential. This can represent the scattering of the incoming electrons from the tip, which is shown pictorially in Figure 4.3.

The transition matrix, or t-matrix is given by the Lippman-Schwinger equation [70], which is written in the integral form

$$t(\boldsymbol{k'}, \boldsymbol{k}; E) = V_{\boldsymbol{k'},\boldsymbol{k}} + \int d^3k'' V_{\boldsymbol{k'},\boldsymbol{k''}} G_0^R(\boldsymbol{k''}; E) t(\boldsymbol{k''}, \boldsymbol{k}; E) \ , \tag{4.9}$$

where $G_0^R(\boldsymbol{k''}; E)$ is the Retarded Green's Function. In coordinate space the Green's Function describes the propagation of electrons from a point source at $\boldsymbol{r'}$ to $\boldsymbol{r}$, and is a solution to the operator equation for the Hamiltonian H; $G = (E - H)^{-1}$. A good description can be found in Ref. [70]. In momentum space $G_0^R(\boldsymbol{k''}; E)$ is given by

$$\left(\frac{\hbar^2 \varkappa^2}{2m} - \frac{\hbar^2 k''^2}{2m} + i\delta \right)^{-1} \ , \tag{4.10}$$

where $\varkappa$ is the free parameter representing the momentum of the electrons.

The transition we are calculating in (4.9) is shown in Figure 4.4. The whole scatter is modeled as a direct scatter from the potential between the initial and the final state, plus

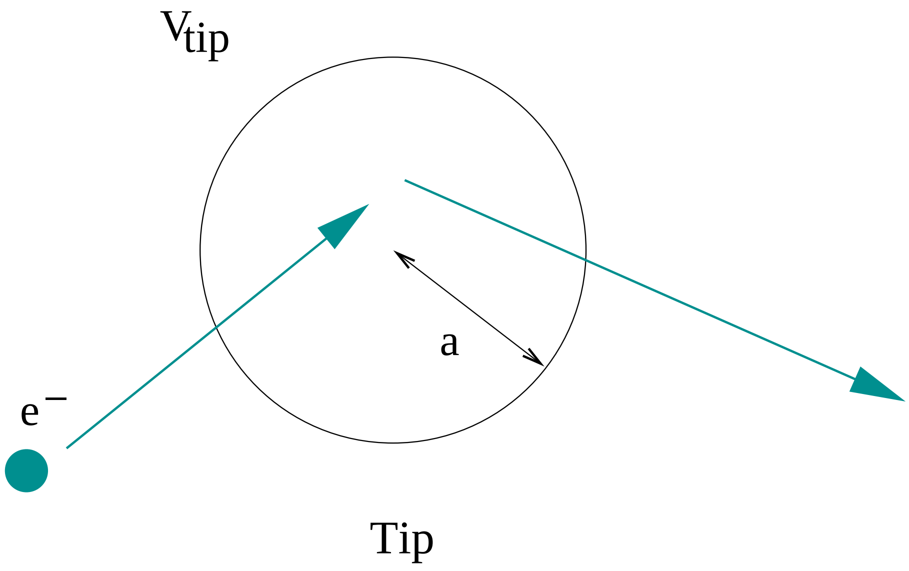

Figure 4.3: The model of the STM tip in the Delta Shell Model. The potential is given by $V(\boldsymbol{r}) = -g\delta(\mid \boldsymbol{r} \mid - a)$, where a is the radius of the potential shell, and g is the strength of the interaction.

a perturbation to the scatter, represented as an intermediate scatter through the state k''. The potential in momentum space is given by the Fourier Transform of equation (4.2)

$$V_{\boldsymbol{k'},\boldsymbol{k}} = \langle \boldsymbol{k'} \mid V \mid \boldsymbol{k} \rangle = \frac{1}{(2\pi)^3} \int V(\boldsymbol{r}) \exp\left(i(\boldsymbol{k'} - \boldsymbol{k}) \cdot \boldsymbol{r}\right) d^3 r \ . \tag{4.11}$$

The incoming and outgoing plane waves are expanded into spherical waves using the Spherical Harmonic identity

$$\exp\left(i\boldsymbol{k} \cdot \boldsymbol{r}\right) = 4\pi \sum_{L} i^l j_l(kr) Y_L^*(\hat{\boldsymbol{k}}) Y_L(\hat{\boldsymbol{r}}) \ , \tag{4.12}$$

where $L \equiv l, m$, the orbital and azimuthal angular momentum quantum numbers, and $j_l(kr)$ is the Spherical Bessel Function defined previously.

The orthonormality of the Spherical Harmonics introduces a Delta Function in $\hat{\boldsymbol{r}}$, and integrating over this we find

$$V_{\boldsymbol{k'},\boldsymbol{k}} = \frac{-2ga^2}{\pi} \sum_{L} Y_L^*(\hat{\boldsymbol{k}}) Y_L(\hat{\boldsymbol{k}}') j_l(ka) j_l(k'a) \ . \tag{4.13}$$

To calculate the t-matrix we expand it in terms of the angular momentum numbers l and m to get

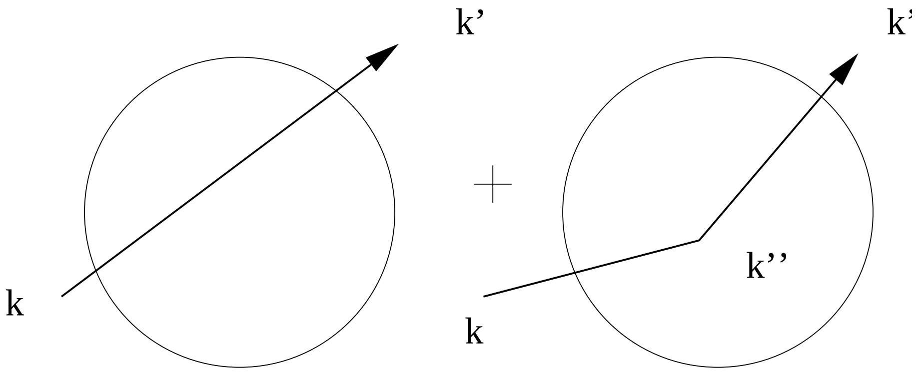

Figure 4.4: The scattering model represented by the Lippman-Schwinger equation for the transition matrix; Scattering from a momentum k to k' via an intermediate momentum, k''

$$\langle \boldsymbol{k'} \mid t(E) \mid \boldsymbol{k} \rangle = \sum_{L,L'} Y_{L'}(\hat{\boldsymbol{k}}') Y_L^*(\hat{\boldsymbol{k}}) \langle k'L' \mid t(E) \mid kL \rangle \ . \tag{4.14}$$

If we put this, and equation (4.13) into (4.9), we find that an algebraic solution only exists if $\langle k'L' \mid t(E) \mid kL \rangle$ can be further split up into separate energy and momentum components;

$$\langle k'L' \mid t(E) \mid kL \rangle = j_l(ka) j_l(k'a) t(E)\, \delta_{LL'} \tag{4.15}$$

There are now a matching pair of Spherical Harmonics and Bessel Functions in each term of the t-matrix equation, so the equation can be simplified to give

$$\begin{aligned} t_{L'L}(E) &= V_l\, \delta_{L'L} + V_l\, g_l(E_{k''})\, t_{L'L}(E) \\ &= \frac{V_l}{1 - V_l\, g_l(E)} \delta_{L'L} \ . \end{aligned} \tag{4.16}$$

V_l represents the remaining constant from the potential term $-2ga^2/\pi$, and $g_l(E_{k''})$ is given by

$$g_l(E_{k''}) = \int_0^\infty \frac{k''^2 j_l^2(k''a)}{\dfrac{\hbar^2 \varkappa^2}{2m} - \dfrac{\hbar^2 k''^2}{2m} + i\delta}\, dk'' \tag{4.17}$$

4.3.2 Solving $g_l(E_{k''})$

$g_l(E_{k''})$ can be split into two terms, factorising the constants and changing the integration term to be over the product $k''a$ rather than k''. We also take out a minus sign from the denominator to make a form that will be more useful to us further on.

$$\frac{-2m}{2\hbar^2\varkappa a^2}\left\{\int\limits_0^\infty \frac{(k''a)^2 j_l^2(k''a)}{(k''a)-(\varkappa a)-i\eta}d(k''a)-\int\limits_0^\infty \frac{(k''a)^2 j_l^2(k''a)}{(k''a)+(\varkappa a)+i\eta}d(k''a)\right\} \tag{4.18}$$

The limits of integration can be expanded to $-\infty$ and each integral is split into a 'Principal' part $\mathcal{P}$, and a remainder part using the following relationships:

$$\begin{aligned}\int\limits_{-\infty}^{\infty}\frac{A(x)}{x-\omega+i\delta}\,dx &= \mathcal{P}\int\limits_{-\infty}^{\infty}\frac{A(x)}{x-\omega}\,dx - i\pi A(\omega)\\ \int\limits_{-\infty}^{\infty}\frac{A(x)}{x+\omega-i\delta}\,dx &= \mathcal{P}\int\limits_{-\infty}^{\infty}\frac{A(x)}{x+\omega}\,dx + i\pi A(-\omega)\end{aligned} \tag{4.19}$$

As $(k''a)^2 j_l^2(k''a)$ is even, $A(-\omega)=A(\omega)$ so the two remainder terms add, and the principal parts can be recombined. This gives the following expression for $g_l(E_{k''})$

$$\frac{-2m}{\hbar^2 a}\int\limits_0^\infty \frac{(k''a)^2 j_l^2(k''a)}{(k''a)^2-(\varkappa a)^2}d(k''a)-\frac{im\pi\varkappa}{\hbar^2}j_l^2(\varkappa a) \tag{4.20}$$

The integral is exactly solvable and is given in a paper by J Dörr for Bessel Functions of the First Kind [76];

$$\int_0^\infty \frac{tJ_m^2(t)}{t^2-s^2}dt = -\frac{\pi}{2}J_m(s)N_m(s) \tag{4.21}$$

where $N_m(s)$ is a Neumann Function of the First Kind. This is transformed into Spherical Bessel Functions and gives the result

$$g_l(E_\varkappa)=\frac{m\pi\varkappa}{\hbar^2}j_l(\varkappa a)n_l(\varkappa a)-\frac{im\pi\varkappa}{\hbar^2}j_l^2(\varkappa a) \tag{4.22}$$

So finally the energy component of the t-matrix is

$$t_l(E_\varkappa)=\frac{-2ga^2\hbar^2/\pi}{\hbar^2+2ga^2m\varkappa j_l(\varkappa a)n_l(\varkappa a)-2iga^2m\varkappa j_l^2(\varkappa a)} \tag{4.23}$$

The same solution for the t-matrix is calculated by Gottfried in [68] using a partial wave expansion method and obtained by matching radial wavefunctions at large r as was mentioned in the previous section.

4.3.3 The Scattering Matrix and Phase Shifts

The scattering matrix (s-matrix) is related to the t-matrix by the following relation [77],

$$\langle \boldsymbol{k'} \mid S \mid \boldsymbol{k} \rangle = \delta^{(3)}(\boldsymbol{k'} - \boldsymbol{k}) - 2\pi i \delta(E_{k'} - E_k) t(\boldsymbol{k'}, \boldsymbol{k}; E) \tag{4.24}$$

The delta functions ensure momentum and energy conservation in the scattering process; we operate ‘on the energy-shell’ looking at elastic collisions only.

We can expand the s-matrix, the t-matrix, and the delta function in momentum out in terms of spherical harmonics, as we did in equation (4.14), to remove the vector dependence. They are then all removed to leave

$$S(k', k) = \frac{\delta^{(1)}(k' - k)}{k^2} - 2\pi i \delta(E_{k'} - E_k) t(k', k; E) \tag{4.25}$$

The first term on the right can be rewritten as a delta function in energy multiplied by $\hbar^2/mk$, and as our s-matrix is only defined on the energy shell, when $k'^2 = k^2 = \varkappa^2$, we can write $S(k', k) = \delta(E_{k'} - E_k) S(\varkappa)$. This leaves us with

$$S(\varkappa) = \frac{\hbar^2}{m\varkappa} - 2\pi i t(\varkappa) t(E_\varkappa) \tag{4.26}$$

We can rescale to get an s-matrix dependant on the angular momentum quantum number only; $S_l = S(\varkappa) m\varkappa/\hbar^2$. This gives

$$S_l = 1 - \frac{2\pi i m\varkappa}{\hbar^2} t(\varkappa) t(E_\varkappa) \tag{4.27}$$

In the previous section, $t(\varkappa)$ was found from the condition necessary to form an algebraic equation for the t-matrix. For the momentum value $\varkappa$, this is simply given by the square of the Spherical Bessel Function $j_l(\varkappa a)$. This gives the following scattering matrix;

$$S_l = \frac{\hbar^2 + 2ga^2 m\varkappa j_l(\varkappa a) n_l(\varkappa a) + 2iga^2 m\varkappa j_l^2(\varkappa a)}{\hbar^2 + 2ga^2 m\varkappa j_l(\varkappa a) n_l(\varkappa a) - 2iga^2 m\varkappa j_l^2(\varkappa a)} \tag{4.28}$$

It was mentioned previously that the s-matrix can be expressed in terms of the phase shifts. This arises from the need to conserve the number of particles involved in a scattering event. To achieve this the s-matrix must be hermitian and unitary, so can be written as

$$S_l^* S_l = 1 \rightarrow S_l = e^{2i\delta_l} \tag{4.29}$$

If we write $e^{2i\delta_l} = \frac{n}{d}$, we can find the tangent of the phase shifts using the simple relation

$$tan(\delta_l) = \frac{id - in}{d + n} \tag{4.30}$$

Giving the tangent of the phase shifts as

$$tan(\delta_l) = \frac{2gma^2 \varkappa j_l^2(\varkappa a)}{\hbar^2 + 2gma^2 \varkappa j_l(\varkappa a) n_l(\varkappa a)} \tag{4.31}$$

This is the same answer as was found by Gottfried in Ref. [68].

4.4 Results

The phase shifts given by this model are plotted in figures 4.5, 4.6(a) and 4.6(b) for the first three angular momentum quantum numbers. They are plotted in the rescaled dimensionless units mentioned in section 4.1.2, and show low energy behaviour.

As the potential strength $\tilde{g}$ is increased, the phase shift increases to form peaks. The peaks at lower energies form first, then as the potential is increased further, all the peaks take on a saw-tooth shape, starting at $(\widetilde{\xi}, \delta_l) = (0, \pi)$. This saw-tooth pattern can be seen in Figure 4.7. The width of the pattern (the distance between adjacent zeros) increases for successive peaks, and also for increasing l. The maximum peak value is always equal to π.

We compare the graphs for the three angular momenta. At low energies, the $l = 0$ phase shift gives the greater result, with the higher angular momentum phase shifts becoming greater as the energy is raised. For a fixed energy value and increasing the potential strength, the largest contribution first comes from the $l = 0$ phase shift, then the higher phase shifts as the potential is increased further. It was found that once the phase shift equation was rescaled, there was no dependence on the radius of the Delta shell.

Looking only at the zero energy behaviour, the $l = 0$ graph behaves differently from the higher angular momenta graphs. As $\tilde{g}$ is increased the peak creeps up very close to the

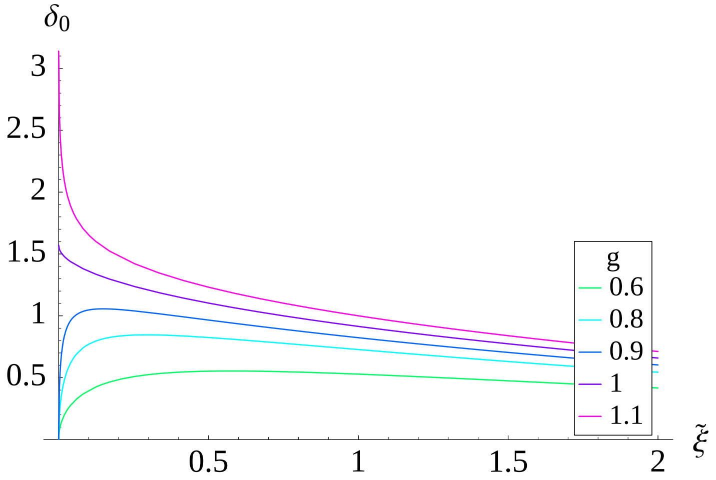

Figure 4.5: Non-relativistic phase shifts for $l = 0$ as the potential strength $\tilde{g}$ is increased. The phase shift at zero energy jumps abruptly from $\pi/2$ to π as $\tilde{g}$ passes 1.

phase shift axis, the line always starting at $(\widetilde{\xi}, \delta_0) = (0, 0)$ until it switches to being a slope of completely negative gradient at $(0, \pi/2)$ when $\tilde{g} = 1$. When $\tilde{g}$ is increased above 1, the curve jumps to start at $\delta_0 = \pi$, avoiding any values of δ_0 in between $\pi/2$ and π. Conversely, in the graphs of higher angular momenta, the peak continues to rise (two-sided) until a potential of $\tilde{g} = 2l + 1$ is reached when it turns into a one-sided slope starting at $(0, \pi)$.

In order to examine resonances in the scattering behaviour from the Delta Shell potential, a horizontal line is drawn through $\delta_l = \pi/2$ in Figure 4.7 for the $l = 0$ phase shifts. This line intersects the saw-tooth pattern twice in each peak, each intersection representing a type of resonance. The first intersection cuts through an almost instantaneous jump of π in the phase shift, and following Gottfried we call this rise passing through $\pi/2$ a sharp resonance. The second $\pi/2$ intersection on each saw-tooth is called the broad resonance.

At zero energy, there are obviously resonance differences between the $l = 0$ and the higher momentum graphs. A resonance is defined as a positive rise in the phase shift through an odd multiple of $\pi/2$. This does not occur at low energies in the s-wave scattering profile, therefore we can say that no resonances occur in the s-wave phase shifts at zero energy. The phase shift jumps immediately from a value of $\pi/2$ when $\tilde{g} = 2l+1$ to a phase shift of π, with no positive rise *through* $\pi/2$. Following Ref. [78], in which resonances in spherical

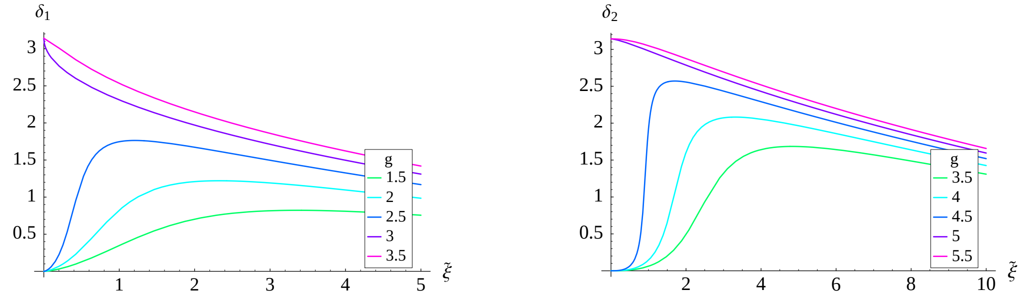

(a) Non-relativistic phase shifts for $l = 1$ as the potential strength is increased. The phase shift jumps to π when $\tilde{g}$ reaches 3.

(b) Phase shifts for $l = 2$. Potential strength, $\tilde{g}$ is increased and the graph displays similar behaviour to the $l = 1$ case, but the phase shift jumps when $\tilde{g} = 5$.

Figure 4.6: Non-relativistic phase shifts for $l = 1$ and $l = 2$.

wells are studied, we call the state when $\delta_l = \pi/2$, a 'half bound state'. The authors of Ref. [78] find, as we do, that it is only the s-wave phase shifts that have these states. The higher angular momentum phase shifts *do* rise through $\pi/2$ at low energies and therefore have resonances.

Figure 4.8 shows the location in energy of these resonances (the intersections with $\pi/2$) as they occur with changing potential value. The $l = 0$ curve increases immediately in $\tilde{g}$ as the energy is increased in Figure 4.8. This verifies that no resonance, broad or sharp, for any energy value can appear for $\tilde{g} \leq 1$. The parabolic nature of the $l = 1, 2$ curves highlight different behaviour. The minimum point on the curves is not at zero energy as it was for $l = 0$. The curve to the left of the minimum shows the development of the sharp resonance, which *can* occur for potentials less than the value given by $\tilde{g} = 2l + 1$. The curve to the right of the minimum shows the range of the broad resonances.

We can see from Figure 4.7 however, that at higher energies, the s-wave phase shifts *do* rise through $\pi/2$, therefore qualify as having resonance behaviour. If we were to plot the second set of resonances (from the second peaks), we would expect the $l = 0$ curves to take the same form as the other angular momentum curves, being parabolic with increasing energy.

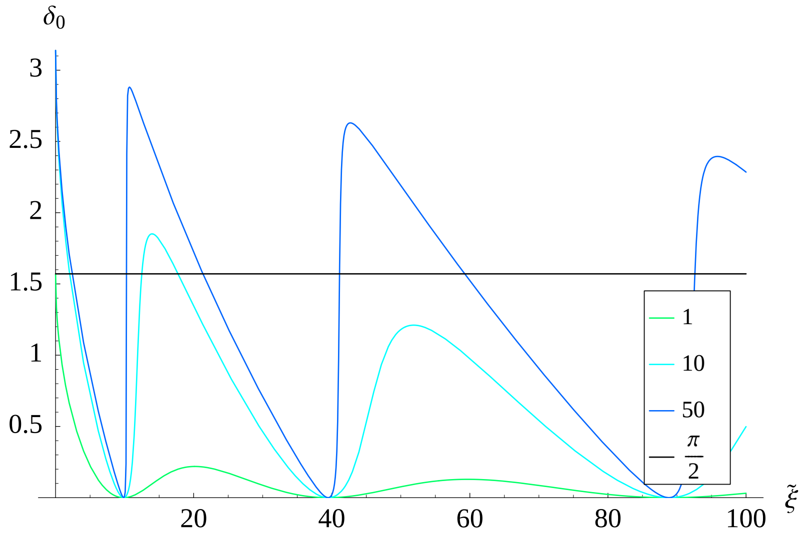

Figure 4.7: Non-relativistic phase shifts for $l = 0$ cutting through the $\pi/2$ line for potential values of 1, 10 and 50. The sharp resonances do not change location in energy as g is varied, a fact borne out by studying the phase shift analytically.

4.5 Discussion

The sharp resonances are the true resonances here. The occurrence of a resonance is always accompanied by a fast increase in the phase shift through the point $\pi/2$. They are usually characterised by an elongated s-shape curve which can be seen in Figure 4.6. As the interaction strength $\tilde{g}$ is increased, the phase shifts sharpen. As the phase shift gradient is an indication of the time for which the electrons are ‘bound’ by the potentials [71], this corresponds to the incoming electrons being bound for increasingly longer times. In fact, when the phase shift jump becomes instantaneous, the electron will become bound indefinitely and we see the occurrence of a bound state rather than a resonance state.

We saw the potentials required to form a bound state in Figure 4.2 in section 4.2. The vertical changes in phase shift by π also show these states. At zero energy, a scattering state changes into a bound state at the potential given by $\tilde{g} = 2l+1$ for $l > 0$, and at $\tilde{g} > 1$ for $l = 0$. Levinson’s theorem (see for example Refs. [68, 79]), states that for a spherically symmetric potential, the phase shift at zero momentum is related to the number of bound

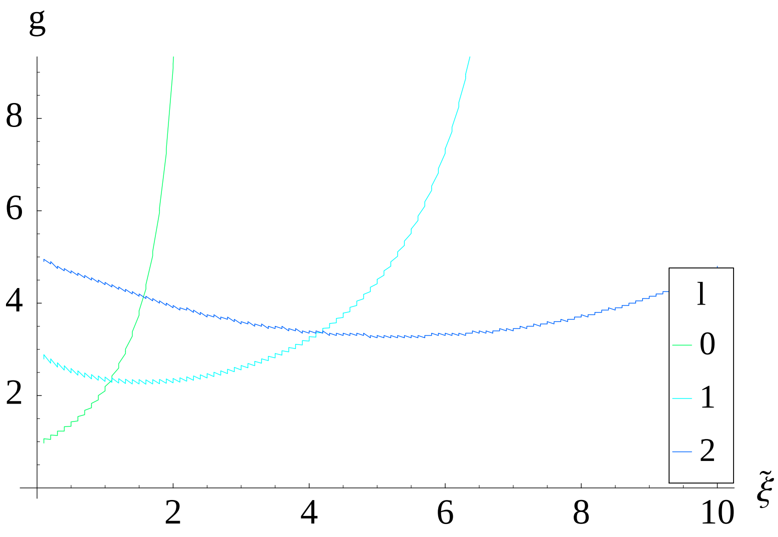

Figure 4.8: The occurrence of resonances in energy as a function of interaction strength, $\tilde{g}$. The $l = 1, 2$ cases show both broad and sharp resonances for one value of $\tilde{g}$, which doesn't occur for the $l = 0$ case. A minimum $\tilde{g}$ value is needed before resonances at zero energy can occur.

states in that angular momentum channel (n_l) by the relations

$$\begin{aligned} \delta_l(0) = & \quad (n_l + 1/2)\pi \quad & l = 0 \\ \delta_l(0) = & \quad n_l\pi \quad & l > 0 \end{aligned} \tag{4.32}$$

Our model then gives 1 bound state in the higher angular momentum channels, and none in the $l = 0$ channel.

It is difficult to tell from inspection what the minimum potential strength needed is to form the second set of resonances, or at what potential strength another bound state is formed from these resonances. Figure 4.7 shows a jump of π for when $\tilde{g} = 50$, but because these and the higher resonances form gradually, there is no obvious value defining the jump or where the resonances appear, as there was at zero energy.

Analytically however, both the energy at which the bound states occur, and the energies of the resonances (where the phase is equal to $\pi/2$), can be derived. We take the $l = 0$ case as an example. The phase shift is given by the following expression [with the rescaled notation (˜) dropped]

$$\tan(\delta_0) = \frac{g\sin(\sqrt{\xi})^2}{\sqrt{\xi} - g\cos(\sqrt{\xi})\sin(\sqrt{\xi})} \ . \tag{4.33}$$

A bound state is accompanied by a phase shift of π in this model, so the location of the phase shifts will be given when the right hand side of the equation evaluates to 0 (when $\delta_l = \pi$, $\tan\delta_l = 0$). This can be achieved by simply calculating the appropriate values of energy that puts the numerator to 0. As $\tilde{g}$ is simply multiplied, this implies that the location of the zeros are *not* dependent on the potential value. This is as we found in the figures. The first two bound states occur at $\tilde{\xi} = \pi^2$ and $4\pi^2$, according to the expression above, which can be verified by inspection of Figure 4.7. Applying the same criteria to the general phase shift equation, we find that the nth resonance for the lth angular momentum can be roughly given by the relation $\widetilde{\xi_l^n} \approx (n^2 + ln)\pi^2$, and can be exactly found at the roots of

$$j_l^2\left(\sqrt{\xi}\right) = 0 \ . \tag{4.34}$$

In Ref. [68], Gottfried studies the energies of the resonances, and for the $l = 0$ phase shifts he found the nth resonance to be situated at $\xi^n \approx n\pi^2\left(1 + 1/g\right)$. This was found by considering the scattering cross section of the $l = 0$ wave, $\sin^2\delta_0(\xi)$. We take the general phase shift equation and force it to evaluate to ∞ (when $\delta_l = \pi/2$, $\tan\delta_l = \infty$). This is achieved by putting the denominator equal to 0, which results in the resonances occurring at the energies given by

$$j_l\left(\sqrt{\xi}\right) n_l\left(\sqrt{\xi}\right) = -\frac{1}{g\sqrt{\xi}} \ . \tag{4.35}$$

This equation gives both the locations of the broad and the sharp resonances, so it is important to only take every other solution, starting with the second solution as $\tilde{\xi}$ is increased.

There is no upper limit on the gradient of the phase shift with energy, but a lower limit does exist. This is given in Wigner's paper [71] as

$$\frac{d\delta_l}{dk} > -a \tag{4.36}$$

a is the radius of the scattering centre, and dropped out of the model when we moved to dimensionless units. When we transform this relation to find the dependence on ξ rather than k, the fraction $d\delta_l/d\xi$ becomes inversely proportional to the velocity of the incoming electron wave. If we assume the velocity stays the same when crossing the potential, we get the relation

$$t < -\hbar\frac{d\delta_l}{d\xi} \tag{4.37}$$

This inequality gives a limit to the size of the negative-going gradient in the graphs of the phase shifts. Physically, t represents the time it takes the electrons with energy ξ to cross the area of the potential, assuming no interactions take place to slow them down. So the gradient must therefore be greater than this transit time, effectively disallowing the resonance state to exist for shorter than the length of time needed to cross the potential. This minimum time is increased when the potential range is increased, and is decreased when the electron has a higher energy (implying a greater velocity). Two observations we have made from this model are that the minimum time for the gradient decreases with increased angular momentum number; and as the energy is increased, the time decreases in discrete steps. This is due to the sudden jumps in the phase shifts being interspersed with lines of continuous gradient. For energies up to 50 dimensionless units, and for a potential range a, of a few Bohr radii, the transit times in this model are on the order of 10^{-17} s.

Table 4.1 gives some typical potential strengths and energy values of resonances for a few different radius values. The potential strengths g_B, are the values required to obtain the zero energy bound state for each angular momentum, and come from the dimensionless condition $\tilde{g} = 2l + 1$. The next two columns for each angular momentum give an example value of a potential required to have a resonance at $\tilde{\xi} > 0$, and the energy that this resonance will occur at. The subscript to each value of g is the dimensionless value of $\tilde{g}$ that the potential strength refers to. These are different for each angular momentum to try to reflect the same condition; namely a potential that only just causes resonances at energies greater than zero. The values in the table are found from the dimensionless graphs using $g[eVm] = \tilde{g}/2a \times 27.21 \times 0.529 \times 10^{-10}$ and $\xi[eV] = \tilde{\xi}/2a^2 \times 27.21$. All lengths are imputed as Bohrs, and are chosen to reflect the size of the tip atom which we take to be $\sim 2 - 4$ Åwide.

a /Bohr(Å)	$l = 0$			$l = 1$			$l = 2$		
	g_B /eV Å	g_9 /eV Å	E /eV	g_B	g_{12}	E	g_B	g_{14}	E
1 (0.529)	7.2	64.8	176.9	21.6	86.4	336.7	36.0	100.7	539.8
2 (1.058)	3.6	32.4	44.25	10.8	43.2	84.2	18.0	50.4	135.0
5 (2.645)	1.4	12.9	7.1	4.3	17.3	13.5	7.2	20.2	21.6

Table 4.1: Experimental values of resonances resulting from scattering from a Delta Shell potential of varying radii. The interaction strength g_B is the minimum value needed to create a zero energy bound state. The interaction strength g_v represents a potential v, required to just cause a resonance at higher energies, which are given in the third columns. Each successive set of results have the same units as the set for $l = 0$.

It appears that a larger radius of the Delta Shell results in resonant states existing for smaller values of interaction strength and electron energy. Table 4.1 and Figure 4.7 also show that higher values of both parameters are needed to create resonant states of a higher angular momentum. In the experiments, the tip bias was in the range of $0.5 - 8$ eV. Assuming that the applied bias is equal to the energy of the electrons, this energy is large enough to only create an s-wave bound state in our model.

4.6 Conclusions

We have introduced a Delta Shell potential as a model for an STM tip. The bound states of this potential were shown by Villarroel in Ref. [75], and a minimum value of the potential equal to $2l + 1$, where l is the orbital angular momentum, was found to be required for a bound state. The scattering states were formulated in momentum space using the t-matrix from the Lippmann-Schwinger equation. The energy-dependent part of the t-matrix was found using an integral result from J. Dörr in Ref. [76], and then manipulated to give the phase shifts using the unitarity condition of the scattering matrix.

The phase shifts showed that electrons could form resonance states at potentials less than $2l + 1$, when $l > 0$, and that this potential strength was the value at which a scattering state became a bound state. Resonance states were forbidden for s-wave electrons, and an increasing potential only served to change a half bound state to a bound state when $\tilde{g} > 1$.

At higher energies however, resonance states occurred for all angular momenta examined, and were found to occur at energies given by the second solutions to $j_l\left(\sqrt{\xi}\right) n_l\left(\sqrt{\xi}\right) = -1/g\sqrt{\xi}$. The bound states at $\tilde{\xi} > 0$ occurred at energies given by the solutions to $j_l^2\left(\sqrt{\xi}\right) = 0$, which were independent of the potential.

The negative gradient of the phase shift plots gives the least time the electrons can be partially bound by a potential to be on the order of $\sim 10^{-17}$ s, governed by the minimum time it takes to cross the potential shell.

The Delta Shell potential was found to accurately reproduce the scattering and bound states achieved from a spherical well potential in Ref. [78], although the critical potentials values differed. The same phase shift was achieved by Gottfried in Ref. [68], although the two approaches differed. Gottfried matched the wavefunctions approaching the potential to the wavefunctions inside the shell at the boundary of the shell. This approach treated the electrons in momentum space, removing the need to match wavefunctions.

Chapter 5

The Relativistic Delta Shell Model

In this chapter the Delta Shell Model is formulated in a relativistic framework. This allows the inclusion of the spins of the tunnelling electrons. We first discuss the way the Delta Shell potential has been used relativistically previously in the literature, then discuss the bound states found from the approach used by Villarroel [75]. We start from this to formulate the relativistic approach, introducing some theoretical concepts before calculating the phase shifts of the model. We then consider the low-energy, semi-relativistic limit, which we take in order to move back to non-relativistic energies whilst retaining the spin characteristics of the electrons.

5.1 The Relativistic Delta Potential

The treatment of the Delta Shell potential in relativistic quantum mechanics is problematic. Whilst the Schrödinger approach caused singularities in the derivative of the wavefunction, the relativistic approach with this potential presents singularities in the wavefunction itself. The centre of the delta potential is not well defined in this form, so the question of how this singularity should be treated must be asked.

Two approaches have been used in the literature: Either the potential is regarded as the limit of a sharply peaked potential around the location of the eventual Delta potential [80, 81], or the Dirac equation is solved with the Delta potential inserted explicitly [75, 82, 74]. The differences between both approaches in configuration space has been studied by McKellar *et al.* [83], in which the authors decide that the second approach introduces unphysical singularities. They argue that it is only for a weak value of the delta potential that the two methods agree.

A method which employs the second approach but appears to neatly avoid the problem of defining the wavefunction at the singularity is used in [84, 85]. As with any potential in the Dirac equation, the radial components, $F(r)$ and $G(r)$ form two coupled differential equations. Benguria *et al.* [84] treat the singularity problem in configuration space by manipulating the coupled equations to eliminate the occurrence of the potential. They integrate the resulting expression just over the singularity (from $a-\epsilon$ to $a+\epsilon$) and take the limit of the integration (ϵ) to zero;

$$F(a+\epsilon)^2 + G(a+\epsilon)^2 = F(a-\epsilon)^2 + G(a-\epsilon)^2 \tag{5.1}$$

The absolute value of this is constant when crossing the singularity. Another manipulation of the coupled equations can be combined with the above to get an expression relating the coupling constant g to the wavenumber k;

$$\tan g/\hbar c = \frac{\rho^2(1+\epsilon)\sqrt{1-\epsilon^2}(1+\Lambda\rho\sqrt{1-\epsilon^2})}{\rho^2(1+\epsilon)^2 - (\rho\sqrt{1-\epsilon^2}+1)(\rho\sqrt{1-\epsilon^2})(1-\Lambda)}\ , \tag{5.2}$$

Where $\rho = a/\hbar/mc$ and $\Lambda = \tanh ka/ka$. They study whether, for a fixed value of the Delta Shell radius a, a ground state exists in the limit of $-mc^2 < E < mc^2$. As the electron energy tends toward a free state ($E \rightarrow mc^2$), the coupling constant $g/\hbar c$ goes to zero and they find that bound states disappear for a vanishing potential. As the energy approaches the Dirac Sea, ($E \rightarrow -mc^2$), a critical value of the coupling constant arises for which the ground state energy sinks into the Dirac Sea. This is given by $\tan(g_{crit}/\hbar c) = -3/2\rho$. The same boundary condition for crossing the singularity is found in [85], where the relativistic case is studied in $(2+1)$ configuration space. The authors declare that the physically admissible solutions are finite, continuous, vanishing at the origin, and square integrable. Bound states must also satisfy the criteria that as $r \rightarrow \infty$, $F(r), G(r) \rightarrow 0$.

In [86] one of the authors from [84] goes on to use the boundary conditions there to examine the phase shifts caused by the scattering of relativistic particles near the low-energy limit. They use a Relativistic Partial Wave Expansion method, getting a differential cross section composed of the scattering amplitudes from the asymptotic form of the wavefunction.

Their phase shifts comprise of a simple fraction of sums of the First and Second Bessel Functions and display similar behaviour to the results presented later in this chapter.

A more formal construction of the Dirac operators consistent with a spherically symmetric potential is to be found in [82] and [74]. The authors construct self-adjoint extensions of the Dirac operator, and only consider those extensions that are rotationally invariant and reflection-symmetric. The boundary conditions require that the Delta Shell interaction can be written as

$$\int_{a-\epsilon}^{a+\epsilon} \delta(r-a)\Psi(r)\,dr = 1/2\left[\Psi(a^+)+\Psi(a^-)\right] \ . \tag{5.3}$$

In [87] and [80], Dominguez regards first the one-dimensional delta function, then the delta shell as the limit of an electrostatic-like sharply peaked potential with physically realistic boundary conditions given by

$$\begin{pmatrix} F(a+\epsilon) \\ G(a+\epsilon) \end{pmatrix} = \cosh(s) \begin{pmatrix} 1 & -\tanh(s) \\ \tanh(s) & 1 \end{pmatrix} \begin{pmatrix} F(a-\epsilon) \\ G(a-\epsilon) \end{pmatrix} \tag{5.4}$$

for a purely scalar potential s. In [83], McKellar *et al.* support this approach, commenting that the boundary conditions of the previous approach depends upon a formal manipulation of the Delta function potential that requires an ambiguous definition of the product of the width and the height of the Delta function. In the appendix of [74], Dittrich *et al.* try to reconcile the two approaches showing how their vector and scalar potentials match the potentials used in [80]. For the case of a scalar potential only, Dittrich's g_s can be written in terms of Dominguez's s as $g_s = 2\sinh s/1+\cosh s$. There is equivalence up to the set $g_s \in (-2,2)$ which is covered by $s \in (-\infty,\infty)$. However a scalar potential of g_s outside this range isn't covered by Dominguez's approach, which validates the statement in [83] that the two approaches are only equivalent for low potential values.

The only work on momentum space in the literature so far for this potential seems to be from Villarroel [75]. The author uses the method of directly solving the Dirac equation for the Delta shell potential, again integrating over the location of the singularity. Dominguez pointed out in [87] that this approach was different to his, but as this is the only work that operates in momentum space, the differences between the two approaches have not been fully examined.

5.2 Bound States in a Relativistic Model

We present the results of the relativistic bound state spectra from Villarroel's paper [75]. There are two graphs; one for $j = l + 1/2$, a positive coupling of the orbital and intrinsic angular momentum, and one for $j = l - 1/2$. These are given by

$$\begin{aligned} \frac{4c}{\tilde{g}} + \frac{\tilde{g}}{16c} &= \frac{(\widetilde{W} + \widetilde{\mu c^2})}{4c} I_{l+\frac{1}{2}}(\lambda) K_{l+\frac{1}{2}}(\lambda) + \frac{(\widetilde{W} - \widetilde{\mu c^2})}{4c} I_{l+\frac{3}{2}}(\lambda) K_{l+\frac{3}{2}}(\lambda) \\ \frac{4c}{\tilde{g}} + \frac{\tilde{g}}{16c} &= \frac{(\widetilde{W} + \widetilde{\mu c^2})}{4c} I_{l+\frac{1}{2}}(\lambda) K_{l+\frac{1}{2}}(\lambda) + \frac{(\widetilde{W} - \widetilde{\mu c^2})}{4c} I_{l-\frac{1}{2}}(\lambda) K_{l-\frac{1}{2}}(\lambda) \end{aligned} \tag{5.5}$$

where

$$\lambda = \sqrt{(\widetilde{\mu c^2})^2 - \widetilde{W}^2}\ , \tag{5.6}$$

and $I(\lambda)$, $K(\lambda)$ are the Modified First and Third Order Bessel Functions respectively. The relativistic energy $\widetilde{W}$ is related to the non-relativistic energy and the rest-mass energy through the relation $\widetilde{W} = \tilde{\xi} + \widetilde{\mu c^2}$. When comparing the two scenarios or when looking at graphs in this work, the relativistic energy is always converted into the non-relativistic energy form first.

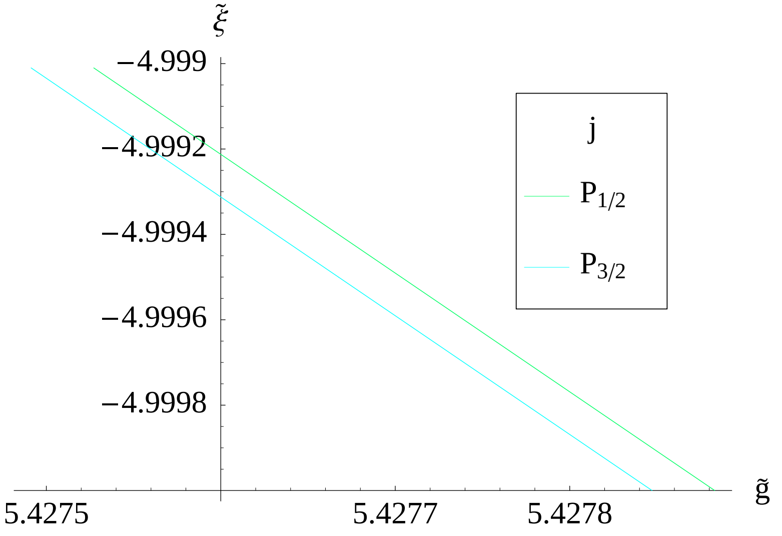

Figure 5.1: The two relativistic p-wave bound state spectra. The states for $j = l + 1/2$ and $j = l - 1/2$ differ causing a split of the order of ~ 0.0001.

The difference in the two spectra lies in the order of the Bessel Functions in the last term. The full spectra are plotted for p-shell bound states in Figure 5.1. There is an energy splitting of ~ 0.0001 between the two spectra, which is slightly increased to ~ 0.00015 in the case of the d-shell bound states (not shown).

To make the bound state spectra for the relativistic case match the non-relativistic, we had to input a value for the range of the Delta Shell - a. This parameter dropped out of the non-relativistic description naturally when the parameters were rescaled into dimensionless units. In the relativistic model however, the length remains as part of the rescaled mass term $\widetilde{\mu c^2}$. This can be written as $2a^2/\lambda_c^2$ where $\lambda_c = \hbar/mc$ is the Compton wavelength. This relation arises from the Heisenberg Uncertainty Principle and represents the minimum length in which a relativistic particle can be confined in and still be considered a free particle. Once a particle is confined to less than this length, particle/antiparticle pairs can be produced. Written in this form, the relativistic equation depends on the area covered by the Delta Shell potential in units of the Compton wavelength squared (the Compton area). In order to make the bound states match those from the non-relativistic model (such that $\tilde{g} = 2l + 1$), we had to put a equal to 2.

To verify that the splitting of the relativistic spectra is a relativistic spin-orbit effect we take the two relativistic curves and for a fixed value of $\tilde{g}$, we take the non-relativistic limit, taking $1/c^2 \to 0$. This is shown in Figure 5.2. It can clearly be seen that the two curves converge as we move toward the non-relativistic case, showing that this is indeed a relativistic phenomenon.

5.3 Relativistic Scattering with the Delta Shell Model

In this section we examine the scattering states arising from using a Delta Shell potential in a relativistic framework. We start by introducing the necessary relativistic notation, then discuss the t-matrix and phase shifts arising from the model. The results are described, and compared to the non-relativistic results.

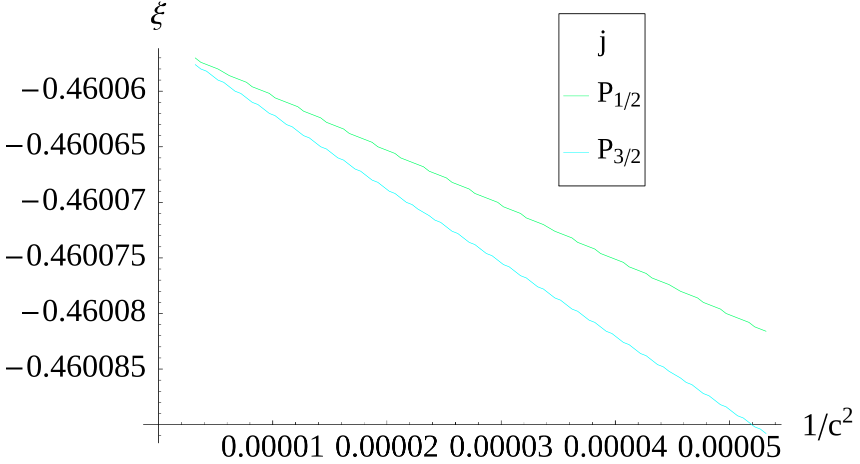

Figure 5.2: The non-relativistic limit is taken with the two relativistic spectra for the p-shell bound states. The convergence toward one curve when $c^2 \to 0$ shows that the splitting is due to relativistic effects.

5.3.1 Theoretical Background

Spin-angular functions

Spin-Angular Functions are the two dimensional, relativistic spinor equivalents of the Spherical Harmonics. They are given by

$$\langle \boldsymbol{k} \mid \chi^{\mu}_{\kappa} \rangle = \sum_{s} C(l\tfrac{1}{2}j; \mu - s, s) \langle \boldsymbol{k} \mid Y^{\mu - s}_{l} \rangle \chi_s \ . \tag{5.7}$$

They include a sum over Clebsch-Gordan coefficients, Spherical Harmonics, and the 2 × 1 spin vectors;

$$\mid \chi_{\uparrow} \rangle = \begin{pmatrix} 1 \\ 0 \end{pmatrix} \quad \mid \chi_{\downarrow} \rangle = \begin{pmatrix} 0 \\ 1 \end{pmatrix} \tag{5.8}$$

Whereas Spherical Harmonics are the angular solutions to the radial Schrödinger equation and are defined by the quantum numbers l and m, the orbital angular momentum value, and its z-component respectively, spin-angular functions are the angular solutions to the radial Pauli equation. They are defined by two new quantum numbers - κ and the z component of the total angular momentum μ. κ represents the *total* angular momentum number j which sums the orbital (l), and the intrinsic (S) angular momentum. For an electron, the angular momentum can be coupled either positively or negatively: $j = l+1/2$ or $j = l - 1/2$. The relations between κ, j, l, and $\bar{l}$, a quantity associated with negative values of κ, are summarised by Strange [67].

$$\begin{array}{lllll} j = l + 1/2 & ; & \kappa = -l + 1 = -(j + 1/2) & ; & \bar{l} = l + 1 = -\kappa \\ j = l - 1/2 & ; & \kappa = l = (j + 1/2) & ; & \bar{l} = l - 1 = \kappa - 1 \end{array} \tag{5.9}$$

Spin-angular Functions are related to Spherical Harmonics in the following way,

$$\underline{\boldsymbol{I}}_{\mathbf{2}} \sum_{l,m} Y_l^{m*}(\hat{\boldsymbol{r}}) Y_l^m(\hat{\boldsymbol{r}}') = \sum_{\kappa,\mu} \chi_\kappa^\mu(\hat{\boldsymbol{r}}) \chi_\kappa^{\mu\dagger}(\hat{\boldsymbol{r}}') \tag{5.10}$$

and obey the orthonormality condition;

$$\int \chi_{\kappa'}^{\mu'\dagger}(\hat{\boldsymbol{r}}) \chi_\kappa^\mu(\hat{\boldsymbol{r}}) d\hat{\boldsymbol{r}} = \delta_{\kappa\kappa'}\delta_{\mu\mu'} \tag{5.11}$$

Another useful number to define in relativistic quantum mechanics is $S_\kappa = \kappa / \mid \kappa \mid$, such that

$$\begin{array}{lll} S_\kappa = -1 & \text{for} & j = l + 1/2 \\ S_\kappa = +1 & \text{for} & j = l - 1/2 \end{array} \tag{5.12}$$

Table 5.1 summarises the values of the new quantum numbers κ and $\bar{l}$ for the three angular momentum values we present results for. Using κ rather than l removes the degeneracy caused by the spin-orbit coupling., such that there is a unique value of κ for each value of $j = l \pm 1/2$.

The Relativistic Green's Function

The relativistic Green's Function in configuration space is given by Strange as

$$G_0(\boldsymbol{r}, \boldsymbol{r}', W) = -\frac{1}{\hbar^2 c^2}(c\tilde{\boldsymbol{\alpha}} \cdot \hat{\boldsymbol{p}} + \tilde{\beta} mc^2 + W)\frac{e^{ipR/\hbar}}{4\pi R}\ . \tag{5.13}$$

l	$\bar{l}$	S	$j = l + S$	κ
0	1	+1/2	1/2	-1
1	0	-1/2	1/2	+1
1	2	+1/2	3/2	-2
2	1	-1/2	3/2	+2
2	3	+1/2	5/2	-3
3	2	-1/2	5/2	+3
3	4	+1/2	7/2	-4

Table 5.1: Values of κ and $\bar{l}$ for the first three angular momentum numbers.

W is the relativistic energy, and $\tilde{\alpha}_z$ and $\tilde{\beta}$ are the 4 by 4 matrices;

$$\tilde{\alpha}_i = \begin{pmatrix} 0 & \tilde{\sigma}_i \\ \tilde{\sigma}_i & 0 \end{pmatrix} \ ; \ \tilde{\beta} = \begin{pmatrix} \underline{\boldsymbol{I_2}} & 0 \\ 0 & -\underline{\boldsymbol{I_2}} \end{pmatrix} \tag{5.14}$$

The $\tilde{\sigma}_i$ terms are the 2 by 2 Pauli matrices, $\underline{\mathbf{I_2}}$ is the 2 by 2 identity matrix, and $R = |\boldsymbol{R}| = r, \boldsymbol{R} = \boldsymbol{r} - \boldsymbol{r'}$.

The Green's function in momentum space can be found by taking the Fourier Transform of this,

$$-\frac{1}{\hbar^2 c^2} \int d^3r \, (c\tilde{\boldsymbol{\alpha}} \cdot \hat{\mathbf{p}} + \tilde{\beta} mc^2 + W) \frac{e^{ipr/\hbar}}{4\pi r} e^{-i\boldsymbol{k}\cdot\boldsymbol{r}} \ . \tag{5.15}$$

The $\hat{\mathbf{p}}$ operation is carried out, assuming that we orientate our system such that the momentum is directed toward the z-axis only. Integration over ϕ gives a factor of 2π and integration over $\cos\theta$ leaves

$$\frac{-i}{2\hbar^2 c^2 k} (-\hbar c \tilde{\alpha}_z k + \tilde{\beta} mc^2 + W) \int_0^\infty dr \, e^{i(p/\hbar - k)r} - e^{i(p/\hbar + k)r} \ . \tag{5.16}$$

The integrand evaluates to

$$\frac{2ik}{p^2/\hbar^2 - k^2} \ , \tag{5.17}$$

giving the relativistic Green's function in momentum space as

$$G_0(k, W) = \frac{(-\hbar c \tilde{\alpha}_z k + \tilde{\beta} mc^2 + W)}{(pc)^2 - (\hbar ck)^2} \ . \tag{5.18}$$

This Green's Function has poles when the denominator is equal to zero. To avoid this problem, a small imaginary energy is added to the denominator, and the Green's Function is evaluated in the limit of this energy going to zero. We already mentioned in the non-relativistic section that the Retarded form of the Green's Function, G^R has a small positive energy added to the denominator. This represents the physical scenario in which events propagate forward in time, and the cause precedes the effect. The Advanced form of the Green's Function, G^A is for the opposite scenario. We will always be using the Retarded Green's Functions.

5.3.2 The Relativistic T-Matrix

The relativistic t-matrix should have a 4 x 4 structure to accommodate the possibility of spin-up and spin-down components for particles of both negative and positive mass. The t-matrix should have the same form as the potential, which can again be written as the Fourier Transform of the potential in coordinate space.

For a 4 x 1 Spinor, U_s, multiplied by an exponential, Strange gives the relativistic expansion as

$$U_s \exp\left(ipr/\hbar\right) = 4\pi \left(\frac{W+mc^2}{2W}\right)^{1/2} \sum_{\kappa\mu} C(l\tfrac{1}{2}j;\mu-s,s)\, i^l Y_l^{\mu-s*}(\hat{\boldsymbol{k}}) \times \begin{pmatrix} j_l(kr)\chi_\kappa^\mu(\hat{\boldsymbol{r}}) \\ \dfrac{i\hbar c k S_\kappa}{W+mc^2} j_{\bar{l}}(kr)\chi_{-\kappa}^\mu(\hat{\boldsymbol{r}}) \end{pmatrix} \tag{5.19}$$

We insert this and its complex conjugate into the Fourier Transform of the potential, simplifying the expression by calling $-2ga^2(W+mc^2/2W\pi) = V_W$ and $\hbar c k S_\kappa/(W+mc^2) = D$;

$$V(\boldsymbol{k'};\boldsymbol{k}) = V_W \sum_s \sum_{\kappa\mu} \sum_{\kappa'\mu'} \int d\Omega_r Y_{l'}^{*\mu'-s}(\hat{\boldsymbol{k}}')Y_l^{\mu-s}(\hat{\boldsymbol{k}})C(l\tfrac{1}{2}j;\mu-s,s)C(l'\tfrac{1}{2}j';\mu'-s,s) \times i^{l'-l} \begin{pmatrix} j_{l'}(k'a)\chi_{\kappa'}^{\mu'}(\hat{\boldsymbol{r}}) \\ iD' j_{\bar{l}'}(k'a)\chi_{-\kappa'}^{\mu'}(\hat{\boldsymbol{r}}) \end{pmatrix} \begin{pmatrix} j_l(ka)\chi_\kappa^{\dagger\mu}(\hat{\boldsymbol{r}}) & -iD j_{\bar{l}}(ka)\chi_{-\kappa}^{\dagger\mu}(\hat{\boldsymbol{r}}) \end{pmatrix} \tag{5.20}$$

The full t-matrix equation is as before, only this time the potential, t-matrix and Green's functions are all 4 × 4 matrices, and the full relativistic energy, W, is used:

$$t(\boldsymbol{k'},\boldsymbol{k};W) = V(\boldsymbol{k'},\boldsymbol{k}) + \int d^3k''\, V(\boldsymbol{k'},\boldsymbol{k''})G^R_{rel}(\boldsymbol{k''};W)t(\boldsymbol{k''},\mathbf{k};W) \tag{5.21}$$

We assume the t-matrix takes the same form as the potential, replacing the constant V_W with the energy term $t(W)$, yet to be determined. Putting the appropriate expressions into (5.21) and simplifying, we derive an expression for $t(W)$.

$$\begin{aligned} t(W) &= V_W \Bigg[1 - V_W \sum_{s\kappa\mu} \int d\Omega_r \int_0^\infty dk\, \frac{k^2 C(l\tfrac{1}{2}j;\mu-s,s)^2}{(pc)^2-(\hbar ck)^2+i\epsilon} \\ &\times \quad \begin{pmatrix} j_l(ka)\chi^{\dagger\mu}_\kappa(\hat{\boldsymbol{r}}) & -iDj_{\bar{l}}(ka)\chi^{\dagger\mu}_{-\kappa}(\hat{\boldsymbol{r}}) \end{pmatrix} \\ &\times \begin{pmatrix} W+mc^2 & 0 & -\hbar ck & 0 \\ 0 & W+mc^2 & 0 & \hbar ck \\ -\hbar ck & 0 & W-mc^2 & 0 \\ 0 & \hbar ck & 0 & W_mc^2 \end{pmatrix} \begin{pmatrix} j_l(ka)\chi^\mu_\kappa(\hat{\mathbf{r}}) \\ iDj_{\bar{l}}(ka)\chi^\mu_{-\kappa}(\hat{\mathbf{r}}) \end{pmatrix} \Bigg]^{-1} \end{aligned} \tag{5.22}$$

Multiplying out the matrix and vectors, and writing the Spin Angular functions out in full, the integral over the r angles is carried out. This results in delta functions in $l,\bar{l}$ and l,l. Obviously each value of l has a unique, different value of $\bar{l}$ associated with it so the terms featuring the delta functions in l and $\bar{l}$ disappear and we are left with only the 'diagonal' components (δ_{ll}) from the matrix multiplication.

$$t(W) = V_W \left[1 - V_W \int_0^\infty dk\, \frac{k^2 \left(j_l^2(ka)(W+mc^2) + D^2 j_{\bar{l}}^2(ka)(W-mc^2) \right)}{p^2c^2 - (\hbar ck)^2 + i\epsilon} \right]^{-1} \tag{5.23}$$

The integral is split into two terms. The first consists of $j_l^2(ka)k^2$ and is calculated the same way as the non-relativistic t-matrix integral. The second term is given by

$$\int_0^\infty \frac{(W-mc^2)D^2 j_{\bar{l}}^2(ka)k^2}{p^2c^2-(\hbar ck)^2+i\epsilon}\, dk \tag{5.24}$$

The integral is changed from an integral over dk to one over $d(ka)$, and split into Principal and remainder parts in the same manner as the previous term. As the constant D features k, the numerator has k^4 in it. Using the same method as was used to calculate

$$\int_0^\infty \frac{j_l^2(s)s^2}{s^2-t^2}\,ds = -\frac{\pi}{2} t j_l(t) n_l(t) \tag{5.25}$$

by Dörr [76], it is straight forward to show that

$$\int_0^\infty \frac{j_l^2(s)s^4}{s^2-t^2}\,ds = -\frac{\pi}{2} t^3 j_l(t) n_l(t) \tag{5.26}$$

Combining the results from both terms, we finally find $t(W)$ to be

$$t(W) = \frac{\dfrac{-2ga^2}{\pi}\dfrac{W+mc^2}{2W}}{1+\dfrac{ga^2}{2}\dfrac{(W+mc^2)^2}{W\hbar^2c^2}\dfrac{p}{\hbar}(j_l n_l - i j_l^2) + \dfrac{ga^2}{2}\dfrac{W-mc^2}{W(W+mc^2)}\dfrac{p^3}{\hbar^3}(j_{\bar{l}} n_{\bar{l}} - i j_{\bar{l}}^2)} \tag{5.27}$$

The argument of all of the Bessel Functions is $(pa/\hbar)$.

The scattering matrix element is found as usual by $S = 1 - iCt(W)t(pa/\hbar)$. $Ct(pa/\hbar)$ was given by $2\pi m\kappa j_l^2(\kappa a)/\hbar^2$ for the non-relativistic case, and was found from the terms necessary to make an algebraic equation out of the t-matrix.

For the relativistic case, from the form of the potential it would appear that an appropriate expression for $t(pa/\hbar)$ would be

$$\begin{pmatrix} \sum_s j_l^2(\frac{pa}{\hbar})C(l\frac{1}{2}j;\mu-s,s)^2 & 0 \\ 0 & \sum_s D^2 j_{\bar{l}}^2(\frac{pa}{\hbar})C(\bar{l}\frac{1}{2}j;\mu-s,s)^2 \end{pmatrix} \tag{5.28}$$

Where each entry can be expanded into a 2 x 2 matrix. We use the scattering matrix definition to find the constant C which gives the relativistic phase shifts

$$\tan\delta_\kappa = \frac{\dfrac{1}{\hbar^2c^2}\dfrac{ga^2}{2W(W+mc^2)}\dfrac{p}{\hbar}\left(j_l^2(W+mc^2)^3 + j_{\bar{l}}^2(W-mc^2)p^2c^2\right)}{1+\dfrac{1}{\hbar^2c^2}\dfrac{ga^2}{2W(W+mc^2)}\dfrac{p}{\hbar}\left(j_l n_l(W+mc^2)^3 + j_{\bar{l}} n_{\bar{l}}(W-mc^2)p^2c^2\right)}\,. \tag{5.29}$$

Each phase shift is now labeled with the appropriate value of κ rather than l.

5.4 Results

The curves described by the relativistic phase shifts have the same general shape as the non-relativistic curves. The curve for $l = 0$, shown in Figure 5.3 displays the same zero energy behaviour, and the points at which the curves touch the energy axis for all three angular momenta (the location of the bases of the sharp resonances) are also the same. The potentials at which the resonances start to appear are not affected by the move to relativistic scattering.

All three of the lowest angular momentum curves have been plotted in Figure 5.4 to show the overall similarity of the general features to the non-relativistic curves. The potential strength is chosen to be equal to 3, such that the $l = 0$ bound state is well-established, the $l = 1$ one has just formed, and the $l = 2$ profile shows resonance behaviour, and the profile is still double-sided.

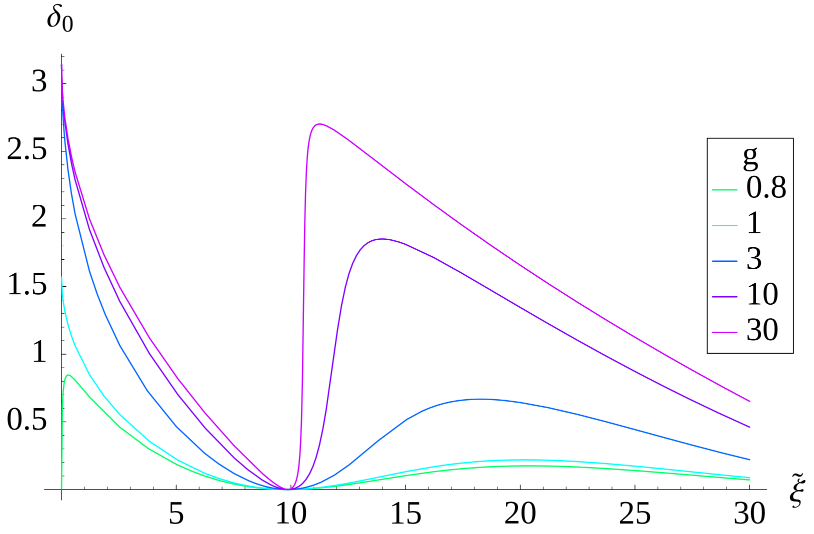

Figure 5.3: The relativistic phase shift curves for the $l = 0$ angular momentum as potential strength $\tilde{g}$ is increased.

Following Ref. [78], it was expected that an s-wave resonance would be discovered at low potentials and energies when we moved to a relativistic formulation. By inspecting the phase shifts at very low energies and at potentials just lower than that required for a bound state, we find this to be the case. However the values that were found for a resonance

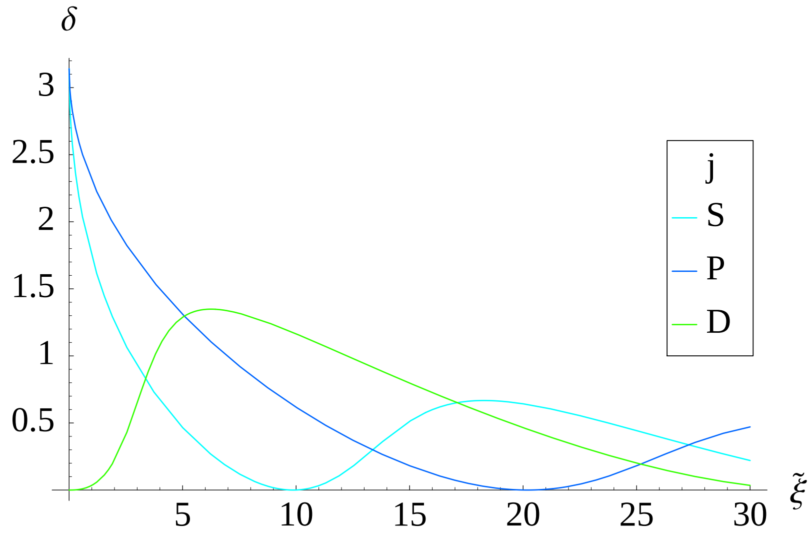

Figure 5.4: The first three angular momentum curves for the relativistic phase shifts under a Delta potential of strength $g = 3$. The shapes are similar to the non-relativistic curves.

were given by $\tilde{g} = 1 - 2 \times 10^{-16}$ and $\tilde{\xi} = 4 \times 10^{-20}$, making the resonance unobservable on the energy scales we are interested in.

The location of the resonances can again be calculated for a fixed potential value simply by putting the denominator of the phase shift equation equal to zero. This time, for relativistic scattering, the resonances occur at the solutions to the equation

$$\frac{\sqrt{\xi\ \lambda}}{\lambda(\xi + \mu c^2)}\ \left(\lambda\ \xi^2 j_{\bar{l}}\ n_{\bar{l}} + \lambda^3 j_l\ n_l\right) = -\frac{1}{g}\ , \tag{5.30}$$

where the arguments of the Bessel Functions are given by $\sqrt{\lambda\ \xi}/4c^2$, $\lambda = \xi + 2\mu c^2$, and all the parameters are understood to be dimensionless (usually presented with a tilde).

The reason for moving to relativistic scattering was to include the spin-orbit behaviour in the phase shifts for the $l = 1$ and $l = 2$ momentum values. We concentrate on a p-shell electron; namely we are interested in the quantum numbers $\kappa = +1, -2$. Figure 5.5 shows the phase shift for the $l = 1$ state for a potential strength of $\tilde{g} = 5$. Figure 5.5(b) shows an area of the main phase shift in greater detail as the splitting due to the spin isn't visible on the energy scale of the resonances. The phase shifts are split by $\sim 2 \times 10^{-7}$ energy units, which is a lot smaller than the splitting in the p-shell bound states, (of the order of

10^{-4}).

However, the energy difference between the two split states depends upon the part of the phase shift being studied. Comparison with Figure 5.5(a) shows that the detailed graph was looking midway between the top and bottom of a slope defining the start and end of a resonance. To see splitting in the scattering states of a comparable size to the bound state splitting, we should instead look at the points where the phase shift first turns upwards to form a resonance, or at the top of a resonance slope, when the phase shift turns downwards. Figure 5.6(a) shows the point where the resonance slope finishes, and it quite clearly shows a maximum splitting in the phase shifts. It can be seen in Figure 5.6(b) that this is due to one of the spin-split phase shifts changing sign before the other. This cross-over of the curves causes the wide difference in the energy.

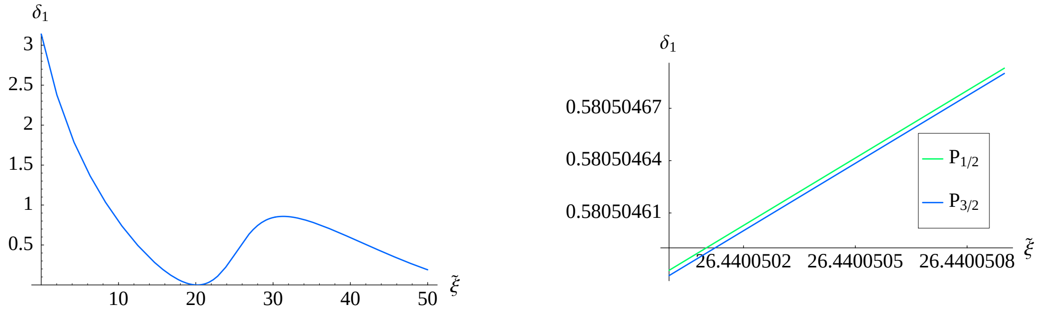

(a) The $l = 1$ phase shift for a potential strength of $\tilde{g} = 5$.

(b) A section of the Figure 5.5(a) in greater detail, showing the spin-split phase shifts.

Figure 5.5: The splitting of the phase shifts due to spin-orbit coupling. The width of the split is $\sim 2 \times 10^{-7}$ energy units at this point.

As the potential is increased, the splitting actually decreases. This is due to the resonances sharpening, which means that the top and bottom of the resonance lines move closer together in energy. This in turn means that the phase shift graphs turn more sharply, reducing the energy differences at the crossover points. As there are spin-splitting maxima at the top and bottom of the resonance lines, this also has the effect of moving the maxima closer together in energy. When the potential is strong enough to turn the resonance into a bound state, there will be no spin-splitting seen in the phase shifts.

Because the bound state and scattering state graphs were rescaled to dimensionless energy units, we can easily compare them to the energy spectrum of the Hydrogen atom. When

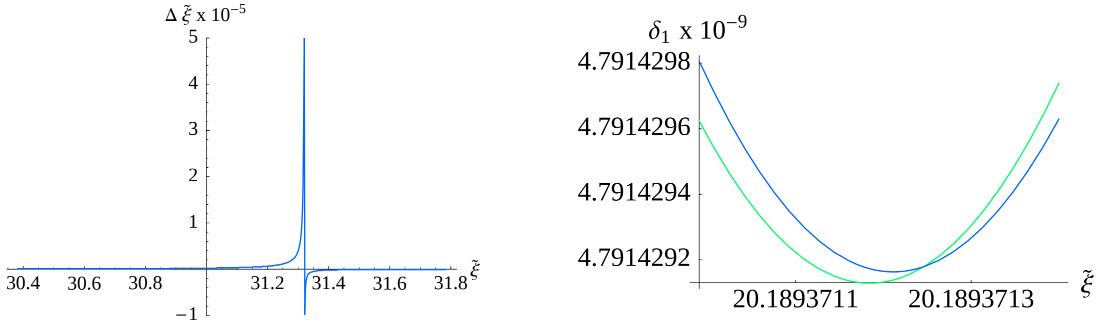

(a) The energy difference between the two spin-split levels in the $l = 1$ case, plotted as a function of energy for a potential strength of $\tilde{g} = 5$.

(b) The beginning of a resonance curve for the $P_{1/2}$ (green) and $P_{3/2}$ (blue) phase shifts. The energy splitting is greatest shortly before the curves cross over.

Figure 5.6: The energy difference between the spin-split $l = 1$ phase shifts.

the bound states were first plotted, the radius of the delta shell was chosen in the relativistic model to be equal to 2. This ensured that the position of the relativistic bound states matched those of the non-relativistic. This turns out to conveniently put the difference in energy between the s- and p-shell levels to be ~ 10, (the difference in location of the resonances along the energy axis, seen for example in Figure 5.4). In electron-volts this matches the energy difference between both levels in the Hydrogen atom (see Figure (5.7)). In Figure 5.6(a) the maximum spin-split energy difference of $\sim 4 \times 10^{-5}$ between the $P_{1/2}$ and $P_{3/2}$ states corresponds nicely to the splitting observed in the Hydrogen atom of $4.5 \times 10^{-5}\, eV$.

5.5 The Semi-Relativistic Limit

In order to describe the experiment accurately we need to look at the scale of non-relativistic energies, but still retain the spin-orbit coupling achieved by using the relativistic representation. To this end we aim to take a semi-relativistic limit of the phase shifts, retaining terms up to the order of $1/c^2$. Rewriting the expression for the phase shifts such that $1/c^2 = X$, we find the Bessel Functions in equation (5.29) are multiplied by the following;

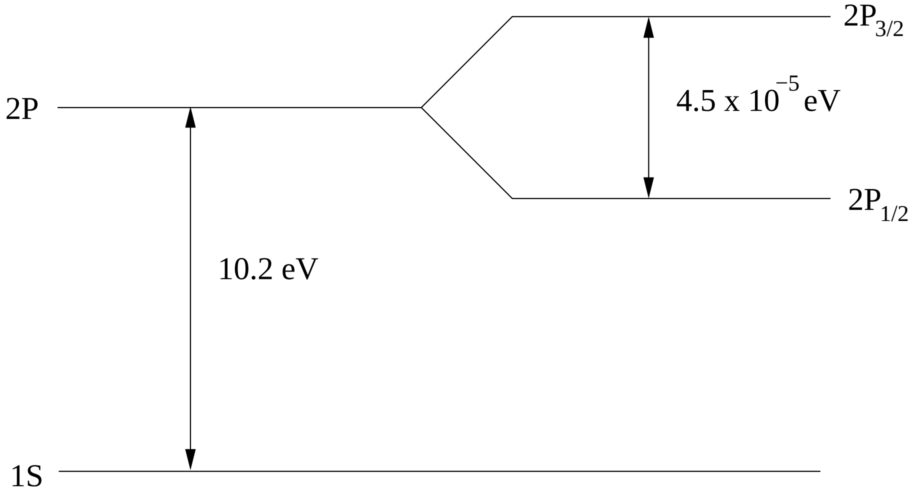

Figure 5.7: The energy levels in the Hydrogen spectrum that correspond to the scattering states observed with the Delta Shell potential. The difference between the S and P levels, and the $P_{1/2}$ and $P_{3/2}$ levels correspond to those achieved with the model.

$$j_l^2\left(\frac{pa}{\hbar}\right)\frac{4m^2+4EX}{2E^2mX+4Em^2} \quad ; \quad j_{\bar{l}}^2\left(\frac{pa}{\hbar}\right)\frac{EX^2}{2E^2X^2+6EmX+4m^2} \tag{5.31}$$

Taking $c \to \infty$ ($X \to 0$) and leaving terms of order X and lower will, however, remove the dependence on the Bessel Functions $j_{\bar{l}}$, and therefore all the spin-orbit coupling. It is only through the $\bar{l}$ term that the states of the same orbital momentum, but of different total angular momentum are described. To keep this term it is necessary to keep terms up to X^2 ($1/c^4$), and take the leading order terms. This then gives a semi-relativistic phase shift of

$$tan(\delta_l) = \frac{gka^2\left(j_l^2(ka)\dfrac{2m}{\hbar^2} + j_{\bar{l}}^2(ka)\dfrac{\hbar^2k^4}{8m^3c^4}\right)}{1+gka^2\left(j_l(ka)n_l(ka)\dfrac{2m}{\hbar^2} + j_{\bar{l}}(ka)n_{\bar{l}}(ka)\dfrac{\hbar^2k^4}{8m^3c^4}\right)} \tag{5.32}$$

This is the fully non-relativistic phase shift with $j_{\bar{l}}$ terms added to the usual j_l terms. Interestingly, when this is put into dimensionless units, these extra terms turn out to be multiplied by the prefactor $\xi^2/(2\widetilde{mc^2})^2$, where $\widetilde{mc^2}$ is the scaled rest mass energy mc^2 in dimensionless units.

$$tan(\delta_l) = \frac{\tilde{g}\sqrt{\xi}\left(j_l^2(\sqrt{\xi}) + \frac{\xi^2}{(2\widetilde{mc^2})^2} j_{\overline{l}}^2(\sqrt{\xi})\right)}{1 + \tilde{g}\sqrt{\xi}\left(j_l(\sqrt{\xi})n_l(\sqrt{\xi}) + \frac{\xi^2}{(2\widetilde{mc^2})^2} j_{\overline{l}}(\sqrt{\xi})n_{\overline{l}}(\sqrt{\xi})\right)} \tag{5.33}$$

We can relate this prefactor to the Compton Wavelength. We recall that when a relativistic particle is confined to a length less than $\hbar/mc^2$, there is a possibility that particle/antiparticle pairs can be created. The size of the spin-orbit coupling term in the semi-relativistic limit is determined by the ratio of the particles energy to the energy necessary to create two such particles.

In the low energy limit, the energy of the particle is much less than its rest mass, and the spin-orbit splitting of the spectra is not expected to be visible on the scale of the resonances. As the energy approaches the rest mass energy, equal weighting is given to both the l and the $\overline{l}$ terms in the phase shift, with the $\overline{l}$ term becoming more important as the energy is increased further.

One of the reasons to use the semi-relativistic limit is that we want a curve that is close in energy to the non-relativistic case. We find that the difference between the relativistic and the semi-relativistic curve is practically the same as the difference between the relativistic and non-relativistic, showing that the semi-relativistic is similar to the non-relativistic. The other, more important feature we want from the semi-relativistic limit is the retaining of the spin-split energy states. Plotting the spin-split differences given by the semi-relativistic limit shows the exact same curve as the relativistic, showing that this is indeed an accurate limit to consider.

The more general features of this limit are the same as the non-relativistic curves given in the previous chapter.

5.6 Conclusions

The Delta Shell potential was used in a relativistic scattering model to include the spin-orbit effect of the incoming electrons. By moving to a relativistic model, the nature of the s-wave phase shift profile changed such that a resonance at low energies now occurred at a potential just lower than that required for a half bound state. However the difference between the potential of the resonance and the potential of the bound state was so small as to be practically unobservable, as was the energy at which the resonance occurred; $\tilde{\xi} = 4 \times 10^{-20} \rightarrow \xi = 1.4 \times 10^{-19}$ eV. We therefore decide to treat this resonance of the s-wave state as being unattainable practically.

As the scattering occurs at low (non-relativistic) energies, a semi-relativistic limit was sought that retained the spin-orbit splitting of the scattering states. When put into dimensionless units, the semi-relativistic limit demonstrated the energy dependence of the phase shifts. The energy of resonances was given by the expression

$$-\frac{1}{\tilde{g}\sqrt{\xi}} = j_l(\sqrt{\xi})n_l(\sqrt{\xi}) + \frac{\xi^2}{\widetilde{(2mc^2)}^2} j_{\bar{l}}(\sqrt{\xi})n_{\bar{l}}(\sqrt{\xi}) \tag{5.34}$$

for a fixed potential value. The second term on the right is the semi-relativistic correction, and for energies less than the rest mass energy, is found to be negligible for the bulk behaviour. The size of the spin-orbit splitting however, is determined by this ratio of the electron energy to the energy required to create a particle/antiparticle pair. It was found that the maximum energy split between the two spin-split states decreased as the potential strength $\tilde{g}$ was increased, and the maximum splitting observed for the p-states with a potential strength of $\tilde{g} = 5$, $(1.8 \times 10^{-9}\, eVm)$, was calculated to be $1.4 \times 10^{-4}\, eV$. We also show that by choosing the Delta Shell radius to be equal to 2, we can correctly reproduce the energy level splitting scales seen in the Hydrogen energy spectrum.

Chapter 6

Spin Dependant Delta Shell Scattering

In the previous two chapters we have considered the bare Delta Shell, which we chose to represent the tip of the STM. Now we add a spin onto the shell to model the BDPA molecule. This spin represents the unpaired electron on the molecule, which the tunnelling electrons only interact with when they are on the potential shell. We start by showing how the transition matrix for a Delta Shell potential is changed by the addition of an external spin. We show in detail the non-relativistic approach, then move to the semi-relativistic limit which we will use to include the spin-orbit interaction of the tunnelling electrons.

6.1 The t-matrix for a Delta Shell potential with an external spin.

To include the presence of the electron on the molecule, the Delta Shell potential is modified by the addition of an interaction between the molecule electron spin and the spin of the tunnelling electrons, of strength $\boldsymbol{J}$.

$$V(\boldsymbol{r}) = -(g + J\boldsymbol{S}\cdot\boldsymbol{\sigma})\delta(|\mathbf{r}| - a) \tag{6.1}$$

$\boldsymbol{S}$ is the spin of the electron on the molecule, and $\boldsymbol{\sigma}$ is the vector spin operator of the tunnelling electrons. The spin of the free electron on the molecule (which is s-wave), is

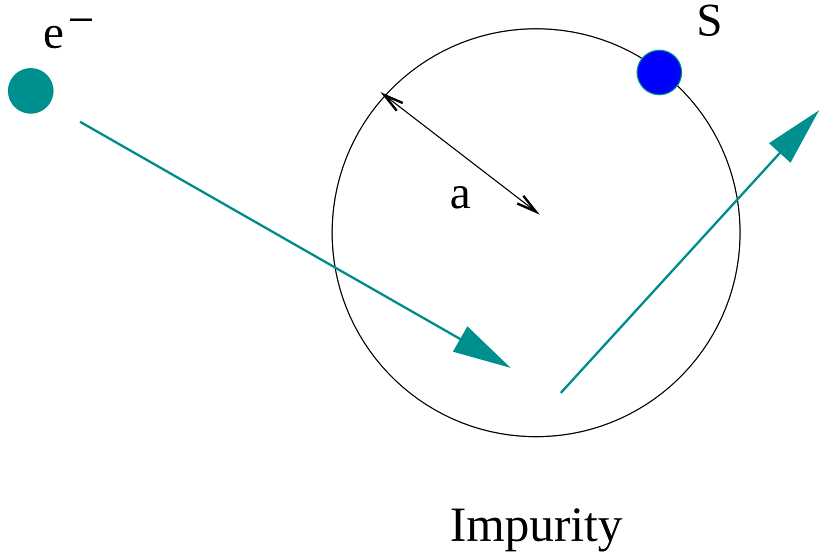

Figure 6.1: The BDPA molecule is represented by a Delta Shell potential. A spin sits on the shell representing the single unpaired electron magnetic moment.

treated as sitting on the delta shell.

The eigenvectors of the spin operators are given by, as usual,

$$\begin{aligned}\sigma^2 \mid \boldsymbol{k} s\, m_s\rangle &= s(s+1) \mid \boldsymbol{k} s\, m_s\rangle \\ \sigma_z \mid \boldsymbol{k} s\, m_s\rangle &= m_s \mid \boldsymbol{k} s\, m_s\rangle \\ S^2 \mid \boldsymbol{k} SM\rangle &= S(S+1) \mid \boldsymbol{k} SM\rangle \\ S_z \mid \boldsymbol{k} SM\rangle &= M \mid \boldsymbol{k} SM\rangle \ .\end{aligned}$$

We need to calculate the interaction

$$\langle \boldsymbol{k}' m_s' M' \mid V \mid \boldsymbol{k}\, m_s\, M\rangle \ , \tag{6.2}$$

where we have simplified the notation by only writing down the z-component of the spins. We change the representation from real space to momentum space as we did previously, assuming that the spin is not affected by this change

$$\begin{aligned}V_{\boldsymbol{k'}M'm_s';\boldsymbol{k}Mm_s} &= \langle \boldsymbol{k}' M' m_s' \mid V \mid \boldsymbol{k} M m_s\rangle \\ &= \frac{-1}{(2\pi)^3}\int \langle M' m_s' \mid (g + J\boldsymbol{S}\cdot\boldsymbol{\sigma})\delta(r-a) \mid M m_s\rangle \exp\left(i(\boldsymbol{k'}-\boldsymbol{k})\cdot\boldsymbol{r}\right) d^3r\end{aligned}$$

(6.3)

We expand the exponentials into Spherical Harmonics, simplify using the orthogonality of the Spherical Harmonics and perform the radial integral over the delta function:

$$V_{\boldsymbol{k'}M'm_s';\boldsymbol{k}Mm_s} = \frac{-2a^2}{\pi}\sum_L Y_L^*(\hat{\boldsymbol{k}})Y_L(\hat{\boldsymbol{k'}})j_l(k'a)j_l(ka)\langle M'm_s' \mid (g + J\boldsymbol{S}\cdot\boldsymbol{\sigma}) \mid Mm_s\rangle \ . \tag{6.4}$$

Again, L is used to represent the quantum numbers l, and m_l. Our t-matrix can be written as an operator on $(k, l, M, m_s; k', l', M', m_s')$, and is put into the same basis set as the potential to give

$$\langle \boldsymbol{k'}M'm_s' \mid t(E) \mid \boldsymbol{k}Mm_s\rangle = \sum_{L,L'} Y_{L'}(\hat{\boldsymbol{k'}})Y_L^*(\hat{\boldsymbol{k}})\langle k'\, l'\, M'\, m_s' \mid t(E) \mid k\, l\, M\, m_s\rangle \ . \tag{6.5}$$

We assume that the transition matrix is of a similar form to the potential, with a separable momentum and spin dependence. The momentum subspace will be the same as for the potential, consisting of two Spherical Bessel functions and a Kronecker delta function in angular momentum, and we won't specify the form of the spin subspace yet.

$$\langle \boldsymbol{k'}M'm_s' \mid t(E) \mid \boldsymbol{k}Mm_s\rangle = \sum_{L,L'} Y_{L'}(\hat{\boldsymbol{k'}})Y_L^*(\hat{\boldsymbol{k}})j_l(k'a)j_l(ka)\langle M'm_s' \mid t(E) \mid Mm_s\rangle\delta_{LL'} \tag{6.6}$$

We substitute the potential and the t-matrix into the Lippmann-Schwinger equation. Again using the orthonormality of the Spherical Harmonics, and cancelling out the Spherical Bessel functions, we find

$$\begin{aligned}\sum_L\langle M'm_s' \mid t(E) \mid Mm_s\rangle = \frac{-2a^2}{\pi}&\sum_L\langle M'm_s' \mid (g + J\boldsymbol{S}\cdot\boldsymbol{\sigma}) \mid Mm_s\rangle \\ &-\frac{2a^2}{\pi}\int dk''\, k''^2\left\{\sum_{L\, m_s''\, M''} j_l^2(k''a)G_0^R(k''; E)\times\right. \\ &\left.\langle M'm_s' \mid (g + J\boldsymbol{S}\cdot\boldsymbol{\sigma}) \mid M''m_s''\rangle\langle M''m_s'' \mid t(E) \mid Mm_s\rangle\right\} \ .\end{aligned} \tag{6.7}$$

If we call $-2a^2/\pi = V_l$ and use $g_l(E_{k''})$, which was calculated in chapter 4, to represent the Green's Function and the result of the remaining k integrals, we get a equation that reduces to a form similar to the non-spin t-matrix;

$$\begin{aligned} t_s(E) &= V_l(g + J\boldsymbol{S}\cdot\boldsymbol{\sigma}) + V_l g_l(E_{k''}) t_s(E)(g + J\boldsymbol{S}\cdot\boldsymbol{\sigma}) \\ &= V_l(1 - V_l g_l(E_{k''})(g + J\boldsymbol{S}\cdot\boldsymbol{\sigma}))^{-1}(g + J\boldsymbol{S}\cdot\boldsymbol{\sigma}) \end{aligned} \tag{6.8}$$

The spin-spin interaction $J\boldsymbol{S}\cdot\boldsymbol{\sigma}$, is a 4×4 matrix for two electron spins of $S = 1/2$. There are only six non-zero matrix elements and Table 6.1 gives these elements and the physical scenarios they represent.

Element	Entry	Spin before Scatter		Spin after Scatter		
		Impurity	Electron	Impurity	Electron	
$\{1,1\}$	J	up	up	up	up	Same spin, no spin flip
$\{4,4\}$	J	down	down	down	down	Same spin, no spin flip
$\{2,2\}$	-J	up	down	up	down	Opp. spins, no spin flip
$\{3,3\}$	-J	down	up	down	up	Opp. spins, no spin flip
$\{2,3\}$	J/2	down	up	up	down	Opp. spins, spin flip
$\{3,2\}$	J/2	up	down	down	up	Opp. spins, spin flip

Table 6.1: Matrix elements of the spin-spin interaction between two electrons given by $J\boldsymbol{S}\cdot\boldsymbol{\sigma}$.

The entries in the table are found by expanding out the spin operators using the raising and lowering operator notation;

$$\hat{S^+} = \hat{S}_x + i\hat{S}_y \quad ; \quad \hat{S^-} = \hat{S}_x - i\hat{S}_y \tag{6.9}$$

which gives

$$(g + J\boldsymbol{S}\cdot\boldsymbol{\sigma}) = g + JS_z\sigma_z + J\frac{S^+\sigma^-}{2} + J\frac{S^-\sigma^+}{2} \ . \tag{6.10}$$

The spin-spin interaction is limited by the restriction that scattering permutations where M and m_s change independently of each other are forbidden. The simplest interactions would be when neither the tunnelling electron nor the impurity electron spin changes value. This can happen if the spins are alike (elements $\{1,1\}$ and $\{4,4\}$), or if they are opposite to one another (elements $\{2,2\}$ and $\{3,3\}$). The remaining possible scenario is for the spins to start opposite to one another, and to both flip during the scatter, resulting in them still being opposite to one another (elements $\{2,3\}$ and $\{3,2\}$).

The scattering matrix is defined as before, but now in matrix form and with an unknown constant:

$$S = 1 - iCt(E_{\varkappa}) \tag{6.11}$$

As S is unitary, we can use it with its transpose to find C:

$$C = i[t(E_{\varkappa})]^{-1} \cdot [t(E_{\varkappa}) - t^{\dagger}(E_{\varkappa})] \cdot [t^{\dagger}(E_{\varkappa})]^{-1} = \frac{2m\pi\kappa}{\hbar^2} j_l^2(\kappa a) \tag{6.12}$$

for the non-relativistic case.

6.2 The relativistic and semi-relativistic t-matrix for a Delta Shell potential with an external spin.

The non-relativistic t-matrix for an external spin resulted in an expression which was very similar to the t-matrix for the bare Delta Shell potential. We find that this is the same for the relativistic case. The spin interaction matrix doesn't affect the manipulation of the t-matrix, and we start with a potential defined as

$$\begin{aligned} V_{\boldsymbol{k'}M'm'_s;\boldsymbol{k}Mm_s} &= V_{W'} \sum_{s} \sum_{\kappa\mu} \sum_{\kappa'\mu} \int d\Omega_r \, Y_{l'}^{*\mu'-s}(\hat{\boldsymbol{k}}') Y_l^{\mu-s}(\hat{\boldsymbol{k}}) C(l\tfrac{1}{2}j;\mu-s,s) \\ &\times \; C(l'\tfrac{1}{2}j';\mu'-s,s)\,(g + J\boldsymbol{S}\cdot\boldsymbol{\sigma})\; i^{l'-l} \begin{pmatrix} j_{l'}(k'a)\chi_{\kappa'}^{\mu'}(\hat{\boldsymbol{r}}) \\ iD' j_{\bar{l}'}(k'a)\chi_{-\kappa'}^{\mu'}(\hat{\boldsymbol{r}}) \end{pmatrix} \\ &\times \; \begin{pmatrix} j_l(ka)\chi_{\kappa}^{\dagger\mu}(\hat{\boldsymbol{r}}) & -iDj_{\bar{l}}(ka)\chi_{-\kappa}^{\dagger\mu}(\hat{\boldsymbol{r}}) \end{pmatrix} \end{aligned} \tag{6.13}$$

$V_{W'}$ is given by $V_W/g = -2a^2(W + mc^2)/(2\pi W)$, and $D = \hbar ckS_{\varkappa}/W + mc^2$ as before.

The energy term of the t-matrix is given by

$$
\begin{aligned}
t_{M'm'_s;Mm_s}(W) \quad = \quad & V_{W'}\left[1 - V_{W'}\left(g + J\boldsymbol{S}\cdot\boldsymbol{\sigma}\right)\sum_{s\kappa\mu}\int d\Omega_r \int_0^\infty dk\, \frac{k^2 C(l\tfrac{1}{2}j;\mu-s,s)^2}{(pc)^2-(\hbar ck)^2+i\epsilon}\right. \\
\times \quad & \begin{pmatrix} j_l(ka)\chi_\kappa^{\dagger\mu}(\hat{\boldsymbol{r}}) & -iDj_{\bar{l}}(ka)\chi_{-\kappa}^{\dagger\mu}(\hat{\boldsymbol{r}}) \end{pmatrix} \\
\times \quad & \begin{pmatrix} W+mc^2 & 0 & -\hbar ck & 0 \\ 0 & W+mc^2 & 0 & \hbar ck \\ -\hbar ck & 0 & W-mc^2 & 0 \\ 0 & \hbar ck & 0 & W-mc^2 \end{pmatrix} \\
\times \quad & \left.\begin{pmatrix} j_l(ka)\chi_\kappa^{\mu}(\hat{\boldsymbol{r}}) \\ iDj_{\bar{l}}(ka)\chi_{-\kappa}^{\mu}(\hat{\boldsymbol{r}}) \end{pmatrix}\right]^{-1} \left(g + J\boldsymbol{S}\cdot\boldsymbol{\sigma}\right)\ . \qquad (6.14)
\end{aligned}
$$

Once the integrals are performed, this evaluates to

$$
\begin{aligned}
t_{M'm'_s;Mm_s}(W) \quad = \quad & \left[1 - V_{W'}\left(g + J\boldsymbol{S}\cdot\boldsymbol{\sigma}\right)\left(\frac{W+mc^2}{2\hbar^2c^2}\frac{\pi p}{\hbar}(j_l n_l - ij_l^2)\right.\right. \\
+ \quad & \left.\left.\frac{W-mc^2}{(W+mc^2)^2}\frac{\pi}{2}\left(\frac{p}{\hbar}\right)^3(j_{\bar{l}}n_{\bar{l}} - ij_{\bar{l}}^2)\right)\right]^{-1} V_{W'}\left(g + J\boldsymbol{S}\cdot\boldsymbol{\sigma}\right)\ . \\
& \qquad (6.15)
\end{aligned}
$$

The arguments of the Bessel functions above are $pa/\hbar$.

6.3 Phase Shift Results

The scattering matrix has non-zero elements in the same places as there were in the spin-spin interaction matrix. Each of these terms are rewritten in terms of phase shifts, and three different entries are found. For the non-relativistic, the semi-relativistic and the full relativistic approach, the entries all have the same form, which we denote by their position in the spin-spin matrix;

$$\tan\delta_{\{1,1\}} = \frac{DH_a(g+J)}{DH_a(g+J)+1}$$

$$\tan\delta_{\{2,2\}} = \frac{DH_b[-4Dg^2(H_a+iH_b)+4g(1+2DJ(H_a+iH_b))-J(4+3DJ(H_a+iH_b))]}{4-4D(2H_a+iH_b)(g-J)+D^2H_a(H_a+iH_b)(4g^2-8gJ+3J^2)}$$

$$\tan\delta_{\{2,3\}} = \frac{i[4-8D(H_a+iH_b)(g-J)-4iDJH_b+D^2(H_a+iH_b)^2(4g^2-8gJ+3J^2)]}{4-4D(2H_a+iH_b)(g-J)+D^2H_a(H_a+iH_b)(4g^2-8gJ+3J^2)}$$

The variables D, H_a and H_b are given in Table 6.2 for the three different approaches.

Case	$D/\left(\frac{-2a^2}{\pi}\right)$	H_a	H_b
NR	1	$\frac{m\pi k}{\hbar^2} j_l(ka) n_l(ka)$	$-\frac{m\pi k}{\hbar^2} j_l^2(ka)$
Rel	$\frac{W+mc^2}{2W}$	$\frac{W+mc^2}{2\hbar^2c^2}\frac{\pi p}{\hbar} j_l\left(\frac{pa}{\hbar}\right) n_l\left(\frac{pa}{\hbar}\right)+$ $\frac{W-mc^2}{(W+mc^2)^2}\frac{\pi p^3}{2\hbar^3} j_{\bar{l}}\left(\frac{pa}{\hbar}\right) n_{\bar{l}}\left(\frac{pa}{\hbar}\right)$	$-\frac{W+mc^2}{2\hbar^2c^2}\frac{\pi p}{\hbar} j_l^2\left(\frac{pa}{\hbar}\right)$ $-\frac{W-mc^2}{(W+mc^2)^2}\frac{\pi p^3}{2\hbar^3} j_{\bar{l}}^2\left(\frac{pa}{\hbar}\right)$
SR	1	$\frac{m\pi k}{\hbar^2} j_l(ka) n_l(ka)$ $+\frac{\hbar^2k^5\pi}{16m^3c^4} j_{\bar{l}}(ka) n_{\bar{l}}(ka)$	$-\frac{m\pi k}{\hbar^2} j_l^2(ka)$ $-\frac{\hbar^2k^5\pi}{16m^3c^4} j_{\bar{l}}^2(ka)$

Table 6.2: The components for the phase shifts when scattering from a Delta Shell potential with an external spin. The non-rel., semi-rel. and rel. approach all obey the same phase shift equations, but with different components.

We now go on to describe the behaviour of the phase shifts for the three possible scattering scenarios. The behaviour of the three entries are different from one another, but general patterns are followed for all the graphs of angular momentum 0, 1 and 2 separately. We will only look at the semi-relativistic results now, for reasons detailed in the previous chapter.

6.3.1 Scattering between two similar spins with no spin flip

Here, both the tunnelling electrons and the impurity electron have spins pointing in the same direction. The actual direction of the spins (up or down), has no effect on the results. We first study what happens for a constant value of the spin-spin interaction variable $\tilde{J}$, ($\tilde{J} = 0.2$). As the potential is increased, the graphs behave as they did when there was no external spin. The $l = 0$ curve moves to a phase shift of π at zero energy via an abrupt jump from $\pi/2$. However the potential strength at which this jump occurs is not $\tilde{g} = 1$, as in the previous case, but rather $\tilde{g} = 0.8$. This is because the occurrence of a resonance at zero energy is now determined by the sum of the shell potential strength and the spin-spin interaction strength. The phase shift begins at $\pi/2$ when $\tilde{g} + \tilde{J} = 1$. This relationship holds as $\tilde{J}$ is increased. The location of the bound states ($\tilde{\xi} = \pi^2$, $4\pi^2$ etc) match those for no external spin coupling; introducing $\tilde{J}$ has no effect on the location.

For the $l = 1$, 2 cases, the graphs show the same behaviour again as their spinless counterparts except for when the zero-energy phase shift jumps to π. This now occurs when $\tilde{g} + \tilde{J} = 2l + 1$, and again, the higher bound states occur at the same location in energies as previously. For these curves and all following ones, there is no effect if the radius of the Delta shell potential is changed.

We now consider the spin-orbit splitting of the p- and d-wave phase shifts. This can be quantified by either finding the difference in energy for a given phase shift, as described in the previous chapter, or by finding the difference in the phase shift for a given energy. This is what we choose to study here. Both give a measure of the size of the splitting, but the second technique is easier to obtain graphically. We find that the phase shift difference follows a continuous line intersected by peaks that increase in height as the energy is increased (see Figure 6.2).

The peaks occur just after the bound state energies, and reflect the differences seen in the phase shifts when resonances occur. As the potential strength increases the peaks become more localised in energy as a consequence of the resonances becoming sharper. The amplitude of the peaks also increase due to the resonances becoming thinner. As they become more ‘upright’, the vertical distance between the spin-split graphs increase. Because of the symmetric relation between the potential strength and the spin-spin coupling, the same

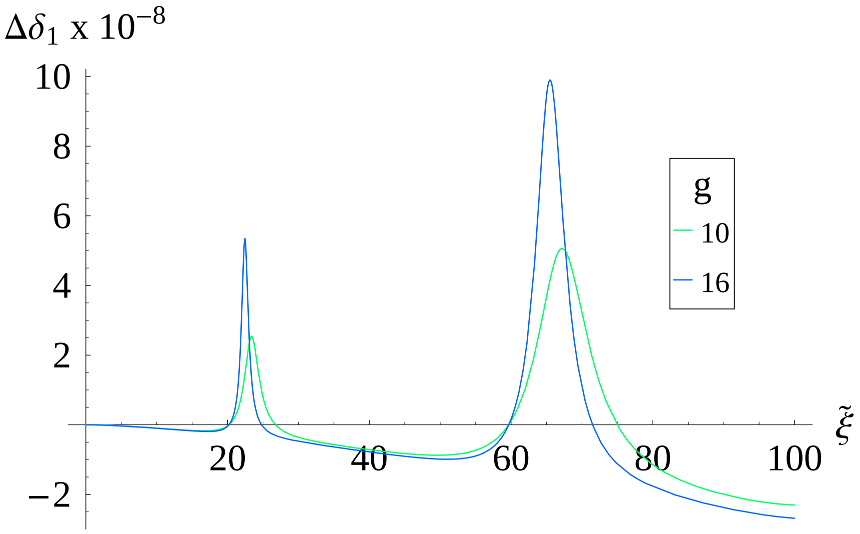

Figure 6.2: The difference in phase shift for the $P_{1/2}$ and $P_{3/2}$ states. This is for similar spins scattering with no spin flip for $\tilde{J} = 2$ and $\tilde{g} = 10$ and 16. As either $\tilde{g}$ or $\tilde{J}$ are increased the peaks get taller and thinner due to the resonance states becoming more localisd in energy.

behaviour is shown when we increase the value of $\tilde{J}$.

6.3.2 Scattering between two dissimilar spins with no spin flip

The general shape of the phase shift profile for dissimilar spins is the same as that of the same spins. However the phase shift ‘lags’ when either the shell, or the spin interaction potential is changed (see Figure 6.3(a)).

As the spin interaction between opposite spins was given by $-\tilde{J}$, we postulate that as the total potential for same spins was $\tilde{g}+\tilde{J}$, the potential for opposite spins is given by $\tilde{g}-\tilde{J}$. This would explain the slower rise in phase shift when compared to the same spin profile. The phase shifts depend on the potentials together, so an opposite spin scatter is viewed as if it is a same spin scatter but with a smaller total potential.

When the spin interaction strength is large however, rather than just seeing a delayed phase increase, we see the addition of small secondary peaks occurring around the resonances. After the resonance jumps, we also see small dips in the phase shift profile that grow

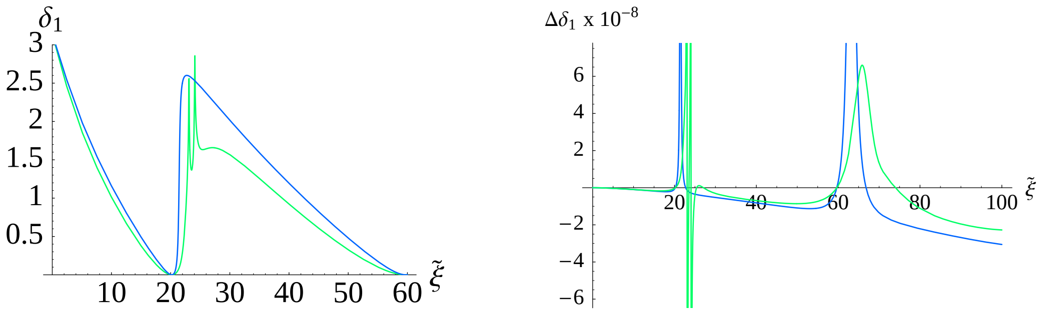

(a) Phase shifts for the similar and dissimilar spins with no spin flip. The phase shift for dissimilar spins is smaller than the phase shift for similar spins, and spikes have started to appear in the profile.

(b) The difference in phase between the spin-split $P_{1/2}$ and $P_{3/2}$ states.

Figure 6.3: Comparison of the phase shifts for scattering between similar (blue) and dissimilar (green) spins with no spin flip. $\tilde{g} = 23$ and $\tilde{J} = 10$.

with increasing $\tilde{J}$ and disappear as we take $\tilde{J}$ to zero. These spikes can be seen in Figure 6.3(a). For very large values of $\tilde{J}$, the baseline of the phase shifts is raised such that it never reaches zero at the bound state energies.

Figure 6.4 shows a scatter dominated by such a value of $\tilde{J}$. Excluding the peaks, the overall variance in the phase shifts have decreased from π, but the minimum value of the phase shift has been raised up to $\delta_l = \pi/2$. This can be explained by the relation between $\tilde{g}$ and $\tilde{J}$. When $\tilde{J} > \tilde{g}$, $\tilde{g} - \tilde{J}$ is negative, which changes the potential from being attractive to repulsive. A repulsive potential cannot bind an electron, so the signature of a bound state ($\delta_l = 0$ here), is removed. The phase shift of $\pi/2$ suggests *only* strong scattering is occurring. A phase shift of zero or π signifies weak scattering or bound states.

This effect can also be be seen when $\tilde{g}$ is less than $2l + 1$. When $\tilde{g} < \tilde{J}$ in this range, the phase shift is approximately equal to π across the whole energy spectrum. Closer observation shows a slight oscillation such that the phase shift is a maximum at energies corresponding to the bound states. This appears to be some kind of reflection in the phase shifts, but the scenario is not physically interesting to us so we do not investigate it further.

If we look at the phase shift behaviour when varying $\tilde{g}$ or $\tilde{J}$ on a 3D plot (Figure 6.5),

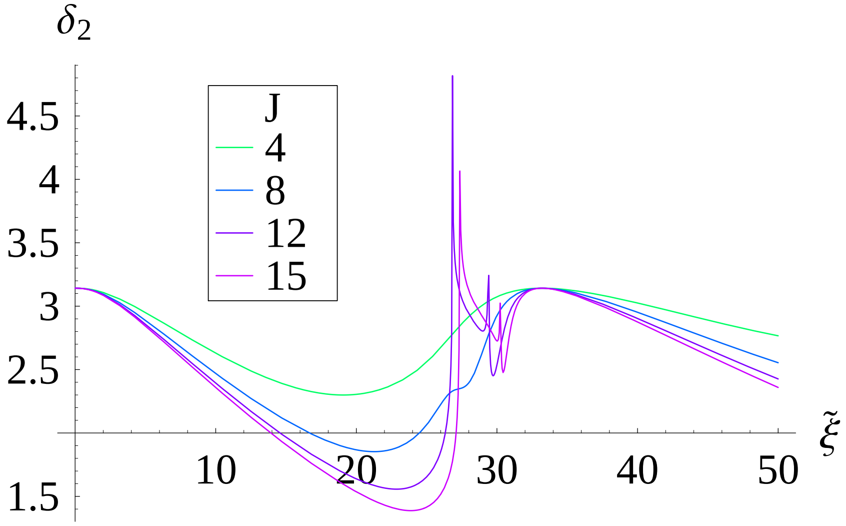

Figure 6.4: A large value of the spin interaction strength $\tilde{J}$ combined with a small shell potential ($\tilde{g} = 0.2$), results in a repulsive potential which cannot support a bound state. Instead the electrons are strongly scattered. This is a d-wave scattering profile.

we can see more clearly the effect that $\tilde{J}$ has on the phase shifts, and view the secondary peaks mentioned above. For a fixed value of $\tilde{J}$, we see ellipses in the $(\tilde{g}, \tilde{\xi})$ plane running mainly along the direction of the energy axis. These ellipses are split along the long axis with a π jump in the phase shift defining the split, and thin peaks defining the borders of the ellipses. At zero energy the jump appears to occur at $2l + 1 = \tilde{g} - \tilde{J}$, running into smaller potential values when the energy is increased. This appears to be the occurrence of a bound state at zero energy. The width of the ellipses, (the distance between the peaks), is equal to $\tilde{J}$. This gives us a quantitative description of how much broader the resonance becomes in the case of opposite-spin scattering.

The length of the ellipse depends on the angular momentum value. For $l = 0$ the ellipse cuts into the zero-energy axis, appearing as a semi-circle before it ends. For $l = 1$ and 2 the ellipse is longer in energy. Figure 6.5 shows the $l = 1$ ellipse.

We know from Wigner [71] that the width of the resonance is directly related to the time the particle is captured by the potential for ($t_l^D = \hbar d\delta_l/dE$). The reduced phase shifts (when $\tilde{J}$ is small) result in a broadened resonance which indicates that the presence of the

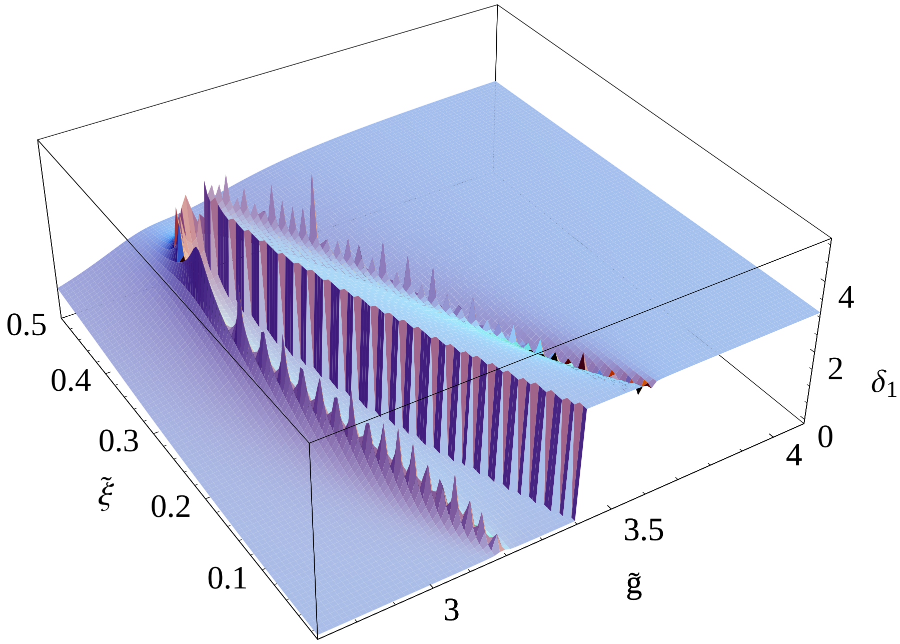

Figure 6.5: The potential strength and energy distribution of the phase shifts for $l = 1$ for dissimilar spins scattering with no spin flip. The jump in π signifying a bound state, occurs at a value of $\tilde{g} - \tilde{J} = 2l + 1$ and the width of the entire feature is equal to $\tilde{J}$ ($= 0.4$ here).

opposite spin interaction has reduced the time the electrons are captured for. For larger $\tilde{J}$, where the secondary peaks seen in Figure 6.5 appear, the peaks can also be seen as broadening the resonance, again reducing the time the electrons are bound for.

If we plot the difference in phase between the spin-split $l = 1$ graphs, we find a very similar structure to the graph describing the scattering of same spins with no spin flip. However the location of the peaks are shifted to reflect the total reduced potential (Figure 6.3(b)), and the extra spikes due to $\tilde{J}$ result in larger, more confined differences.

6.3.3 Scattering between two dissimilar spins with a spin flip

Now we look at the scattering of two opposite spins which flip their spins during the scatter. The phase shift profiles for this scattering scenario are very different to the previous two.

This scattering scenario has features at the same locations as the resonances seen in the other scenarios. However, rather than seeing a rapid rise through π at the resonance and bound states, then a slow decrease back to zero, the phase shifts instead look like sharp peaks, with an almost symmetric rise and fall. Figure 6.6 shows this and another difference between this scattering scenario and the previous two. The phase shifts have previously all been constrained to a maximum value of π. When scattering with a spin flip, they start at 2π and higher, and in one cycle (defined as moving from one peak to the next) the phase shift changes by more than π. The phase shift appears enlarged as well as displaced in δ.

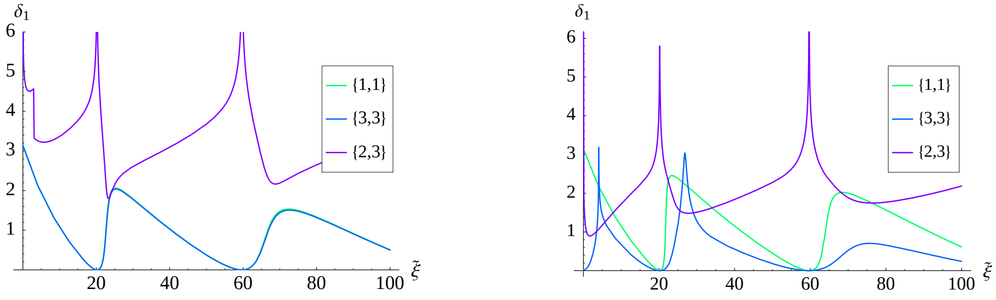

(a) $\tilde{J} = 0.2$

(b) $\tilde{J} = 10$

Figure 6.6: A comparison of the phase shifts for scattering with a spin interaction: Same spin scatter with no spin flip ($\{1,1\}$), dissimilar spins with no spin flip ($\{3,3\}$), and dissimilar spins with a spin flip ($\{2,3\}$). The effect of an increased $\tilde{J}$ is shown in the second graph. $\tilde{g} = 16$

We examine the features at zero energy by studying the change in the phase shift with the interaction strength $\tilde{g}$ (Figure 6.7). When the spin-spin interaction strength $\tilde{J}$ is increased, a dip appears in the phase shifts. The two sides of the dip occur at values of $\tilde{g}$ and $\tilde{J}$ that satisfy the relations

$$\tilde{g} - \frac{\tilde{J}}{2} = 2l + 1 \qquad \tilde{g} - \frac{3\tilde{J}}{2} = 2l + 1 \tag{6.16}$$

The width of the dip is equal to $\tilde{J}$, which is the same as was found in the scattering between dissimilar spins with no spin flip. However, here there is no jump of π splitting the trough in half.

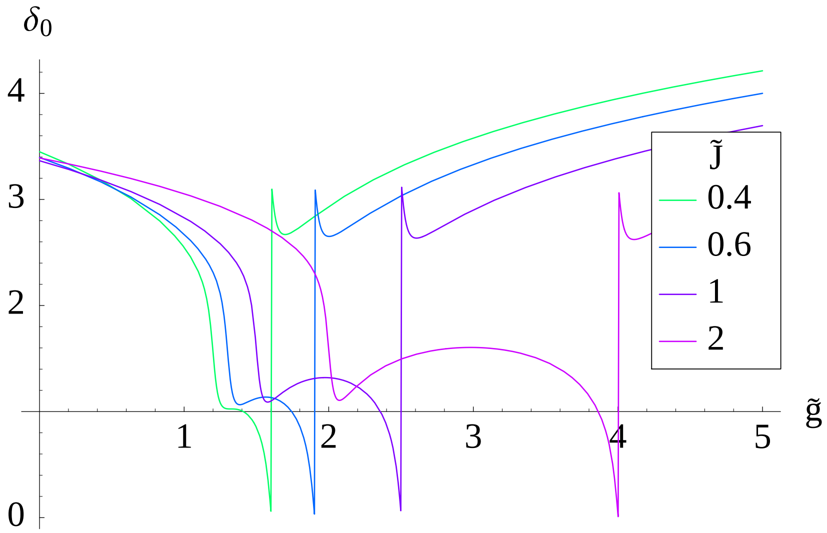

Figure 6.7: S-wave scattering for dissimilar spins scattering with a spin flip. The spin-spin interaction strength $\tilde{J}$ is varied, and troughs of width $\tilde{J}$ appear. The graphs are plotted at zero energy.

It was expected that the total potential should change as $\tilde{g} + \tilde{J}/2 = 2l + 1$, in the same manner in which the potential was related to the spin-spin interaction matrix for the previous scatterings. However this doesn't appear to be case. A plot of energy versus phase shifts instead shows a step that runs from $(\tilde{\xi}, \delta) \approx (0, \pi)$ that only appears after the threshold condition of $\tilde{g} - 3\tilde{J}/2 = 2l + 1$ is reached.

If we study a 3D plot of the phase shifts as a function of energy and potential strength (Figure 6.8), instead of the ellipses that characterised no spin flip scattering between dissimilar spins, we see thin parabolic steps that run along the $\tilde{g}$ axis for a short distance just after a peak occurs.

As we look to higher instances of this feature, higher values of potential strength are needed before they occur, and the background level of the phase shifts increases such that the steps get shallower. These features could almost be resonance behaviour as they require a minimum potential to occur, and appear just after the usual bound state energies. However the numerical values of the phase shifts suggest that this isn't the case.

In Figure 6.6 we show the change in phase shift profile when $\tilde{J}$ is large. The background

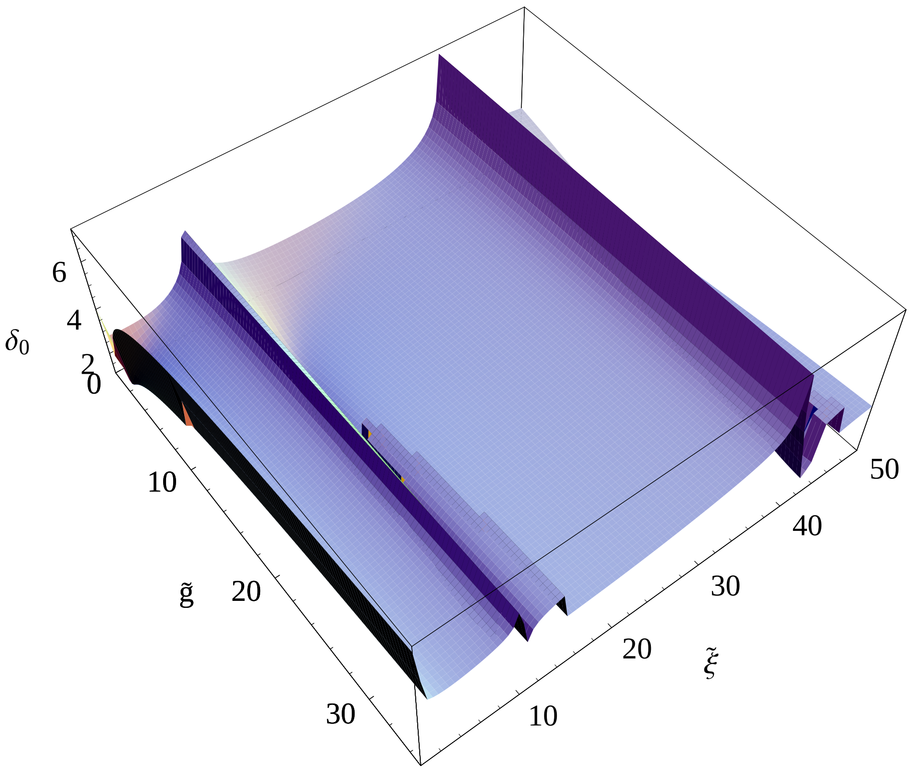

Figure 6.8: The potential and energy dependence of the phase shift for s-wave scattering between two dissimilar spins with a spin flip. Thin steps running along $\tilde{g}$ can be seen just after the peak feature. The second occurrence of a step can be seen starting at $(\tilde{\xi},\, \tilde{g}) \approx (45, 30)$.

level of the phase shift has dropped as $\tilde{J}$ is increased, and the troughs occurring immediately after the peaks are not as resolved.

If we increase $\tilde{J}$ above $\tilde{g}$, we see troughs appear in the phase shift profile just before the bound state energies. Figure 6.9 shows δ_1 for three different values of $\tilde{J}$. These troughs appear to be artefacts of the plotting technique in which a phase shift greater than π is translated to start at $\delta_l = 0$. This does not signify resonance behaviour, but it may still be instructive to show how this behaviour changes for large $\tilde{J}$.

The troughs occur over a width which grows rapidly with $\tilde{J}$, but with a depth that has a slow response to increasing $\tilde{J}$. For very large $\tilde{J}$ values, the trough still remains, and

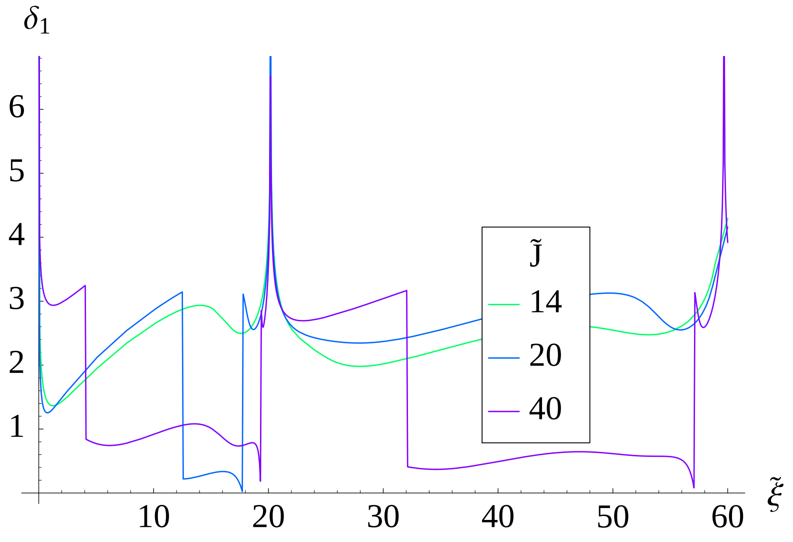

Figure 6.9: The p-wave scattering for dissimilar spins scattering with a spin flip. Increasing $\tilde{J}$ above $\tilde{g}$ (14 here), introduces steps of π in the phase shifts, which only represent a translation of the phase shifts greater than π. The step widths lengthen with $\tilde{J}$.

doesn't appear to affect the development of the peak at the bound state energy.

The difference between this scattering scenario and the others is clearly seen when the size of the phase shift difference between the spin-split p-wave states are considered. The phase shift difference is much larger for spin-flip scattering, and the maximum occurs at lower energies than the others. Whilst the other scenarios showed $\Delta\delta$ getting greater and more localised in energy as the potential was increased, here the phase shift difference gets wider in energy, and more features appear after the main peak. Increasing $\tilde{J}$ has more effect on the phase difference for scattering scenarios without a spin flip than it does on the one with a spin flip. The phase shift differences for all three scattering scenarios are shown in Figure 6.10.

6.4 Conclusions

For moderate values of the spin interaction strength, the effect of an additional potential on the phase shifts for scattering without a spin flip is to change the energies of the

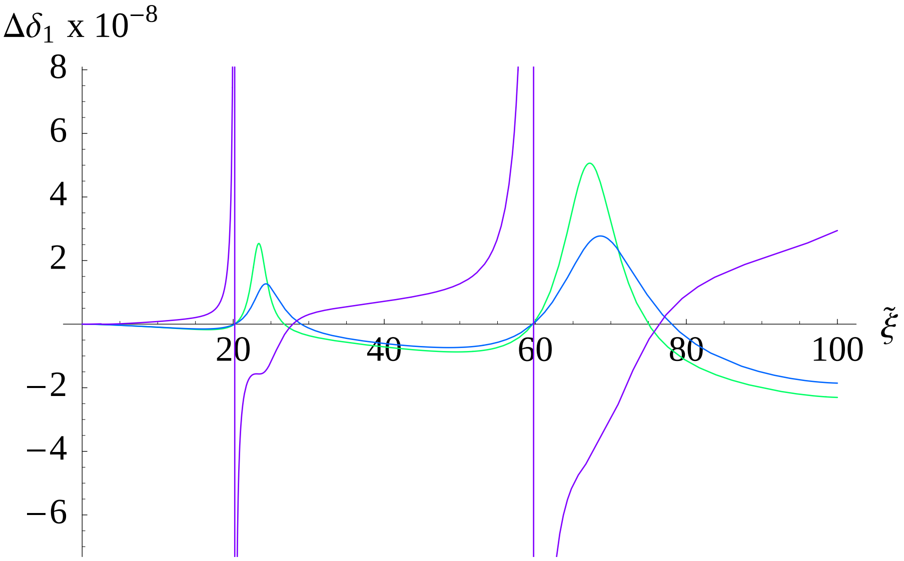

Figure 6.10: The p-wave phase shift differences for all three scattering scenarios; Green represents $\{1, 1\}$, Blue, $\{3, 3\}$, and Purple, $\{2, 3\}$. $\tilde{g} = 10$.

resonances. The bound state at zero energy appears when $2l + 1 = \tilde{g} + \tilde{J}$ for same spins, and at $\tilde{g} - \tilde{J}$ for opposite spins. The phase shift profiles appear to depend on the sum of the potentials only.

When $\tilde{J}$ increases however, for spins orientated opposite to one another, the general phase shift pattern does acquire additional features. The jumps in π determining a resonance at non-zero energies are flanked by peaks that occur at $\pm\tilde{J}/2$ of the resonance location. This has the effect of broadening the resonances which reduces the time that the electrons are captured by the shell. We saw that for $\tilde{J} > \tilde{g}$, the potential switched from being an attractive to a repulsive one, which resulted in no bound states being possible. This general broadening as $\tilde{J}$ was increased can be viewed as a development towards that scenario.

Transitions that involved a spin flip displayed complicated phase shift behaviour, and no obvious dependence on $\tilde{g} + \tilde{J}/2$ was seen, although it was expected from the behaviour of the previous scattering scenarios.

There was no usual resonance or bound state behaviour, although large peaks did appear at the resonance energies. The range of the phase shifts were greater than π, and was mostly not retractable back to the range of 0 to π. It is unclear what these phase shifts represent.

Resonance-like behaviour was observed when the potential strength was increased, but the phase shifts didn't pass through π, or go to zero. This could indicate that the potential was unable to support a bound state, but because of the increased range of the potential, and the lack of transitions through π, it isn't clear how to interpret the figures.

The non-zero value of δ_l could indicate a general background level of scattering, and the peaks could signify enhanced scattering or no scattering at all. As we are comparing three different scattering scenarios it may be good enough at the moment to just view the phase shift as being different from the patterns produced for the simple scattering, and therefore completely identifiable.

The reason for studying this model in the semi-relativistic limit, was to include the electron spin-orbit interaction. When looking at the difference in phase shifts between the two different profiles arising from the interaction, the maximum difference between spin-split states was found for when the scatter involved a spin flip. As the interaction strength was increased, the energy range for which the splitting is large increased for this case. The other two scattering scenarios showed a greater difference when the potentials were increased, but over a smaller range.

However the differences are very small. The differences in the phase shifts noted here are $\sim 10^{-8}$, and the energy differences calculated in Chapter 5 were $\sim 10^{-5}$ in our dimensionless units. This corresponds to energies on the scale of 10^{-5} eV. The magnitude of the spin signal measured by Durkan [54] was around 200 nV. It therefore seems unfeasible that an energy difference such as we have found for the spin-orbit coupling could be measured experimentally here.

6.5 Summary

This information describes the transition of an electron wave through a potential shell with a spin, which we have taken to model a free-radical molecule in an STM experiment. The three different scattering possibilities give very different phase shift signatures. The effect of an increasing spin interaction separates the behaviour of similar spins and dissimilar spins, and the phase shift differences between the spin-split p- and d-wave scattering states easily identifies which scatters are accompanied by a spin flip. The spin flip scattering doesn't display typical resonance behaviour, but does have enlarged phase shift signatures at the usual resonance energies. The size of the spin-split phase shift differences have been found to be too small to be observed experimentally. These results will be taken forward and will be combined with the transition results through a bare Delta Shell to calculate the conductance through an entire STM system.

Chapter 7

Delta Shell Scattering with a Precessing Spin

The previous chapter described the phase shifts due to an interaction between two static spins. Here, we introduce a precessing spin as the molecule spin such that the applied magnetic field that features in the experiments can be included in the model. Rather than only examining the phase shifts generated by the potential, in this chapter the scattering amplitudes, the total scattering cross section, and the generalised phase shifts are also studied. This chapter deals with the molecule only, and its effect on an incoming electron wave.

7.1 Motivation

In the Durkan experiment, the sample was sitting on a permanent magnet with its axis in the direction of the STM tip. What effect, if any, does this magnetic field have on the phase shifts due to the shell potential and the spin interaction?

Let us assume that under the influence of the external magnetic field the molecule spin precesses with a relaxation time large enough to ensure that no decoherence of the spin occurs in the observational time frame. By having this restriction, we assume that either the observational time is short, or that there is an unknown mechanism perturbing the electron away from its equilibrium position often enough such that it is always precessing.

It is important to emphasize here that we are not claiming anything about the nature of, or cause of the precessing spin. This is not an ESR experiment with an oscillating field so we cannot look to that as a source of perturbation.

Electrons in an applied magnetic field will have their energy modified by Zeeman coupling. Depending on whether they are aligned with or against the direction of the field, this energy difference is given by $\pm g_e \mu_B B$, with the positive value taken when aligned against the field. The authors in [47] maintain that this Zeeman coupling of the electrons to the external magnetic field is very small when compared to the exchange coupling to the local spin. For the magnetic fields used in the experiments we are studying, (0.019 – 0.03 T), the size of the splitting is $\sim 2.2 - 3.4 \times 10^{-5}$ eV. We therefore choose to neglect this interaction, concentrating on the spin interaction instead.

In Chapter 2, we calculated that $\sim$ 10 electrons will pass by the molecule during one precessional period. Knowing this, we can treat the system adiabatically and assume that the impurity spin is static for a single electron tunnelling event. This approach is used in [47] and we use formalism from that work in our Delta Shell model to investigate the phase shifts that will arise from such a system.

It is worth noting that in this adiabatic situation, the local spin is treated as precessing, and the conduction electron spins are static. Because of the symmetric way they are treated, the same result would be achieved if we chose the local spin to be static and the conduction electrons to be precessing.

7.2 A Precessing Spin

The precessing spin is described by the following components;

$$\begin{aligned} S_x &= S \sin\theta \cos\phi \\ S_y &= S \sin\theta \sin\phi \\ S_z &= S \cos\theta \ , \end{aligned}$$

where θ and ϕ are the azimuthal and in-plane rotational angles respectively, and S is the magnitude of the spin vector $\boldsymbol{S}$. The equation of motion for the spin is given by

$$\frac{d\boldsymbol{\mu}}{dt} = \boldsymbol{\mu} \times \gamma \boldsymbol{B} \ , \tag{7.1}$$

where the magnetic field is in the z-direction only, $\boldsymbol{B} = (0, 0, B_z)$, and the magnetic moment $\boldsymbol{\mu}$ is the gyromagnetic ratio γ multiplied by the spin vector $\boldsymbol{S}$.

Coupling this spin to the free electron spin $\boldsymbol{\sigma}$, (described by the three Pauli matrices) in an exchange interaction characterised by $\boldsymbol{\sigma} \cdot \boldsymbol{S}$, gives a coupling matrix of;

$$\boldsymbol{\sigma} \cdot \boldsymbol{S} \ = \begin{pmatrix} \cos\theta & \sin\theta \exp[-i\omega_L t] \\ \sin\theta \exp[i\omega_L t] & -\cos\theta \end{pmatrix} \tag{7.2}$$

We have rewritten the angle of rotation ϕ as $\omega_L t$, the frequency of precession (the Larmor frequency) multiplied by the time. We assume the position of the spin vector at time t_0 is in the x-z plane i.e. the y component is zero. This interaction enters the potential term in the non-relativistic spin t-matrix equation from the previous chapter;

$$t_s(E) = V_l[1 - V_l g_l(E)(g + J\boldsymbol{S} \cdot \boldsymbol{\sigma})]^{-1}(g + J\boldsymbol{S} \cdot \boldsymbol{\sigma}) \tag{7.3}$$

The scattering matrix is found using the same method as for the static spins. This results in a 2 by 2 non-diagonal scattering matrix.

In the previous chapter, we analysed the phase shifts from the entries of the s-matrix individually, without diagonalising the s-matrix first. We will use this method to study the scattering states due to a precessing spin, but we will also look directly at the amplitudes given by each term in the s-matrix.

We also choose to move the spin of the tunnelling electron into the frame of the precessing spin. This shows the interaction from a static viewpoint, such that for an instantaneous time, the tunnelling electron is either parallel or antiparallel to the precessing local spin. However, by diagonalising the s-matrix, we lose sight of the good quantum numbers that define each matrix entry, and can only specify the angular momentum number l, of each entry. Strange [67] says that by diagonalising we end up with a generalised phase shift only, which we will briefly study below.

As well as looking in detail at the effect the potential has on each scattering channel, it is instructive to examine the effect on all of the channels together. This may give a better insight into any experimentally observable effect, as the differentiation between the different scattering channels is only possible with further manipulation of the experimental parameters (e.g. a spin-polarised current could be used to differentiate between the scattering elements describing different spin orientations). To do this, the total scattering cross section is determined from the t-matrix. A description of this is set out in the next section.

7.3 The Total Scattering Amplitude

A simple scattering experiment can be modeled with a plane wave of intensity I_0 incident on a target. The plane wave is then scattered, resulting in an angular distribution of scattered wave components $I(\theta, \phi)$, around the target. The scattered wave packet is described as a retarded, radially decaying version of the incident wave packet, modulated by an angular amplitude $f_k(\boldsymbol{r})$, known as the scattering amplitude [88].

Sampling the scattered wave at a particular angle results in the determination of the differential scattering cross section, which is shown in Ref. [88] and elsewhere to be given by

$$\frac{\mathrm{d}\sigma}{\mathrm{d}\Omega} = \frac{I(\theta, \phi)}{I_0} = \mid f_k(\boldsymbol{r}) \mid^2 . \tag{7.4}$$

The total cross section is found by integrating the differential cross section over all angles $\mathrm{d}\Omega$. The total cross section can have a few different meanings, and here it is taken to mean the sum of all possible processes integrated over all possible scattering angles.

The t-matrix is related to the scattering amplitudes by a simple relation, resulting in a total cross section of

$$\sigma = \frac{m^2 L^6}{4\pi^2 \hbar^4} \int \mid t(\boldsymbol{k'}, \boldsymbol{k} : \tilde{\xi}) \mid^2 \mathrm{d}\Omega . \tag{7.5}$$

The length L represents the dimension of the scatterer (a), and the t-matrix has units of energy, giving the cross section units of area. Similar to the other parameters used here, the cross section is re-written in dimensionless units by dividing through by the area of the scatterer;

$$\tilde{\sigma} = \frac{\sigma}{4\pi a^2} \tag{7.6}$$

The t-matrix is used in the semi-relativistic limit and is given by the product $t(\boldsymbol{k'}, \boldsymbol{k} : \tilde{\xi}) = t(\tilde{\xi})t(\boldsymbol{k'}, \boldsymbol{k})$

$$\begin{aligned} t(\boldsymbol{k'}, \boldsymbol{k}; \tilde{\xi}) &= \sum_{s} \sum_{\kappa\mu} \sum_{\kappa'\mu'} \int d\Omega_r (-) \frac{a}{\pi} \begin{pmatrix} j_{l'}(k'a)\chi_{\kappa'}^{\mu'}(\hat{\boldsymbol{r}}) \\ iD' j_{\bar{l}'}(k'a)\chi_{-\kappa'}^{\mu'}(\hat{\boldsymbol{r}}) \end{pmatrix} \\ &\times \begin{pmatrix} j_l(ka)\chi_{\kappa}^{\dagger\mu}(\hat{\boldsymbol{r}}) & -iDj_{\bar{l}}(ka)\chi_{-\kappa}^{\dagger\mu}(\hat{\boldsymbol{r}}) \end{pmatrix} Y_{l'}^{\mu'-s}(\hat{\boldsymbol{k}}')Y_{l}^{*\mu-s}(\hat{\boldsymbol{k}}) \\ &\times \left[1 + \sqrt{\tilde{\xi}}\left(\tilde{g} + \beta\tilde{J}\boldsymbol{S}\cdot\boldsymbol{\sigma}\right)\left((j_l n_l - ij_l^2) + \frac{\tilde{\xi}^2}{\widetilde{(2mc^2)}^2}(j_{\bar{l}}n_{\bar{l}} - ij_{\bar{l}}^2)\right)\right]^{-1} \\ &\times \left(\tilde{g} + \beta\tilde{J}\boldsymbol{S}\cdot\boldsymbol{\sigma}\right) \end{aligned}$$

The Bessel Functions in the third line have the argument $\sqrt{\tilde{\xi}}$, and $D = \hbar k S_\kappa/mc$. The vectors in the first two lines are expanded out, and the integral over Ω_r is carried out over the Spherical Harmonics in the Spin Angular Functions. The sums over κ' and μ' are carried out, and new Spin Angular Functions in $\boldsymbol{k}$ and $\boldsymbol{k'}$ are formed;

$$\begin{aligned} t(\boldsymbol{k'}, \boldsymbol{k}; \tilde{\xi}) &= \sum_{s} \sum_{\kappa\mu} (-) \frac{2a}{\pi} \\ &\times \begin{pmatrix} j_l(ka)j_l(k'a)\chi_{\kappa}^{\mu}(\hat{\boldsymbol{k}}')\chi_{\kappa}^{\dagger\mu}(\hat{\boldsymbol{k}}) & -\imath Dj_l(ka)j_{\bar{l}}(k'a)\chi_{\kappa}^{\mu}(\hat{\boldsymbol{k}}')\chi_{-\kappa}^{\dagger\mu}(\hat{\boldsymbol{k}}) \\ \imath D' j_{\bar{l}}(ka)j_l(k'a)\chi_{-\kappa}^{\mu}(\hat{\boldsymbol{k}}')\chi_{\kappa}^{\dagger\mu}(\hat{\boldsymbol{k}}) & 0 \end{pmatrix} t(\tilde{\xi}) \end{aligned}$$

The final two lines of the previous equation is written as $t(\tilde{\xi})$ above, and the fourth quadrant of the matrix goes to zero in the semi-relativistic limit. The κ sum runs from -3 to +2 (excluding $\kappa = 0$), covering the first three angular momentum values, and both the positive and negative coupling of the spin angular momentum to the orbital angular momentum.

7.4 Results

7.4.1 Amplitudes of the s-matrix entries

The phase shifts are calculated from the transition matrix, via the scattering or s-matrix. Aside from the phase change caused by the scattering potential, the amplitude of each s-matrix entry can be studied by plotting the real part of the amplitude against the imaginary part in a parametric plot. The magnetic field present in the experiment is incorporated into this model as the spin-interaction strength $\tilde{J}$. Figure 7.1 shows the effect that an increasing $\tilde{J}$, mimicking an increasing magnetic field, has on the off-diagonal s-matrix amplitudes.

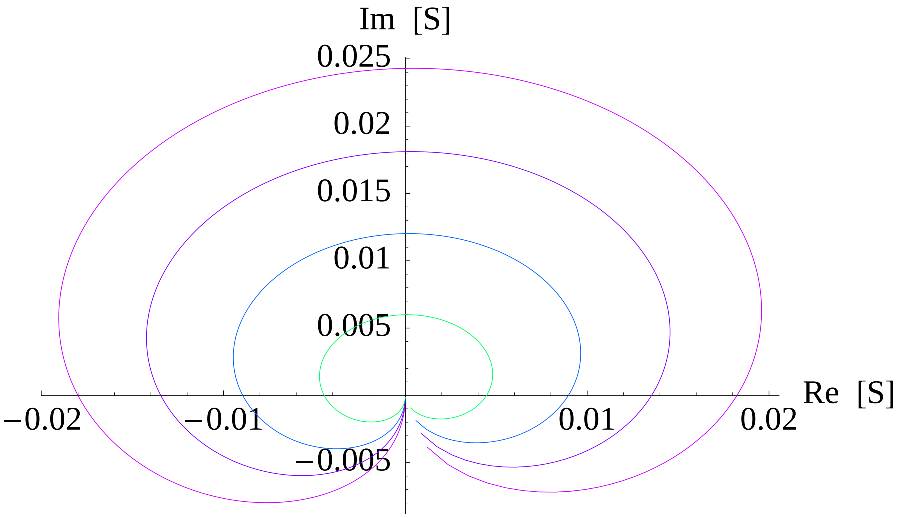

Figure 7.1: The s-wave off-diagonal s-matrix amplitudes plotted as a function of energy, and for increasing $\tilde{J}$ values. The green plot has a value of $\tilde{J} = 0.1$, and each successive plot has a $\tilde{J}$ value increased by 0.1. The energy dependence increases anti-clockwise around the plot. The potential strength is $\tilde{g} = 3$, and the azimuthal angle, $\theta = \pi/16$. $\phi = 0$.

Each plot starts at the origin when $\tilde{\xi} = 0$, and moves in the anti-clockwise direction. When $\tilde{J}$ is increased the plot increases in amplitude, but the phase changes, (the angular change Δ), remain the same - all plots start at the same point and follow similar, although enlarged paths. This plot is for energies up to $\tilde{\xi} = 9$. When the energy is increased further, the amplitude continues to zero when $\tilde{\xi} = \pi^2$, then the plot moves clockwise, forming a small loop that again moves back to zero amplitude at the origin. The formation of this loop and the consecutive one is shown in two stages in Figure 7.2 for one particular value of $\tilde{J}$. The energies at which the amplitude drops to zero corresponds to the energies at which the bound states occurred in the s-wave non-magnetic and static spin models.

When $\tilde{g}$ is increased in these plots, the pattern of loops stays the same, but the amplitudes and phases are changed. A high $\tilde{g}$ decreases the radius of the primary anti-clockwise circle. It also increases the phase changes in the loops, in such a way that the clockwise part of the loop becomes larger, the loop spreading over the top of the primary circle before looping back to become zero again at the bound state energy.

When increasing the azimuthal angle θ, we find that the amplitude of the s-matrix entries are increased (the radius increases) but there is no obvious change in the phase. Changing the in-plane angle, ϕ, however, visibly changes the phase, rotating it such that the lines do not emerge from the imaginary axis anymore. This can be seen in Figure 7.2 where $\phi = \pi/6$. The other off-diagonal entry in the s-matrix shows the same behaviour when most of the parameters are changed, except for when ϕ is increased, when the plots rotate in the opposite direction.

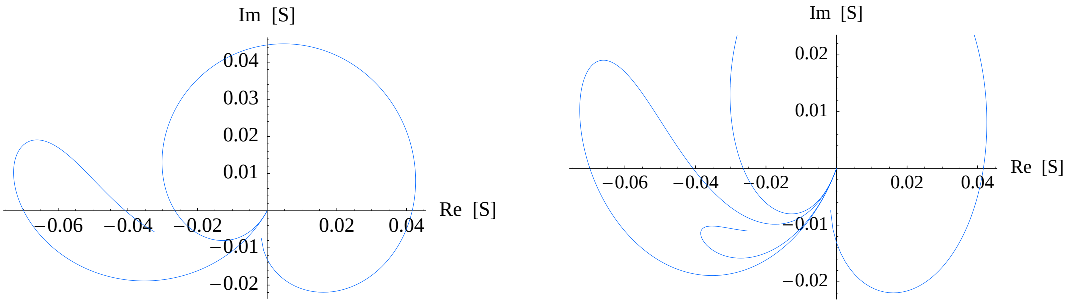

(a) Energies up to $\tilde{\xi} = 25$. (b) Energies up to $\tilde{\xi} = 65$.

Figure 7.2: The formation of loops in the s-wave off-diagonal s-matrix amplitude as $\tilde{\xi}$ is increased. The amplitude drops to zero at energies where bound states conventionally occur in the phase shifts. $\tilde{J} = 0.3$, $\tilde{g} = 3$, $\theta = \pi/6$.

When studying the diagonal s-matrix entries, we find that for intermediate values of $\tilde{g}$, the absolute values of the amplitudes are very close to unity, and deviate from it by only a small amount (Figure 7.3). As $\tilde{\xi}$ is increased, the plot moves rapidly through the positive imaginary region in an anti-clockwise direction, reaching $(1, 0)$ when $\tilde{\xi} = \pi^2$ (for the s-wave scattering). As the energy is increased further, the plot returns clockwise along the original path. It then returns to $(1, 0)$ for $\tilde{\xi} = 4\pi^2$. This is similar behaviour to the off-diagonal s-matrix elements: The phase and amplitude return to the same values at the bound state energies, and between the second and third bound state (and consecutive pairs), a loop is traced out. The differences between the two matrix elements are in the change in absolute amplitude (the off-diagonal plots are not unitary circles), and the phase at zero energy, $\Delta_l(0)$. In the diagonal entries, increasing the value of $\tilde{J}$ changes $\Delta_l(0)$, moving the entry clockwise for $\{1, 1\}$, and anticlockwise for $\{2, 2\}$. The behaviour at the bound state energies however, are not affected.

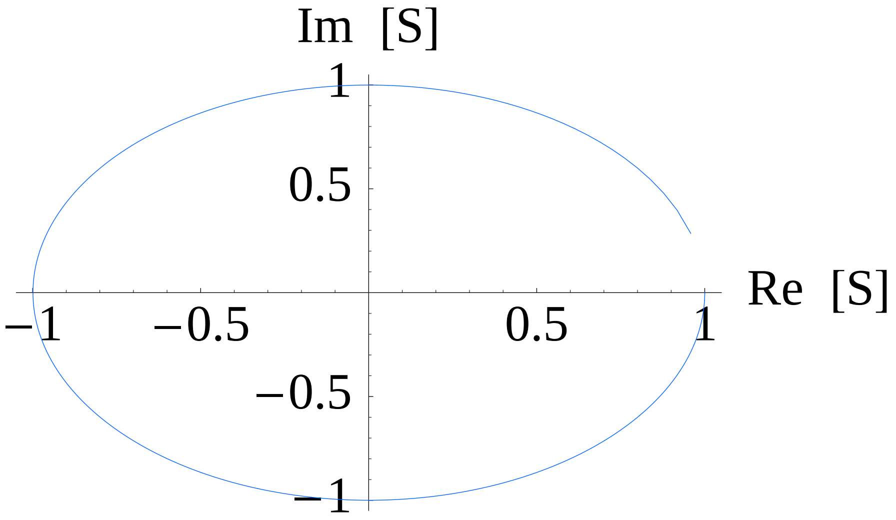

Figure 7.3: The s-wave diagonal s-matrix amplitude plotted as a function of energy. The energy dependence increases anti-clockwise around the plot, and its starting value depends on $\tilde{J}$. Here, $\tilde{g} = 3$, $\tilde{J} = 0.3$, and the azimuthal angle, $\theta = \pi/6$.

At low potentials the diagonal entries show unusual behaviour. For $\tilde{g} < 2l + 1$, the phase increases with energy in a clockwise direction, with $\Delta_l(0)$ always in the $(+ve, -ve)$ section of the graph and moving clockwise as $\tilde{g}$ is increased. The direction switches to anti-clockwise when $\tilde{g}$ passes $2l + 1$. For zero values of $\tilde{J}$, and as $\tilde{\xi}$ tends to zero, the plot starts at $(-1,0)$ for $\tilde{g} = 2l+1$, and jumps to start at $(1,0)$ when $\tilde{g} > 2l+1$. This jump is the jump in phase shift we have seen before for s-wave scattering in the non-magnetic case. Because the s-matrix and the phase shifts are related by $S = \exp(2i\delta_l)$, a change in the s-matrix phase Δ plotted here, by an amount θ, corresponds to a change in phase by $\theta/2$ in δ given by the usual phase shift plots. So this jump in Δ of π corresponds to the $\pi/2$ jump seen at zero energy in the s-wave phase shifts.

We can use the same comparison when considering the change a large $\tilde{g}$ has on the amplitude profile. When we considered the plots of phase shift versus energy in previous chapters, an increased potential increased the maximum phase shift that occurred between bound states. The $\delta_l = \pi/2$ line is the imaginary axis here, so if a loop crosses that line, it symbolises that a resonance has been reached. Figure 7.2 is for a small value of $\tilde{g}$ which isn't large enough to cause a resonance state, but an increased $\tilde{g}$ will increase the second loop, extending it further clockwise before it returns.

There appears to be no dependence on θ, and ϕ doesn't explicitly enter into the expression for the diagonal s-matrix entries.

7.4.2 Total Scattering Cross Section

The incoming electron is confined to the z-axis so that $\Omega_k = 0$, and momentum is conserved such that $k = k'$. The first three angular momentum values are summed over, and the angular distribution of the outgoing electrons is integrated over. The total cross section represents a sum over the amplitudes of all the different possible spin interactions between the precessing spin and the incoming electrons.

The scattering cross section is found to have the form seen in Figure 7.4. As the spin angle tips away from the z axis, there is no change in the total cross section. Four components contribute to the cross section, and considering the form of the spin interaction matrix they can be seen to represent the four different spin permutations such that

$$\sigma_{\text{total}} = \sigma_{\uparrow\uparrow} + \sigma_{\uparrow\downarrow} + \sigma_{\downarrow\uparrow} + \sigma_{\downarrow\downarrow} \ . \tag{7.7}$$

Examining these individual components, we find that $\sigma_{\uparrow\uparrow}$ decreases with an increasing θ, and $\sigma_{\downarrow\downarrow}$ increases with θ by the same amount. These two components are plotted in Figure

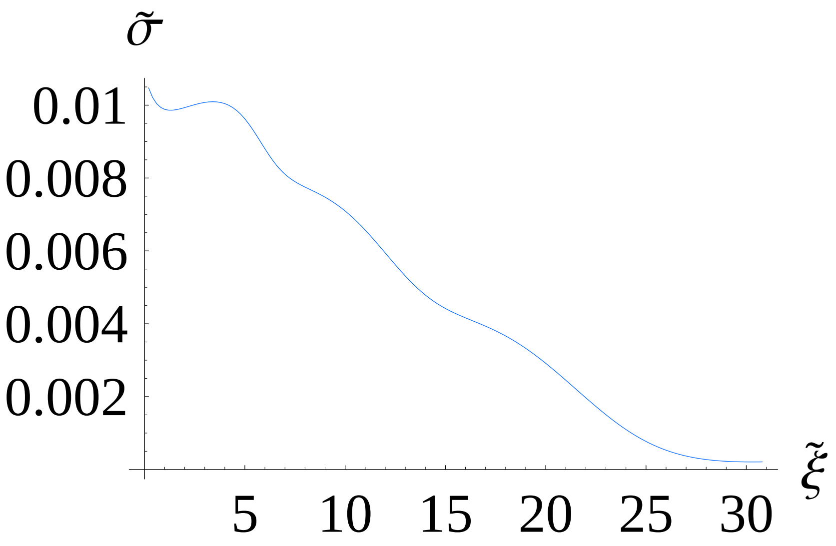

Figure 7.4: The total semi-relativistic cross section for scattering through a precessing spin. There is no change with azimuthal angle θ. Here, $\tilde{g} = 3$, $\tilde{J} = 0.3$, θ and $\phi = 0$.

7.5(a) for increasing values of θ. As the angle is increased, the two plots converge towards one another, and at $\theta = \pi/2$ the cross sections for both components are the same.

The two remaining components $\sigma_{\uparrow\downarrow}, \sigma_{\downarrow\uparrow}$ have values of $\sim 10^{-6}$, which combined with the previous two components results in a practically constant value for σ_{total} with increasing θ. There is no change in the cross section (or in any of the separate components) when the in-plane angle ϕ is changed.

The cross section for scattering appears to drop off in plateaus with increasing energy, and there is very little cross section after $\tilde{\xi} \approx 35$. There is a peak in the cross section at $\tilde{\xi} \approx 8$ which increases with increasing potential strength, as does the whole cross section (shown in Figure 7.5(b)).

7.4.3 Non-diagonalised Phase Shifts

The spin coupling matrix for the precessing spin contained the precessional nature of the impurity spin in the off-diagonal components, and a simple interaction with the z component of the precessing spin in the diagonal components. The scattering amplitude matrix elements are manipulated to enable the phase shifts to be plotted. We study

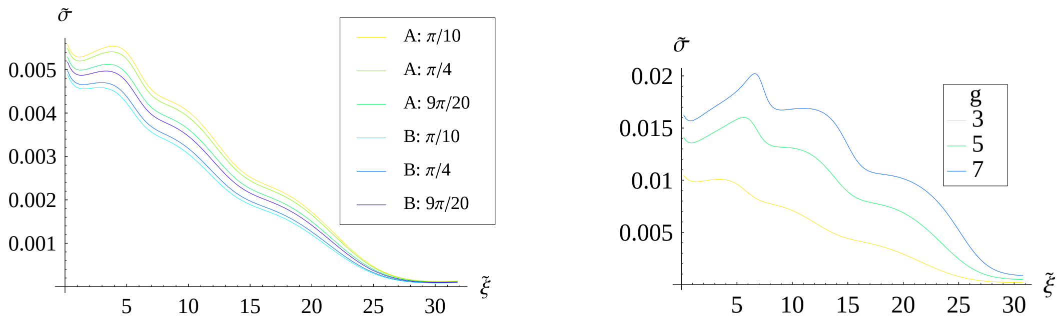

(a) Components $\sigma_{\uparrow\uparrow}$ (A), and $\sigma_{\downarrow\downarrow}$ (B) are shown to converge for increasing θ. $\tilde{g} = 3$, $\tilde{J} = 0.3$ and $\phi = 0$.

(b) The effect on the cross section when the shell potential $\tilde{g}$ is increased. $\tilde{J} = 0.3$, $\theta = \pi/6$ and $\phi = \pi/4$.

Figure 7.5: The variation in cross section components with θ, and the variation in total cross section with increasing $\tilde{g}$.

whether the nature of the precessional spin is indicated in these phase shifts.

Diagonal matrix elements

At low energies, the two diagonal elements appear to behave like the diagonal elements of the static spin phase shifts. The first element $\{1,1\}$, behaves like the scattering between two similar spins, and the $\{2,2\}$ element behaves like the scattering between two dissimilar spins. This is indicated by the conditions for a resonance at zero energy; $2l + 1 = \tilde{g} + \tilde{J}$ for $\{1,1\}$, and $2l + 1 = \tilde{g} - \tilde{J}$ for $\{2,2\}$. As we chose the precessing spin to be precessing around the positive z-axis, this suggests that element $\{1,1\}$ represents spins pointing in the $+ve$ z direction ('up' spins), and element $\{2,2\}$ represents 'down' spins. The higher energy behaviour for both of the diagonal components appears to be the same as in the static case.

When we consider the phase shifts arising from a large $\tilde{J}$ value however, the behaviour of the two diagonal entries differ widely from each other. We first concentrate on element $\{1,1\}$. When $\tilde{J} = \tilde{g}$, every part of the phase shift plot above $\delta_l = \pi/2$ is reflected downward along the $\pi/2$ line. This has the immediate effect of removing the bound state at zero energy. The plot now starts at $(\tilde{\xi}, \delta_l) = (0, 0)$. As soon as the spin interaction strength passes the value of the shell potential, a complete rotation around the $\delta_l = \pi/2$ line occurs.

If $\tilde{J}$ is further increased, the plot grows the same way as the non-magnetic plot did when increasing $\tilde{g}$, but now upside down. This behaviour is shown in Figure 7.6.

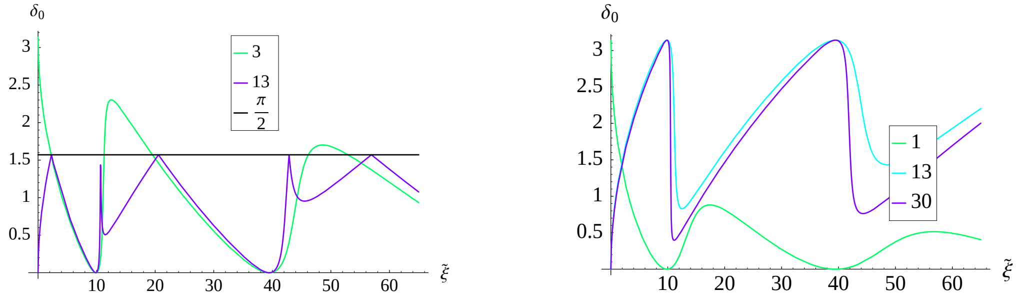

(a) $\tilde{J}$ less than and equal to $\tilde{g} = 13$. A $\pi/2$ line is plotted to aid the eye.

(b) Three $\tilde{J}$ values for $\tilde{g} = 3$.

Figure 7.6: The effect of large $\tilde{J}$ on element $\{1,1\}$. The phase shift first reflects in the $\pi/2$ axis when $\tilde{J} = \tilde{g}$, then completely rotates when $\tilde{J} > \tilde{g}$.

By contrast, the phase shifts for element $\{2,2\}$ change slowly with $\tilde{J}$, and the change is not so dramatic. As $\tilde{J}$ approaches $\tilde{g}$ from below, the whole of the phase shift spectrum reduces in amplitude, until it is practically zero (< 0.01 for $g = 3$). As the spin interaction is then increased above $\tilde{g}$, the phase shifts increase in amplitude again (Figure 7.7).

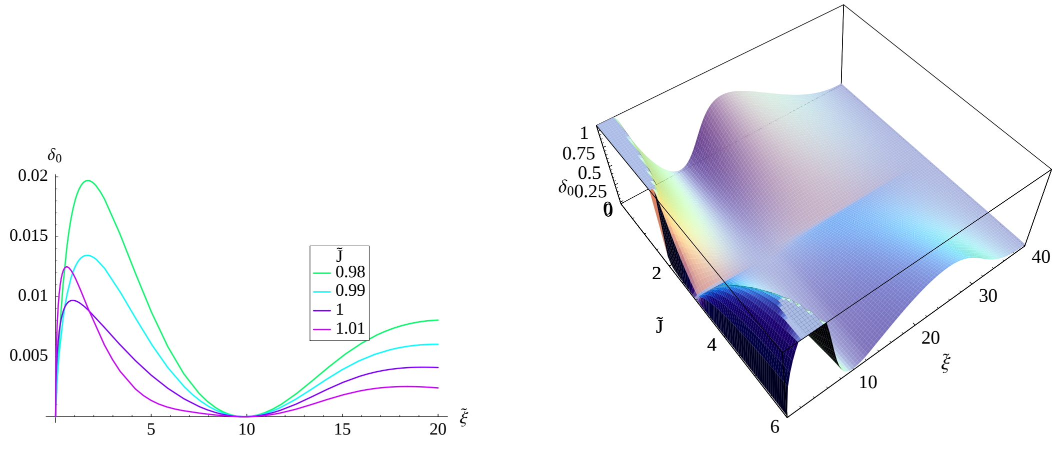

(a) $\tilde{J}$ values close to the potential strength of $\tilde{g} = 1$.

(b) Full energy spectrum showing $\tilde{J}$ values close to $\tilde{g} = 3$.

Figure 7.7: The effect of large $\tilde{J}$ on element $\{2,2\}$. When $\tilde{J}$ is the dominant potential, the phase shifts are suppressed near the value of $\tilde{g} = \tilde{J}$.

Changing the angle of precession - θ, changes the phase shifts in a small way. When θ is reduced, such that the precession is decreased, the phase shifts for the $\{1,1\}$ element (Figure 7.8(a)), are slightly raised, and the phase shifts for the $\{2,2\}$ element are slightly lowered. This was too small an effect to be seen in the scattering amplitudes plots. The phase shifts at zero energy and at the higher bound state locations are not changed by θ.

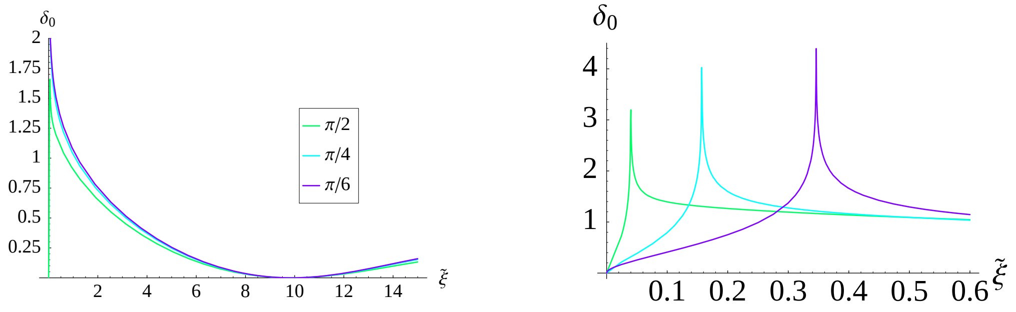

(a) Phase shifts increasing with θ for $\tilde{J} = 0.2$.

(b) The $\theta = \pi/2$ phase shifts. As $\tilde{J}$ is increased from 0.2 to 0.6, the peak moves away from the zero energy axis.

Figure 7.8: The effect of θ on the $\{1,1\}$ phase shift of the precessing spin interaction. S-wave scattering with $\tilde{g} = 1$.

When $\theta = \pi/2$, the precessing spin is completely ‘tipped over’ into the $x - y$ plane, and has no z-component. This changes the low energy behaviour of the phase shifts. Instead of the highest phase shift being at zero energy, a peak occurs instead just above $\tilde{\xi} = 0$. This can be seen in Figure 7.8(b), and is the same for both of the diagonal components.

Off-diagonal matrix elements

The phase shifts for the off-diagonal elements all have features at the usual bound state locations appropriate for each angular momentum value. However the features are not the usual jump of π, but instead are nearly-symmetrical peaks with a background value of $\delta_l = 2 - 3$ in between. This is similar to the phase shifts seen in the previous chapter when the electrons scattered from the local spin and a spin flip occurred. For moderate potential parameters, the phase shifts between the peaks are found to slightly increase with $\tilde{g}$ (Figure 7.9), and slightly decrease with $\tilde{J}$.

The phase shifts also decrease when θ is increased, again, a difference that could not

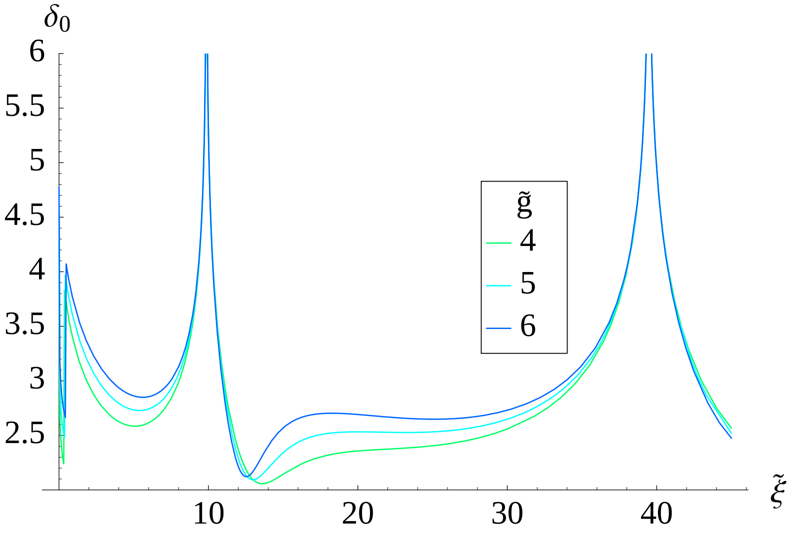

Figure 7.9: Off-diagonal phase shifts with changing $\tilde{g}$. S-wave scattering with $\tilde{J} = 0.2$.

be seen when the scattering amplitudes were plotted. When ϕ is increased, as was seen earlier, one of the off-diagonal phase shifts increases, and the other decreases by an equal amount.

When we move to large values of $\tilde{g}$ and $\tilde{J}$ the phase shifts gain features either side of the resonance peaks at the bound state energies. Large $\tilde{g}$ values introduce troughs after the main peak, with a width of about 0.4 in energy, which doesn't appear to depend on either of the potential values. For potentials when $\tilde{J} > \tilde{g}$, steps before the peaks start to form. The widths do seem to depend on $\tilde{J}$ now, increasing with $\tilde{J}$. These features are again similar to those that appeared in the static spin scattering of two spins with a spin flip, however the troughs were steps previously, and vice versa. As we did then, here we understand the troughs to be translated phase shifts of greater than π. When the potentials take on these large values, the phase shifts all move up in δ and become greater than π, although if we don't include the peaks, the total change in phase between resonances is still within the π range. This was also a feature found when describing scattering with a spin flip in the previous chapter.

We have already mentioned that the spin angle ϕ can be replaced by $\omega_L t$, and one rotation of 2π represents one precession of the impurity spin. As there is a ϕ dependence in the off-diagonal components, we can study these phase shifts as a function of the rotation of the spin. The first things to note are that there is a 2π repetition in all graphs studied, and the phase shifts mainly take on a saw-tooth shape of height π. Element $\{2,1\}$ has steps and troughs that disrupt this π range, but again, these are artefacts of the plotting method, and any jumps of 2π seen can be translated back to the range of the rest of the plot. The saw tooth pattern of $\{1,2\}$ rises instantaneously through π, then drops through π over $\phi = 2\pi$. Element $\{2,1\}$ does the opposite - the drop through π is instantaneous, and the climb is through 2π in ϕ. When $\tilde{g}$ is increased, both phase shifts move back in ϕ, the move decreasing as high values of $\tilde{g}$ are reached. The plot itself is not changed - the width and height of the pattern remains the same.

The change in $\tilde{J}$ is very explicit, and depends largely on the energy. Again, no change in height or width is seen, but $\tilde{J}$ shifts the plot a small amount to either higher or lower values of ϕ. At zero, or higher resonance energies, $\tilde{J}$ has no effect on the change of phase shift with angle. For energies at which the usual energy spectrum plot has a negative-gradient, an increased $\tilde{J}$ shifts the phase shifts to a higher angle, the shift decreasing as an energy at which the phase shifts have zero gradient is approached. When we look at an energy which is in a positive-gradient section of the graph, the phase shift is shifted backwards in ϕ for increased $\tilde{J}$, again moving back to having no effect when an energy signifying a zero gradient is reached. This behaviour occurs for all three angular momentum graphs studied.

As the changing potential values are not affecting the width or height of the general phase shift plot with ϕ, it would seem that the precession frequency is not affected by a changing $\tilde{g}$ or $\tilde{J}$, but instead, the changes in phase that occur because of the scattering are just shifted to different points on the impurity's cycle.

The remaining parameter which can change - θ, has no obvious bearing on the ϕ dependence of the phase shift, signifying that a change in precession angle does not change the rate of precession, nor has any influence on the scattering at different x-y positions.

If we want to study the total off-diagonal scattering effects, we must look at the two plots together. The phase shift behaviour displayed for one entry was opposite to the other, such that their sum would show no oscillation with the precessing angle. Each element represents one orientation of spin. It will be only for a wave that is at least partly spin-polarised that this oscillation will remain.

7.4.4 Diagonalised Phase Shifts

We can move into the frame of the precessing spin, such that the electron spin will either be parallel or anti-parallel to the impurity spin. This is done by diagonalising the s-matrix, with the two new phase shifts given by the following combination of matrix entries;

$$\delta = \frac{1}{2}\left(\{1,1\} + \{2,2\} \pm \sqrt{\{1,1\}^2 + \{2,2\}^2 - 2\{1,1\}\{2,2\} + 4\{1,2\}\{2,1\}}\right) \tag{7.8}$$

We designate the first phase shift to be the one with the square root subtracted, and the second phase shift will be the one with the square root added. The generalised phase shift from this matrix is hard to interpret. Although the behaviour when the parameters are changed are describable, there are few obvious physical interpretations of what the different features in the graphs of energy versus phase shift represent.

We first look at the zero energy behaviour of the phase shifts. Typically, this is where the first resonance would occur in the conventional phase shifts, and a relation between $\tilde{g}$ and $\tilde{J}$ values would be determined. We look at the variance of the phase shifts with potential strength, and introduce low values of the spin-interaction strength. Figure 7.10 shows the first and second phase shift for s-wave scattering. Both graphs show a vertical line representing a jump in $\pi/2$ occurring when $\tilde{g} = 1$, and $\tilde{J} = 0$. (For all angular momenta, when $\tilde{J} = 0$, there is no difference between the two diagonalised entries.) When $\tilde{J}$ is increased, a trough appears of width $2\tilde{J}$, and depth $\pi/2$ centered around the $\tilde{g} = 1$ location. The first phase shift has 'streamers' at the trough edges going down to $\delta_0 = 0$, and the second has peaks heading up to $\delta_0 = \pi$. The higher angular momentum graphs show slightly different behaviour. There is no vertical line for the $\tilde{J} = 0$ case, and the troughs that appear with an increasing $\tilde{J}$ are square-bottomed, and the same for both phase shifts i.e. there are no peaks or streamers coming from the trough edges.

When we move to the energy spectrum of the phase shifts, we see that for all three angular momenta there is one main feature at low values of $\tilde{g}$, (Figure 7.11). A background phase shift value of $\delta_l \approx 2.35$ leads to spikes which define the boundary of a trough, the base of which is at $\delta_l \approx 0.8$. The difference in height between the trough base and the background

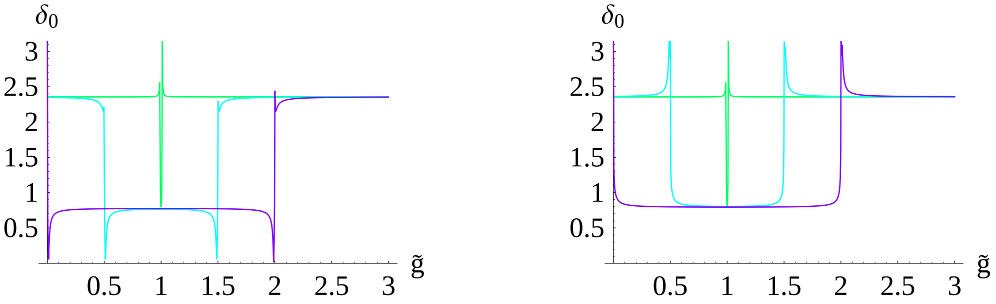

(a) The first phase shift.

(b) The second phase shift.

Figure 7.10: S-wave scattering for the diagonalised s-matrix at zero energy. Green - $\tilde{J} = 0$; blue - $\tilde{J} = 0.5$; purple - $\tilde{J} = 1$.

'tails' is equal to π for no spin interaction strength. In the $l = 0$ case, the trough cuts into the energy axis such that we only see half of the trough, which explains the vertical jump feature seen only in the $(\tilde{g}, \delta_0)$ graph.

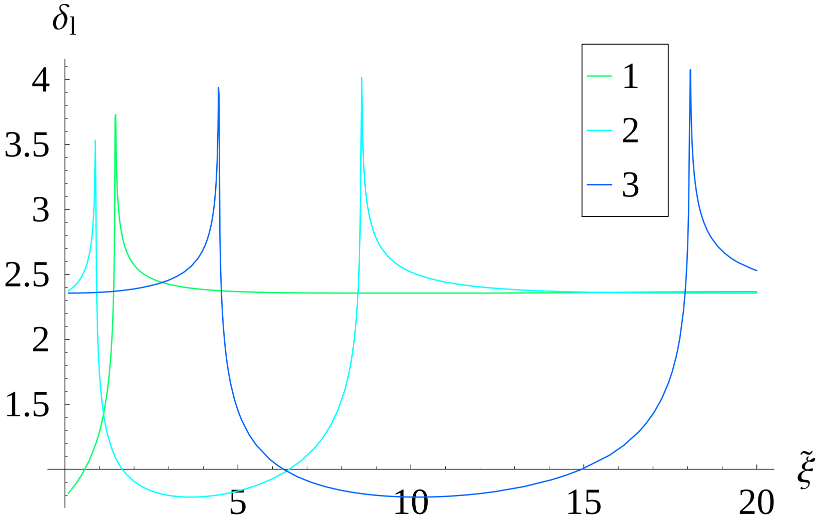

Figure 7.11: The energy features for the diagonalised s-matrix entries for all three angular momenta. $\tilde{J} = 0$, and $\tilde{g} = 2l + 1$ for each different angular momentum value.

For an increasing potential strength $\tilde{g}$, keeping $\tilde{J} = 0$ for now, the width of the trough increases. Also as $\tilde{g}$ increases, we see the trough repeated at higher energies. For low $\tilde{g}$ and $\tilde{J}$ values, there is nothing to emphasise the energies of the bound states, which occur here in the flat tails between consecutive troughs.

When we introduce a finite $\tilde{J}$, the two terms start to differ. A low $\tilde{J}$ acts to reduce the overall change in δ_l in the first phase shift, raising the base of the trough upwards, and reducing the peaks either side of the troughs. It acts in the opposite way on the second phase shift, also raising the edges of the flat background. For both phase shifts, however, as $\tilde{J} \rightarrow \tilde{g}$, the effect starts to reverse, and the phase shifts begins to increase back to its initial values for the first phase shift, and decrease for the second. When $\tilde{J}$ gets this large, the energies of the bound states now become emphasised (Figure 7.12). The phase shift can be seen forming a 'cup' shape around the point (π^2, 2.35), and it also does at the next bound state energy, ($4\pi^2$, 2.35). These are the bound state energies for s-wave scattering. The first entry shows this cup upside down, and very shallow. The second entry shows it the right way up, with edges that reach π. We can also see in this plot how $\tilde{J}$ acts to decrease the phase shift in the first phase shift, to the extent that the cup is almost not visible, and acts to increase it in the second phase shift.

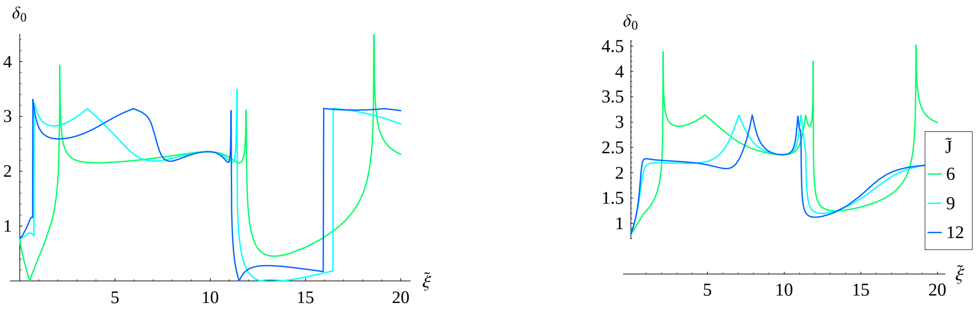

(a) The first phase shift.

(b) The second phase shift.

Figure 7.12: The effect of large $\tilde{J}$ on the diagonalised s-matrix. The plot evolves such that the remaining feature on the line $\delta_l = 2.35$ is centered on the conventional resonance energies. $l = 0$, and $\tilde{g} = 6$ in both cases.

7.5 Discussion

The phase shift energy spectrum of the diagonal components display usual resonance and bound state behaviour, with low energy behaviour exactly like that of the spin scattering seen in Chapter 6. The off-diagonal components show peaks at the resonance energies and a nearly-constant, non-zero value of δ_l in between. When the spin interaction strength is taken to zero, the phase shifts in this chapter are equal to their equivalent matrix element in the previous chapter.

The precessing spin is defined by the parameters $\tilde{J}$ and θ. When $\tilde{J}$ is increased, the amplitude of the s-matrix off-diagonal elements increases by a relatively large amount. An increased precessing angle also has the same effect. As the precessing nature of the spin was contained in the off-diagonal components of the spin-coupling matrix, this is as we would expect. As either the angle of precession or the precession strength increases, the scattering amplitude through that channel increases.

Because the diagonal components of the s-matrix were already very large with no $\tilde{J}$ interaction, the reduction in the amplitude caused by $\tilde{J}$ or θ is hardly visible. The reduction in amplitude occurs with the increase in the non-diagonal amplitudes due to the unitarity property of the s-matrix being maintained.

The effect of $\tilde{J}$ and θ on the phases are different to the effects on the amplitudes. The off-diagonal components have a reduced phase when $\tilde{J}$ or θ is increased, and the two diagonal components behave differently to one another for large $\tilde{J}$. When observing the effect of a static spin pointing in the opposite direction to the electron spin, a large value of $\tilde{J}$ changed the nature of the potential from attractive to repulsive such that no bound state could be supported. We postulated that the total potential was given by $\tilde{g} - \tilde{J}$. It appears here however, that the potential seen by element $\{2, 2\}$ never turns repulsive, and the total potential instead appears to be given by $\mid \tilde{g} - \tilde{J} \mid$. The resonances reduce in size as $\tilde{J}$ approaches $\tilde{g}$, and increases again after $\tilde{J}$ grows larger than $\tilde{g}$.

Matrix element $\{1, 1\}$ displays conventional phase shift behaviour until $\tilde{J} > \tilde{g}$. Then the phase shift profile rotates around $\pi/2$ such that it appears upside down. It is unclear why this happens, but the rotation still results in the phase shift passing through $\pi/2$, and for high potentials results in jumps in π signifying a bound state. It just all happens upside down. The phase shift profile is recognizable, so we conclude it is still a valid representation of where the resonances and bound states occur in energy.

On top of this behaviour, the $\{1, 1\}$ phase is reduced slightly with increasing θ, and the $\{2, 2\}$ elements are increased slightly. This change due to θ is much smaller than the effect due to $\tilde{J}$. If we remember that the phase shifts represent how much the incoming wave has been changed by the potential, this result suggests that the precessing spin must act to reduce the scatter of the up spins, and increase the scattering of the down spins. As a precessing spin results in the spin axis *not* pointing directly in the 'up' direction, this is to be expected.

We saw that for a particular energy, an increased potential strength reduced the off-diagonal scattering amplitude (in the first anti-clockwise loop). We must assume that even though it isn't visible, this is accompanied by a small increase in the scattering amplitude of the diagonal entries. The phase shift however, of both types of entries increase with an increased $\tilde{g}$, as could be seen in the phase shift plots. The secondary loops in the scattering amplitude plots showed the behaviour between resonance energies. The scattering amplitudes would move clockwise, then anti-clockwise before returning to the resonance point, signifying a change in phase first in one direction, then in the other. For the diagonal plots, this explains why the primary loop moved in a clockwise direction with energy for values of $\tilde{g} < 2l + 1$. Conventionally, before that value of potential was reached, the phase shift plot would start at $(\tilde{\xi}, \delta) = (0, 0)$, resulting in a small area of positive gradient before the large negative gradient is observed starting at $(\pi, 0)$.

The real and imaginary parts of the diagonal scattering amplitudes appear to be out of phase with each other by π. This results in a circular parametric plot around the origin. The off-diagonal imaginary part appears to lag by $\pi/2$, but is also stretched asymmetrically, which we see as a shape almost representing a kidney bean. This extra imaginary component appears due to the precessing spin in the off-diagonal spin interaction matrix. The entries in this matrix also explain the different starting points of the parametric plots. The diagonal terms are described by $\cos\theta$, which is purely real, and for low θ result in the parametric plot starting close to $(1, 0)$. The off-diagonal terms are given by $\sin\theta \exp(\pm i\phi) = \sin\theta\cos\theta \pm \sin^2\theta$. The parametric plot will start near $(0, 0)$ for low θ.

The off-diagonal phase shifts did not display typical resonance and bound state behaviour. The same problem arises that occurred with the static spin scattering behaviour. It is unclear how to interpret the large peaks seen at the bound state energies, and the non-zero background phase shift. It is for this case that we can see the importance of the parametric scattering amplitude plots. It is there that we can see the resonance behaviour of the electrons, and the effect of the potentials on this entry.

In this model, symmetry is only broken in the z direction. This means that there is no reason why one direction in the $x-y$ plane should be preferred over another. This is borne out in the scattering cross section graphs where there is no dependance on the precessional angle ϕ. The apparent constancy with changing θ is explained by examining the separate contributions to the total cross section. As mentioned above, the precessing spin appears to reduce the scatter of the 'up' spins, and increase the scatter of the 'down' spins. These changes are equal, resulting in no overall change in the cross section with θ. This is the case for an equal amount of up spins and down spins.

It was found in Chapter 3 that just by passing through a magnetic field, there will be a polarisation equal to 1 in 50,000 spins (for the magnetic field sizes used in the Durkan experiment). To investigate this, a polarisation was entered such that there was a small surplus of up spins over down spins. However this polarisation was too small to notice any change in the cross section with azimuthal angle. The largest change in cross section was $\sim 1 \times 10^{-9}$, which is negligible when compared to the size of the actual cross section signal (~ 0.01).

To determine the size of the spin-orbit coupling effect on the scattering cross section, the fully non-relativistic limit can be taken and compared to the semi-relativistic limit presented above. This limit is taken by taking $c \to \infty$, meaning that all entries multiplied by D in the semi-relativistic t-matrix go to 0 leaving no terms with $\bar{l}$ in. This gives a t-matrix of

$$\begin{aligned} t_{\mathrm{NR}}(\boldsymbol{k'}, \boldsymbol{k}; \tilde{\xi}) &= \sum_{s} \sum_{l m_l} (-) \frac{a}{\pi} j_l(k'a) j_l(ka) Y_l^{m_l}(\hat{\boldsymbol{k}}') Y_l^{*m_l}(\hat{\boldsymbol{k}}) \\ &\times \left[1 - \frac{a}{\pi} \sqrt{\tilde{\xi}} \left(\tilde{g} + \tilde{J} \boldsymbol{S} \cdot \boldsymbol{\sigma} \right) \left(j_l(ka) n_l(ka) - i j_l^2(ka) \right) \right]^{-1} \\ &\times \left(\tilde{g} + \tilde{J} \boldsymbol{S} \cdot \boldsymbol{\sigma} \right) \end{aligned}$$

The resulting cross section for an azimuthal angle of $\pi/6$, a precessional angle of 0, a shell potential strength of 3 and a spin interaction strength of 0.3 can be seen along with the equivalent semi-relativistic one in Figure 7.13.

The non-relativistic limit gives a slightly smaller cross section than the semi-relativistic

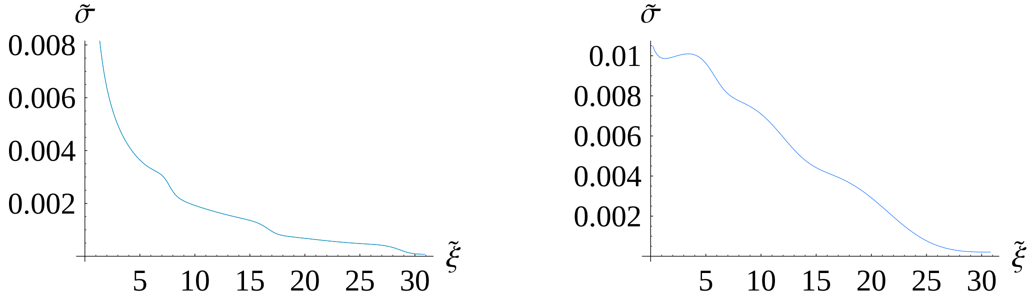

(a) The non-relativistic cross section.

(b) The semi-relativistic cross section.

Figure 7.13: A comparison of the non-relativistic and the semi-relativistic cross sections for scattering from a precessing spin.

limit showing that the spin-orbit coupling acts to increase the overall scattering cross section, and it is therefore important to include this effect.

The cross section is a sum over the first three angular momentum values which may explain the energy distribution seen. The two plateaus seen in the graphs reflect the location of the resonance states seen in the phase shift plots of the individual angular momentum values. Their location changes with $\tilde{g}$, and they become more defined and last for a wider energy range as $\tilde{g}$ is increased. For a very large potential strength, when the resonance states are quite large, the cross section is a smooth curve, interspersed with peaks at the energies of the resonant (and bound) states (Figure 7.14). This signifies an increase in scattering due to the presence of resonance states, which is seen for many other systems, for example in the nucleon cross section [89]. It is also expected that the cross section will decrease with increasing electron energy as the higher the energy, the less effect the potential will have on the incoming electrons. This effect is shown clearly in all of the graphs shown here.

The diagonalised phase shifts practically lose the typical resonance behaviour that was seen in the diagonal s-matrix entries. The larger features on the diagonalised entries appear at energies just higher than the resonance energies, and seem to have their origin in the troughs that appear in the off-diagonal entries for large $\tilde{g}$ values. As an indicator of the scattering that occurs as a result of a precessing spin, the diagonalised phase shifts seem to confuse rather than clarify.

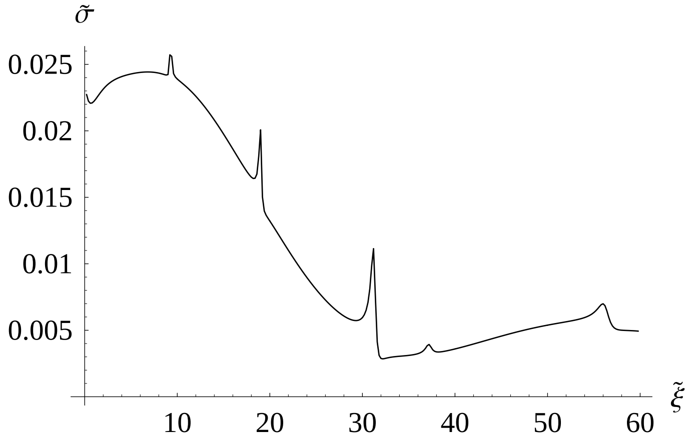

Figure 7.14: The cross section for scattering from a precessing spin with a strong potential ($\tilde{g} = 50$)

7.6 Conclusions

The elements of the s-matrix for a precessing spin interaction display three different types of behaviour:

Matrix element $\{1, 1\}$

For moderate values of energy and potential strengths, this element behaved as though is was a static 'up' spin interacting with the z component of the precessing spin. As the spin interaction strength was increased, the scattering amplitude through this, and the other diagonal channel decreased. This element shows increased phase shifts with $\tilde{J}$, the electrons being scattered by a greater amount. However as the angle of precession increased, the scattering effect was reduced.

Matrix element $\{2, 2\}$

This element behaved like a 'down' spin, its low energy behaviour mimicking that of the scattering between two opposite spins in Chapter 6. The scattering amplitude decreased with increased $\tilde{J}$, as did the phase, the phase shift becoming negligible when $\tilde{J} = \tilde{g}$. It was found that increasing the angle of precession caused higher phase shifts in this case, the scattering effect being enhanced for spins in the opposite direction to the axis of precession.

Off-Diagonal matrix elements

As was expected, the scattering amplitude for both of the off-diagonal elements increased as the spin interaction and the angle of precession was increased. There appears to be no conventional resonances in this scattering profile, the scattering amplitude going to zero when the other scattering channel had a maximum effect. The potential and spin interaction strengths appear to have no effect on the time dependence of the phase shifts, but appear to affect the point in the impurity cycle at which phase shift jumps occur. When both the off-diagonal elements are taken together, the time dependency cancels out leaving no dependency on the precessional angle for an unpolarised wave.

The Total Cross Section

This quantity was calculated to mimic the experimental observable, in that all of the different spin components were observed as one total value. In the semi-relativistic limit there was no dependance on the precessional angle of the spin, and although separate components showed a change with the azimuthal angle θ, the total cross section was constant with this change. The addition of a polarisation expected to arise from the electrons passing through a magnetic field showed only a negligible effect on the cross section when changing θ.

The energy dependance of the cross section arose from the angular momenta that had been summed over, and local increases in cross section were attributed to the presence of resonant states of the target potential.

A comparison with the non-relativistic limit showed that the spin-orbit coupling arising in the semi-relativistic limit does have a significant contribution to the overall cross section, so it is important to include this effect in further cross section calculations.

Chapter 8

Two Potential Scattering

The previous chapters have looked at electrons scattering from either the tip potential alone, or the atom potential alone. Here, we consider the combined effect of the two potentials on incoming electrons. This approach is a closer representation of the Durkan experiment in which the current is affected by both potentials. As discussed in Chapter 7, the total cross section for scattering is a better indicator of experimentally observable quantities than the phase shifts of the individual scattering channels, so this is calculated here using the first order approximation (the Born approximation), to the transition matrix.

8.1 The Two Potential Construction

The combined potential of the tip and the molecule atom on the surface is given by

$$V(\boldsymbol{r}) = -g_t\,\delta(\mid \boldsymbol{r} \mid -a) - (g_a + J\boldsymbol{S}\cdot\boldsymbol{\sigma})\,\delta(\mid \boldsymbol{r} - \boldsymbol{t_a} \mid -a)\ , \tag{8.1}$$

and is shown schematically in Figure 8.1.

The molecule atom is shifted in space from the tip atom by an amount $\boldsymbol{t_a} = (0, 0, t_a)$, such that t_a represents the width of the gap between the STM tip and the surface, and the condition $t_a > a$ holds as it does experimentally.

The potential is moved into the momentum space representation by taking the Fourier Transform over the spatial coordinate $\boldsymbol{r}$. To incorporate the spin-orbit coupling of the

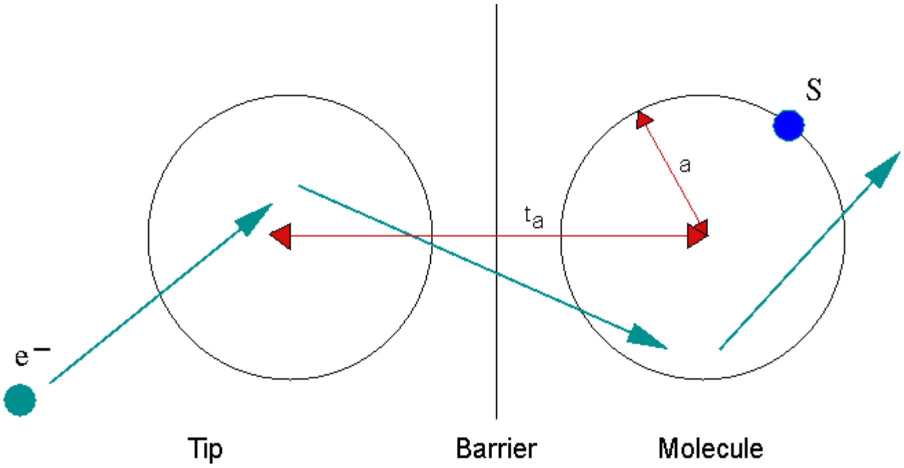

Figure 8.1: The combined potential shells. The potential representing the deposited molecule is t_a away from the center of the tip potential. The radius of both potentials is given by a. The blue lines show a typical electron route.

incoming electrons the equation is formulated relativistically and the semi-relativistic limit is taken. The molecule potential is written in terms of $\mid \boldsymbol{r} - \boldsymbol{t_a} \mid$ rather than $\boldsymbol{r}$ however, so must be converted by first writing $R = \mid \boldsymbol{r} - \boldsymbol{t_a} \mid$, extracting the part constant with R, then replacing R with r to obtain the same basis as that of the tip potential;

$$\begin{aligned} V(\boldsymbol{k'};\boldsymbol{k})_{\text{molecule}} &\propto \int \delta(\mid \boldsymbol{r} - \boldsymbol{t_a} \mid - a) \exp\left[i(\boldsymbol{k'} - \boldsymbol{k}) \cdot \boldsymbol{r}\right] d^3 r \\ &\propto \int \delta(R - a) \exp\left[i(\boldsymbol{k'} - \boldsymbol{k}) \cdot (\boldsymbol{R} + \boldsymbol{t_a})\right] d^3 R \\ &\propto \exp\left[i(\boldsymbol{k'} - \boldsymbol{k}) \cdot \boldsymbol{t_a}\right] \int \delta(R - a) \exp\left[i(\boldsymbol{k'} - \boldsymbol{k}) \cdot \boldsymbol{R}\right] d^3 R \\ &\propto \exp\left[i(\boldsymbol{k'} - \boldsymbol{k}) \cdot \boldsymbol{t_a}\right] \int \delta(r - a) \exp\left[i(\boldsymbol{k'} - \boldsymbol{k}) \cdot \boldsymbol{r}\right] d^3 r \ . \end{aligned} \tag{8.2}$$

The complete potential can then be written as

$$V(\boldsymbol{k'};\boldsymbol{k}) = \frac{1}{(2\pi)^3} \left(-g_t - (g_a + J\boldsymbol{S} \cdot \boldsymbol{\sigma}) \exp\left[i(\boldsymbol{k'} - \boldsymbol{k}) \cdot \boldsymbol{t_a}\right]\right) \int \delta(r - a) \exp\left[i(\boldsymbol{k'} - \boldsymbol{k}) \cdot \boldsymbol{r}\right] d^3 r \tag{8.3}$$

The relativistic expansion of a plane wave (first reproduced in Chapter 5) is applied to both exponential functions in the potential. The molecule potential is consequentially multiplied by

$$(-)\frac{2}{\pi}\frac{W+mc^2}{2W}\sum_{s''}\sum_{\kappa\mu}\sum_{\kappa'\mu'}Y_{l'}^{*\mu'-s''}(\hat{\boldsymbol{k}}')Y_{l}^{\mu-s''}(\hat{\boldsymbol{k}})C(l\tfrac{1}{2}j;\mu-s'',s'')C(l'\tfrac{1}{2}j';\mu'-s'',s'')$$
$$\times\, i^{l'-l}\begin{pmatrix} j_{l'}(k't_a)\chi_{\kappa'}^{\mu'}(\hat{\boldsymbol{t}}_{\boldsymbol{a}}) \\ iD'j_{\overline{l'}}(k't_a)\chi_{-\kappa'}^{\mu'}(\hat{\boldsymbol{t}}_{\boldsymbol{a}}) \end{pmatrix}\begin{pmatrix} j_l(kt_a)\chi_{\kappa}^{\dagger\mu}(\hat{\boldsymbol{t}}_{\boldsymbol{a}}) & -iDj_{\bar{l}}(kt_a)\chi_{-\kappa}^{\dagger\mu}(\hat{\boldsymbol{t}}_{\boldsymbol{a}}) \end{pmatrix}. \tag{8.4}$$

This expansion has separate κ, μ and s dependence from the expansion inside the d^3r integral. The Spin Angular functions are expanded out over s and s', and the argument of the Spin Angular functions $\hat{\boldsymbol{t}}_{\boldsymbol{a}}$ equates to $(\theta,\phi)=(0,0)$ from our choice of direction for $\boldsymbol{t}_{\boldsymbol{a}}$. This results in the whole expression going to 0 except when $\mu-s$ or $\mu'-s'=0$. In the semi-relativistic limit $(W+mc^2)/2W\to 1$ and $DD'\to 0$ simplifying the expression further.

Within the integral the d^3r integral is carried out and in the semi-relativistic limit gives

$$\sum_{s}\sum_{\kappa\mu}(4\pi a)^2\begin{pmatrix} j_l(ka)j_l(k'a)\chi_{\kappa}^{\mu}(\hat{\boldsymbol{k}}')\chi_{\kappa}^{\dagger\mu}(\hat{\boldsymbol{k}}) & -iDj_l(ka)j_{\bar{l}}(k'a)\chi_{\kappa}^{\mu}(\hat{\boldsymbol{k}}')\chi_{-\kappa}^{\dagger\mu}(\hat{\boldsymbol{k}}) \\ iD'j_{\bar{l}}(ka)j_l(k'a)\chi_{-\kappa}^{\mu}(\hat{\boldsymbol{k}}')\chi_{\kappa}^{\dagger\mu}(\hat{\boldsymbol{k}}) & 0 \end{pmatrix}. \tag{8.5}$$

These two expressions are combined with the shell and spin potentials, and the first three angular momentum values are summed over. The scattering cross section is found as in Chapter 7, only here, the t-matrix is calculated to the Born approximation ($t(\boldsymbol{k}';\boldsymbol{k})=V(\boldsymbol{k}';\boldsymbol{k})$) only. The cross section is then given by

$$\sigma=\frac{m^2L^6}{4\pi^2\hbar^4}\int\mid V(\boldsymbol{k}',\boldsymbol{k})\mid^2\,\mathrm{d}\Omega\ . \tag{8.6}$$

This approach was taken as the potential is more complex than in previous chapters.

8.2 Results

The cross section for scattering through a bare shell and a shell with a spin behaves similarly to that of the cross section through a single shell with a spin. There is no change in the total cross section when the azimuthal angle of the precessing spin is changed, but as before, if the cross section is decomposed into its separate entries it is seen that this is because one entry increases with increasing angle, and the other entry decreases by the same amount.

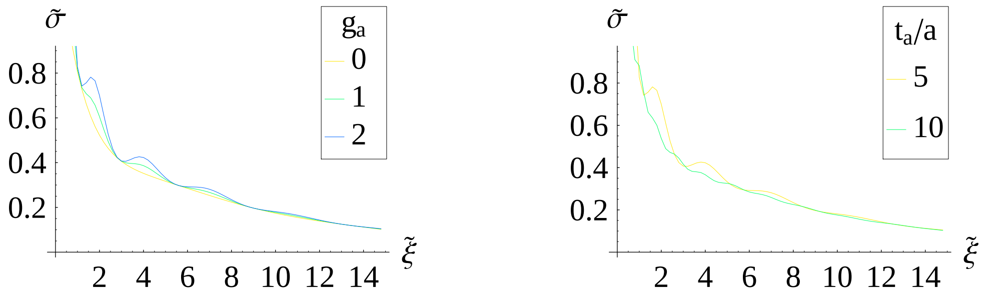

(a) The atom potential $\tilde{g}_a$ is increased for a constant $\tilde{g}_t = 3$ and $\tilde{J} = 0.3$.

(b) The distance between the potentials is increased. t_a/a is the ratio of the potential separation to the shell radius.

Figure 8.2: Changes in the total scattering cross section as the parameters governing the location and the strength of the two potentials are changed.

The cross section appears constant with precessing angle ϕ, and here neither decomposed entry changes with increasing angle. Increasing $\tilde{g}_t$ or $\tilde{J}$ increased the cross section slightly in the same manner as when considering the spin alone, however oscillations are observed (see Figure 8.2(a)) when $\tilde{g}_a$ is increased. These oscillations arise from interference between the two potentials, and decrease as the distance between the potential (given by the ratio t_a/a) increases (Figure 8.2(b)).

The general shape of the cross section for both shells is compared to that of one shell only in Figure 8.3. The overall size of the cross sections differ which will be due to two potentials being present to scatter from. A difference is also expected due to the two-shell cross section being calculated to first order only; the Born approximation tends to over estimate the cross section [90].

Figure 8.3 shows the lack of variance with the azimuthal angle for both cases, and both graphs reduce to negligible cross section just before $\tilde{\xi} = 30$. The plateaus seen in the previous chapters can be discerned at approximately $\tilde{\xi} = 15$ in both graphs, and the one seen near $\tilde{\xi} = 6$ on the single-shell cross section is at the same location as an interference plateau on the two-shell cross section.

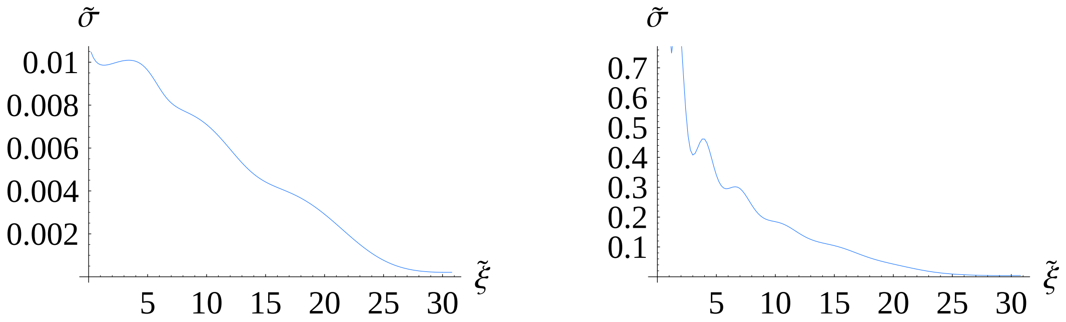

(a) The full t-matrix calculation of the molecule potential alone.

(b) The Born approximation of the molecule and the tip potential.

Figure 8.3: A comparison of the cross section for the molecule alone, and the molecule with the tip. There is seen to be no dependence on θ for both cases.

8.3 Discussion and Conclusions

As seen by the much larger two-shell cross section, the precessing spin affects the overall cross section in a much smaller way than the bare shell representing the tip potential. It is however, unclear how much of this difference is due to the two-shell cross section being calculated to first order only. For that reason, it is wise to only draw conclusions about the change in shape caused by the inclusion of the second potential.

Concentrating on the shape of the energy spectrum, we have found that an extra scattering centre and the location of this impurity affects the energy signature by increasing the cross section at particular energies in a typical interference pattern. This is in contrast to findings by Granot in Ref. [28]. There, the transmission through a 2D wire was found to *not* be affected by an impurity inside that wire, and for weak scattering, the scattering pattern near the threshold energy was not even dependant on the location of the impurity.

The oscillations in the cross section (due to cross terms from having two potentials), are increased by bringing the potentials closer together, or by increasing the strength of the potentials. It is suggested therefore, that to estimate the effect of the second potential and to also allow for the Born approximation used in this chapter, that it is sufficient to compare the graphs obtained above to the graph obtained when $\tilde{g}_a$ is set to 0.

An example of this is seen in Figure 8.2(a), where it is clear that the cross terms contribute significantly to the energy spectrum and that their effect decreases at higher energies.

When trying to observe this effect, it must be noted that at particular energies no changes occur with the introduction of a second potential, and observing at more than one energy is recommended.

This model then appears to show that for the simple potentials used here, the presence of the second potential is probably more important than the nature of the second potential.

It is important to consider if this calculation of the cross section for scattering through both potentials offers an explanation of why the current or conductance through both potentials was found to oscillate in the Durkan experiment. When a voltage is applied across a system, the cross section at the Fermi energy is directly proportional to the conductance through that system. It can be assumed then, that any variation in the conductance will be seen in the cross section, and for this model, the cross section is sufficient to describe movement of electrons under the influence of the two potentials.

It has already been described above that there is no variation in the cross section with the parameters of the precessing spin. This, combined with the fact that we have presented only a very basic model of a tip potential, suggests that no variation will be seen in the conductance either. We can conclude from this that this model has been insufficient to describe the outcome of the Durkan experiment.

Chapter 9

Conclusions

This thesis was motivated by the detection of the precessional nature of a local electron spin in a steady magnetic field inside a tunnel junction.
There were two questions posed in Chapter 2 which we set out to address:

1. If the local spin is precessing, under what mechanism is it doing so (knowing that it is expected to be pointing in the equilibrium magnetisation direction)?
2. Assuming the local spin *is* precessing, how does this motion project itself into the tunnelling current spectrum?

In Chapter 3 we examined whether electrons travelling through a tunnel junction could be affected by the presence of the local magnetic field. Specifically, could they become polarised in the time it took to cross the tunnel junction? This was shown to be the case using a technique of matching waves at the edges of the tunnel junction, assuming the electrons approached the junction as a plain wave. The resulting polarisation when using the parameters used in the Durkan experiment [29], was a spin polarisation of 1 in 50,000. However, this polarisation is steady in time so doesn't offer an explanation for why the local spin should be precessing. This model also doesn't include the local spin inside the tunnel junction.
In Ref. [40], Drakova says

> *A major problem of the perturbation approaches to STM is the neglect of tip-sample interaction and scattering of the injected electron by the localized tip*

> *potential and the potential in the sample or in the tip, depending upon the polarity chosen for electron injection.*

In Chapters 4-7 we attempt to address this problem with the study of a Delta Shell potential in a scattering framework. By operating in momentum space, with such a simple potential, there is no need to match wavefunctions at potential boundaries, and the problem proves to be exactly solvable.

We follow on from work by Villarroel in Ref. [75], and extend the study from bound states to scattering states. We achieve the same phase shifts as Gottfried in Ref. [68], who used wave-matching techniques in coordinate space. We also obtain analytic expressions determining the energies of resonance and bound states for an electron of a general angular momentum value.

In Chapter 5 we used the Delta Shell potential in a semi-relativistic framework to include the spin of the incoming electrons. A semi-relativistic limit was considered sufficient as the energies we were interested in were low, but the spin-orbit coupling is retained in this regime. The phase shifts were macroscopically the same as the non-relativistic ones, and a splitting in the energy between spin-orbit split states was found of $\sim 10 \times 10^{-4}$ eV. This size, along with the size difference between the s- and p-wave bound states, reproduces the spin levels observed in the Hydrogen atom.

In Chapters 6 and 7 the Delta Shell potential was modified by the addition of a local spin interaction to model the interaction between the electron spin and the local spin on the molecule deposited in the tunnel junction.

We found that there were three scattering scenarios. The electron spin could be in the same direction as the local spin, the electron spin could point in the opposite direction to the local spin, or the electron spin could be opposite to the local spin *and* a spin flip could occur during the scattering process. The first two scenarios changed the phase shift profiles such that the total potential was found to be dependent on either the sum (for same spins) or the difference (for opposite spins) of the shell potential, and the spin interaction strength $\tilde{J}$.

The spin-flip scattering was found to completely change the phase shift behaviour, in such a way that they could no longer be interpreted in terms of resonances, scattering and bound states. This area of interest invites further study, as we were unable to fully characterise the behaviour as a function of energy.

So far, no time-dependent artefacts have arisen from our examination of the scattering states so we conclude that we have been unable to show *why* the local spin is precessng. Chapter 7 introduces a time-dependent spin such that we can address the second question posed; that of how a precessing spin manifests itself in a tunnelling current passing through that spin. The precessing spin dependance was located in the off-diagonal elements of the s-matrix such that when they were considered together (constituting an unpolarised electron wave), no spin dependance was noticed. A completely spin-polarised electron wave did show a repetition in the phase shifts at a frequency equal to the Larmor frequency of the precessing spin, however this situation was not expected of the experiment we were trying to model.

It was decided to calculate the total cross section for scattering through all of the available spin channels (same spins or opposite, with or without a spin flip). This was postulated to be a more accurate representation of what could be detected experimentally. The first three angular momentum states were summed over, and the scattering cross section was found to be constant with both the precessional angle, and the azimuthal angle. It was expected that the precessional angle should not affect the total cross section, as the model was set up to be symmetric around the direction of precession (as is the case experimentally). The lack of dependence on the azimuthal angle was found to occur because for one orientation of spin, an increased angle increased the cross section, and for the other orientation it decreased the cross section. These two effects canceled out, leaving no dependence on the angle.

If the current was slightly spin polarised, to the size found in Chapter 3, there was found to be no discernable change in the cross section, a difference of only 1×10^{-9} being found when increasing the azimuthal angle.

It was also found in this chapter that the cross section was affected significantly by the inclusion of spin-orbit coupling, and that it was therefore necessary to include this effect when studying the scattering cross section.

In Chapter 8 the potentials of the STM tip and the local electron spin were summed together, and the cross section for scattering through both potentials was found using a first order approximation to the t-matrix. This was done to determine the effect of the second potential on the cross section, and it was found that the main effect was due to the cross terms which arose from between the two potentials. These resulted in local increases in cross section across the energy spectrum, and emphasised the importance of including all potentials in the calculation.

To take this calculation further it would be necessary to calculate the full t-matrix for the two combined potentials. However the lack of appreciable spin dependance in both the azimuthal and the precessional spin angle when the spin is treated on its own, suggests that this is unlikely to result in any further clarification of the problem. Interference between the two potentials does affect the likelihood of scattering, but as there is very little angular dependance, this would be fixed in time, again leading to no dynamic change in the measured quantities.

We can therefore conclude that for an unpolarised current, this model, which includes spin orbit coupling, is insufficient to describe the Durkan experiment. If a polarised current was present, this model hints at why an oscillating current may be seen after tunnelling into a precessing spin, but further exploration is required to examine the parameters that determine the size of this effect.

Although this approach has not answered the question of why a single precessing spin should affect the temporal characteristics of an electron current passing through it, it has explored the bound states and scattering states of a Delta Shell model. It has examined to some degree the effect of a static and precessing local spin on these states, and has started an analytic investigation into the importance of interference between multiple potentials.

Appendix A

Quantum Mechanical Resonance

To describe what happens in the resonant condition, we switch to a quantum mechanical description of a precessing spin. The spinor notation for a spin $\boldsymbol{S} = 1/2$ is given by

$$\begin{aligned} S_z \mid \alpha\rangle &= +1/2 \mid \alpha\rangle \qquad & S^2 \mid \alpha\rangle &= 1/2(1/2+1) \mid \alpha\rangle \\ S_z \mid \beta\rangle &= -1/2 \mid \beta\rangle \qquad & S^2 \mid \beta\rangle &= 1/2(1/2+1) \mid \beta\rangle \end{aligned}$$

where $\mid \alpha\rangle$ describes the spin up state and $\mid \beta\rangle$ describes the spin down state. The x and y spin operators act on the eigenfunctions of S_z as below

$$\begin{aligned} S_x \mid \alpha\rangle &= +1/2 \mid \beta\rangle \qquad & S_x \mid \beta\rangle &= +1/2 \mid \alpha\rangle \\ S_y \mid \alpha\rangle &= +i/2 \mid \beta\rangle \qquad & S_y \mid \beta\rangle &= -i/2 \mid \alpha\rangle \ . \end{aligned}$$

When an oscillating field B_1 is applied perpendicular to a steady magnetic field B_0, the spins in the system experience a magnetic field given by the vector sum of the two fields.

$$B = B_1 \left[\hat{\imath} \cos(\omega_1 t) + \hat{\jmath} \sin(\omega_1 t) \right] + B_0 \ \hat{k} \tag{A.1}$$

The time-dependent Schrödinger equation is given by

$$i\hbar \frac{\delta \, \Psi(t)}{\delta t} = \mathcal{H}\Psi(t) \ , \tag{A.2}$$

where $\mathcal{H}$, the energy, is given by

$$\mathcal{H} = g_e \mu_B \boldsymbol{S} \cdot \boldsymbol{B} \tag{A.3}$$

for an electron in a magnetic field.

An electron with $g_e = 2$ will therefore be described by

$$\mathcal{H} = 2\mu_B B_1 \left[S_x \cos(\omega_1 t) + S_y \sin(\omega_1 t)\right] + 2\mu_B B_0 S_z \ . \tag{A.4}$$

For a steady magnetic field only, we know there are two energy levels of the system; $E_\alpha = \mu_B B_0$ and $E_\beta = -\mu_B B_0$. The addition of B_1 means that transitions can take place between them and we can write the solution to Equation A.2 with our particular $\mathcal{H}$, as a sum of the two eigenfunctions associated with these levels;

$$\Psi = C'_\alpha \mid \alpha \rangle + C'_\beta \mid \beta \rangle \tag{A.5}$$

The wavefunctions must be separable into time and space components, and the final solution is proposed to be a linear combination of the two wavefunctions

$$\Psi = C_\alpha \Psi_\alpha + C_\beta \Psi_\beta \tag{A.6}$$

with

$$\Psi_\alpha = \mid \alpha \rangle \exp\left(-i/\hbar E_\alpha t\right) \quad \text{and} \quad \Psi_\beta = \mid \beta \rangle \exp\left(-i/\hbar E_\beta t\right)$$

Differentiating Equation A.2 with these entries gives

$$\begin{aligned} \mathcal{H}(C_\alpha \Psi_\alpha + C_\beta \Psi_\beta) &= \frac{i}{\hbar}\left(C_\alpha \frac{d}{dt}\Psi_\alpha + C_\beta \frac{d}{dt}\Psi_\beta + \frac{d}{dt}(C_\alpha)\Psi_\alpha + \frac{d}{dt}(C_\beta)\Psi_\beta\right) \\ &= \mathcal{H}_0(C_\alpha \Psi_\alpha + C_\beta \Psi_\beta) + \mathcal{H}'(C_\alpha \Psi_\alpha + C_\beta \Psi_\beta) \ . \end{aligned} \tag{A.7}$$

The steady state solution of $\mathcal{H}_0 = 2\mu_B B_0 S_z$ is already known. We can manipulate the second term on the right hand side (the pertubed term), to get two coupled differential equations:

$$\begin{aligned} \frac{d\,C_\alpha}{dt} &= \frac{C_\beta}{i\hbar}\mu_B B_1 \exp\left(-i\omega_1 t\right) \exp\left(-i/\hbar(E_\beta - E_\alpha)t\right) \\ \frac{d\,C_\beta}{dt} &= \frac{C_\alpha}{i\hbar}\mu_B B_1 \exp\left(i\omega_1 t\right) \exp\left(-i/\hbar(E_\alpha - E_\beta)t\right) \end{aligned} \tag{A.8}$$

B_1 is defined to be much smaller than B_0, so we can use perturbation theory to solve these equations. At $t = 0$, the system is in the lowest energy state and is described by Ψ_β (spin down), so $C_\beta = 1$. We integrate (A.8) over t, using the fact that $E_\beta - E_\alpha = -2\mu_B B_0$.

$$C_\alpha = \frac{\mu_B B_1}{i\hbar} \frac{\exp\left(i\left(\frac{2\mu_B B_0}{\hbar} - \omega_1\right)t\right) - 1}{\left(\frac{2i\mu_B B_0}{\hbar} - i\omega_1\right)} \tag{A.9}$$

The probability of finding the system in the state α (spin up) at time t is given by $C_\alpha^* C_\alpha$;

$$C_\alpha^* C_\alpha = \frac{4\mu_B^2 B_1^2}{\hbar^2} \frac{\sin^2\left(\frac{1}{2}(2\mu_B B_0 t/\hbar - \omega_1 t)\right)}{(2\mu_B B_0 t/\hbar - \omega_1 t)^2} \tag{A.10}$$

Appendix B

Atomic Units

When evaluating the polarisation of an electron wave as it moves through a magnetic field, we moved into Atomic Units. We use Hartree Atomic Units which are very closely linked to Atomic Rydberg Units. In Atomic Hartree Units, constants are redefined such that

$$\frac{e^2}{4\pi\epsilon_0} = \hbar = m = 1 \tag{B.1}$$

The speed of light is calculated from the fine structure constant, which retains its value of 1/137.

$$\alpha = \frac{e^2}{4\pi\epsilon_0\hbar c} \approx \frac{1}{137} \ \rightarrow c \approx 137 \tag{B.2}$$

The Hartree energy unit is twice that of the Rydberg unit

$$E_{ht} = \frac{\hbar^2}{m_e a_0^2} \ , \tag{B.3}$$

with a_0 being the Bohr Radius given by

$$\frac{h^2}{4\pi^2 m e^2} \ . \tag{B.4}$$

The Bohr radius and the Hartree have the numerical values

$$1\text{Bohr} = 0.529 \text{ Å} \quad ; \quad 1\text{ht} = 27.21\text{eV} \tag{B.5}$$

Bibliography

[1] Doyen, G., Drakova, D., Barth, J. V., Schuster, R., Gritsch, T., Behm, R. J., and Ertl, G. *Phys. Rev. B* **48**, 1738 (1993).

[2] Drakova, D. and Doyen, G. *Phys. Rev. B* **56**(24), 577 (1997).

[3] Shor, P. W. In *35th Annual Symposium on Foundations of Computer Science.* IEEE Press, (1994).

[4] Petta, J. R., Johnson, A. C., Taylor, J. M., Laird, E. A., Yacoby, A., Lukin, M. D., Marcus, C. M., Hanson, M. P., and Gossard, A. C. *Science* **309**, 2180 (2005).

[5] Wineland, D. J., Monroe, C., Meekhof, D. M., King, B. E., Leibfried, D., Itano, W. M., Bergquist, J. C., Berkeland, D., Bollinger, J. J., and Miller, J. *Proc. R. Soc. Lond. A* **454**, 411 (1998).

[6] Jones, J. A. *Phil. Trans. R. Soc. Lond. A* **361**, 1429 (2003).

[7] Vandersypen, L. M. K., Steffen, M., Breyta, G., Yannoni, C. S., Sherwood, M. H., and Chang, I. L. *Nature* **414**, 883 (2001).

[8] DiVincenzo, D. P. In *Mesoscopic Electron Transport,* Kowenhoven, L., Schoen, G., and Sohn, L., editors, NATO ASI Series E. Kluwer Ac. Publ. (1997). Previously published on condmat/9612126.

[9] Nielsen, M. A. and Chuang, I. L. *Quantum Computation and Quantum Information.* Cambridge University Press, (2000).

[10] Jelezko, F. and Wratchtrup, J. *J. Phys.:Condens. Matter* **16**, 1089 (2004).

[11] Budakian, R., Mamin, H. J., Chui, B. W., and Rugar, D. *Science* **307**, 408 (2005).

[12] Rugar, D., Budakian, R., Mamin, H. J., and Chui, B. W. *Nature* **430**, 329 (2004).

[13] Nakamura, Y., Pashkin, Y. A., and Tsai, J. S. *Nature* **398**, 786 (1999).

[14] Gurvitz, S. A. *IEEE Transactions on Nanotechnology* **4**(1), 1 (2005).

[15] Lee, S., von Allmen, P., Oyafuso, F., Klimeck, G., and Whaley, K. B. *J. Appl. Phys.* **97**, 043706 (2005).

[16] Xiao, M., Martin, I., Yablonovitch, E., and Jiong, H. W. *Nature* **430**, 435 (2004).

[17] Blatt, R., Häffner, H., Roos, C. F., Becher, C., and Schmidt-Kaler, F. *Quantum Information Processing* **3**, 1 (2004).

[18] Reichel, J., Hänsel, W., and Hänsch, T. W. *Phys. Rev. Lett.* **83**(17), 3398 (1999).

[19] Heinrich, A. J., Lutz, C. P., Gupta, J. A., and Eigler, D. M. *Science* **298**, 1381 (2002).

[20] Ke, S., Baranger, H. U., and Yang, W. *J. Chem. Phys* **122**, 074704 (2005).

[21] Speyer, G., Akis, R., and Ferry, D. K. *Physica E* **19**, 145 (2003).

[22] Walczak, K. *condmat* , 0405090 (2004).

[23] Wan, C. C., Mozos, J., Taraschi, G., Wang, J., and Guo, H. *Appl. Phys. Lett.* **71**(3), 419 July (1997).

[24] Riquelme, J. J., la Vega, L., Yeyati, A., Agrait, N., Martin-Rodero, A., and Rubio-Bollinger, G. *Europhys. Lett* **70**(5), 663–669 (2005).

[25] Ferreti, A., Calzolari, A., Felice, R. D., Manghi, F., Caldas, M., Nardelli, M. B., and Molinari, E. *Phys. Rev. Lett.* **94**, 116802 (2005).

[26] Nieminen, J. A., Niemi, E., and Rieder, K.-H. *Surface Science* **552**, 47 (2004).

[27] Zarand, G., Borda, L., von Delft, J., and Andrei, N. *Phys. Rev. Lett.* **93**(10), 107204 (2004).

[28] Granot, E. *Phys. Rev. B* **71**, 035407 (2005).

[29] Durkan, C. and Welland, M. E. *Appl. Phys. Lett.* **80**(3), 458 (2002).

[30] Manassen, Y., Hamers, R. J., Demuth, J. E., and Castellano Jr, A. J. *Phys. Rev. Lett.* **62**(21), 2531 May (1989).

[31] Craik, D. *Magnetism: Principles and Applications.* John Wiley & Sons, (1995).

[32] Slichter, C. P. *Principles of Magnetic Resonance.* Springer-Verlag, 3rd edition, (1990).

[33] Binnig, G., Rohrer, H., Gerber, C., and Weibel, E. *Appl. Phys. Lett.* **40**(2), 178 (1982).

[34] Chen, C. J. *Introduction to Scanning Tunneling Microscopy.* Oxford University Press, (1993).

[35] Reiss, G., Schneider, F., Vancea, J., and Hoffmann, H. *Appl. Phys. Lett.* **57**(9), 867 (1990).

[36] Keller, D. *Surface Science* **253**, 353 (1991).

[37] Heinze, S., Bode, M., Kubetzka, A., Pietzsch, O., Nie, X., Blügel, S., and Wiesendanger, R. *Science* **288**, 180 (2000).

[38] Pietzsch, O., Kubetzka, A., Bode, M., and Wiesendanger, R. *Science* **292**, 205 (2001).

[39] Alvarado, S. F. *Phys. Rev. Lett.* **75**(3), 513 (1995).

[40] Drakova, D. *Rep. Prog. Phys.* **64**, 205 (2001).

[41] Bardeen, J. *Phys. Rev. Lett.* **6**(2), 57 Jan (1961).

[42] Tersoff, J. and Hamann, D. R. *Phys. Rev. B* **31**(2), 805 (1985).

[43] Clarke, A. R. H., Pethica, J. B., Nieminen, J. A., Besenbacher, F., Laegsgaard, E., and Stensgaard, I. *PRL* **76**(8), 1276 (1996).

[44] Doyen, G. *J. Phys.:Condens. Matter* **5**, 3305 (1993).

[45] Lucas, A. A., Morawitz, H., Henry, G. R., Vigneron, J. P., Lambim, P., Cutler, P. H., and Feuchtwang, T. E. *Phys. Rev. B* **37**(18), 10 708 (1988).

[46] Pendry, J. B., Pretre, A. B., and Krutzen, B. C. H. *J. Phys.:Condens. Matter* **3**, 4314 (1991).

[47] Zhu, J.-X. and Balatsky, A. V. *Phys. Rev. Lett.* **89**, 286802 (2002).

[48] Wortmann, D., Ishida, H., and Blügel, S. *Phys. Rev. B* **72**, 235113 (2005).

[49] Fan, W. *condmat* , 0407747 (2004).

[50] Manassen, Y. *J. Magnetic Resonance* **126**, 133 (1997).

[51] Goldsborough, J. P., Mandel, M., and Pake, G. E. *Phys. Rev. Lett.* **4**(1), 13 (1960).

[52] Dalal, N. S., Kennedy, D. E., and McDowell, C. A. *J. Chem. Phys.* **61**(5), 1689 (1974).

[53] Hamilton, W. O. and Pake, G. E. *J. Chem. Phys.* **39**(10), 2694 (1963).

[54] Durkan, C. *Contemporary Physics* **45**(1), 1 (2004).

[55] *2nd IRC in Nanotechnology Science Meeting*, (2003).

[56] Manassen, Y. and Balatsky, A. V. *Israel Journal of Chemistry* **44**(4), 401 (2004).

[57] Balatsky, A. V., Manassen, Y., and Salem, R. *cond-mat* , 0206325 (2002).

[58] Balatsky, A. V. and Martin, I. *cond-mat* , 0112407 (2002).

[59] Galperin, Y. M., Kozub, V. I., and Vinokur, V. M. *cond-mat* , 0402575 Feb (2004).

[60] Wittneven, C., Dombrowski, R., Pan, S. H., and Wiesendanger, R. *Rev. Sci. Instrum.* **68**(10), 3806 (1997).

[61] Dombrowski, R., Wittneven, C., Morgenstern, M., and Wiesendanger, R. *Appl. Phys. A* **66** (1998). S203.

[62] Sagisaka, K., Kitahara, M., Fujita, D., Kido, G., and Koguchi, N. *Nanotechnology* **15** (2004). S371.

[63] Petersen, L., Hofmann, P., Plummer, E. W., and Besenbacher, F. *J. Electron. Spectrosc. Relat. Phenom.* **109**, 97 (2000).

[64] Greiner, W. *Relativistic Quantum Mechanics*, chapter 2. Springer-Verlag (1990).

[65] Li, Z.-J., Liang, J.-Q., and Kobe, D. H. *Phys. Rev. A* **65**, 024101 (2002).

[66] Chen, C. J. *Introduction to Scanning Tunneling Microscopy*, chapter 7. Oxford University Press (1993).

[67] Strange, P. *Relativistic Quantum Mechanics.* Cambridge University Press, (1998).

[68] Gottfried, K. *Quantum Mechanics Volume 1: Fundamentals.* W.A. Benjamin Inc, (1966).

[69] Rose, M. E. *Relativistic Electron Theory.* John Wiley & Sons, (1961).

[70] Rodberg, L. S. and Thaler, R. M. *Introduction to The Quantum Theory of Scattering.* Academic Press, (1967).

[71] Wigner, E. P. *Physical Review* **98**(1), 145 (1955).

[72] Antoine, J.-P., Gesztesy, F., and Shabani, J. *J. Phys. A: Math. Gen.* **20**, 3687 (1987).

[73] Blinder, S. M. *Phys. Rev. A* **18**, 853 (1978).

[74] Dittrich, J., Exner, P., and Šeba, P. *J. Maths. Phys.* **33**(6), 2207 (1992).

[75] Villarroel, D. *Eur. J. Phys.* **19**, 85 (1998).

[76] Dörr, J. *ZAMP* **4**, 122 (1952).

[77] Taylor, J. R. *Scattering Theory*, chapter 3. John Wiley and Sons, Inc (1972).

[78] Kennedy, P., Dombey, N., and Hall, R. L. *Int. J. Mod. Phys. A* **19**, 3557 (2004).

[79] Weinberger, P. *Electron Scattering Theory for Ordered and Disordered Matter.* Oxford Science Publications, (1990).

[80] Dimonguez-Adame, F. *J. Phys. A: Math. Gen* **23**, 1993 (1990).

[81] Salazar, A. and de Llano, M. *cond-mat* , 0305631 May (2003).

[82] Dittrich, J., Exner, P., and Šeba, P. *J. Maths. Phys.* **30**(12), 2875 (1989).

[83] McKellar, B. H. J. and Stephenson Jr, G. J. *Phys. Rev. A* **36**(6), 2566 (1987).

[84] Benguria, R. D., Castillo, H., and Loewe, M. *J. Phys. A: Math. Gen.* **33**, 5315 (2000).

[85] Dong, S.-H. and Ma, Z.-Q. *Foundations of Physics Letters* **15**, 191 (2002).

[86] Loewe, M. and Mendizabal, S. *quant-ph* , 0402030 Feb (2004).

[87] Dominguez-Adame, F. and Marciá, E. *J. Phys. A: Math. Gen* **22**, 419 (1989).

[88] Merzbacher, E. *Quantum Mechanics.* John Wiley & Sons, 2nd edition, (1970).

[89] Krane, K. S. *Introductory Nuclear Physics.* John Wiley & Sons, (1988).

[90] Newton, R. G. *Scattering Theory of Waves and Particles.* Courier Dover Publications, 2nd edition, (2002).